Department
of
APPLIED MATHEMATICS

Using a σ-coordinate numerical ocean model for simulating the circulation at Ormen Lange

By

Inge K. Eliassen and Jarle Berntsen

Report no. 138 January 2000

UNIVERSITY OF BERGEN
Bergen, Norway

Department of Mathematics
University of Bergen
5008 Bergen
Norway

ISSN 0084-778x

Using a σ-coordinate numerical ocean model for simulating the circulation at Ormen Lange.

by

Inge K. Eliassen and Jarle Berntsen

Report No. 138

January 2000

Contents

List of Figures

1 Introduction

A three dimensional numerical ocean model has been implemented for simulating the circulation at Ormen Lange. The model, using a topography following vertical coordinate and a time split integration procedure, was developed at the Institute of Marine Research and the University of Bergen starting in 1995. A recent user's guide [4] describes details regarding algorithms and implementations.

The model has been used in some studies, see [7, 5, 3, 6, 14, 15, 13, 2]. In the development of the code especially the ability of the model to maintain the properties of different water masses has been in focus and in [6] the model capabilities in this respect are documented using observations from the SKAGEX experiment in 1990 [12]. Model results from the present code are also compared to model results from the Blumberg and Mellor model [9].

In this study the model is implemented for a 28 km $\times$ 46 km area at Ormen Lange. The equations of the model are described in Sections 2 and 3, while Section 4 gives details of the model setup, e.g., initial fields and forcing. The following section then presents results from simulations of different scenarios with varying direction and magnitude of the background velocity field.

2 The σ-coordinate model

2.1 The Basic Variables and Equations

The symbols used in the description of the model are given in Appendix B. The model assumes that the weight of the fluid identically balances the pressure (hydrostatic assumption), and that density differences are neglected unless the differences are multiplied by gravity (Boussinesq approximation). The following equations are used to describe the variables as functions of the Cartesian coordinates x, y, z.

The continuity equation is

$$\nabla \cdot \vec{U} + \frac{\partial W}{\partial z} = 0, \tag{1}$$

and the Reynolds momentum equations are

$$\frac{\partial U}{\partial t} + \vec{U} \cdot \nabla U + W\frac{\partial U}{\partial z} - fV = -\frac{1}{\rho_0}\frac{\partial P}{\partial x} + \frac{\partial}{\partial z}(K_M \frac{\partial U}{\partial z}) + F_x, \tag{2}$$

$$\frac{\partial V}{\partial t} + \vec{U} \cdot \nabla V + W\frac{\partial V}{\partial z} + fU = -\frac{1}{\rho_0}\frac{\partial P}{\partial y} + \frac{\partial}{\partial z}(K_M \frac{\partial V}{\partial z}) + F_y, \tag{3}$$

$$\rho g = -\frac{\partial P}{\partial z}. \tag{4}$$

The pressure at depth z may be obtained by integrating equation (4) vertically

$$P = P_{atm} + g\rho_0\eta + g\int_z^0 \rho(\acute{z})d\acute{z}. \tag{5}$$

The conservation equations for temperature and salinity are

$$\frac{\partial T}{\partial t} + \vec{U} \cdot \nabla T + W\frac{\partial T}{\partial z} = \frac{\partial}{\partial z}(K_H \frac{\partial T}{\partial z}) + F_T, \tag{6}$$

$$\frac{\partial S}{\partial t} + \vec{U} \cdot \nabla S + W\frac{\partial S}{\partial z} = \frac{\partial}{\partial z}(K_H \frac{\partial S}{\partial z}) + F_S. \tag{7}$$

The density is computed according to an equation of state of the form

$$\rho = \rho(T, S) \tag{8}$$

taken from [26].

Motions induced by small scale processes (sub-grid scale) are parameterized by horizontal and vertical eddy viscosity/diffusivity terms. The horizontal terms F_x, F_y, F_T and F_S may be written

$$F_{x,y} = \frac{\partial}{\partial x}(A_M \frac{\partial(U,V)}{\partial x}) + \frac{\partial}{\partial y}(A_M \frac{\partial(U,V)}{\partial y}), \tag{9}$$

$$F_{T,S} = \frac{\partial}{\partial x}(A_H \frac{\partial(T,S)}{\partial x}) + \frac{\partial}{\partial y}(A_H \frac{\partial(T,S)}{\partial y}). \tag{10}$$

The horizontal diffusivities, A_M and A_H, may be computed according to Smagorinsky [25]

$$(A_M, A_H) = (C_M, C_H)\Delta x\, \Delta y\, \frac{1}{2}[(\frac{\partial U}{\partial x})^2 + \frac{1}{2}\,(\frac{\partial V}{\partial x} + \frac{\partial U}{\partial y})^2 + (\frac{\partial V}{\partial y})^2]^{\frac{1}{2}} \tag{11}$$

or chosen to be constant.

2.1.1 Equations for K_M and K_H

The system of equations given in the previous section is not closed without equations for the vertical viscosity, K_M, and the vertical diffusivity, K_H. There is a long range of turbulence closure schemes that have and are being used in ocean models, see for instance Davies and Xing (1995) [11] and Davies et al. (1995) [10]. There are a number of factors that may govern the choice of turbulence closure in the vertical: the stratification, tidal forcing, the vertical resolution etc.

The present numerical ocean model may be linked to any of the options found in the above literature or elsewhere.

In cases where a limited number of physical phenomena are occurring simpler models may play a role, but our experience is that when we have model areas where both stratification and tidal forcing are important, we need at least the complexity of the Mellor and Yamada [22] 2 1/2 level model. The governing equations with the modifications due to Galperin et al. (1988) [17] for turbulent kinetic energy, $q^2/2$, and turbulent macro scale, l, are given below,

$$\begin{aligned}\frac{\partial q^2}{\partial t} + \vec{U}\cdot\nabla q^2 + W\frac{\partial q^2}{\partial z} &= \frac{\partial}{\partial z}(K_q\frac{\partial q^2}{\partial z}) + \\ 2K_M\left[\left(\frac{\partial U}{\partial z}\right)^2 + \left(\frac{\partial V}{\partial z}\right)^2\right] &+ \frac{2g}{\rho_0}K_H\frac{\partial \rho}{\partial z} - \frac{2q^3}{B_1 l}\end{aligned} \tag{12}$$

$$\begin{aligned}\frac{\partial q^2 l}{\partial t} + \vec{U}\cdot\nabla q^2 l + W\frac{\partial q^2 l}{\partial z} &= \frac{\partial}{\partial z}(K_q\frac{\partial q^2 l}{\partial z}) + \\ lE_1K_M\left[\left(\frac{\partial U}{\partial z}\right)^2 + \left(\frac{\partial V}{\partial z}\right)^2\right] &+ \frac{lE_1 g}{\rho_0}K_H\frac{\partial \rho}{\partial z} - \frac{q^3}{B_1}\tilde{W}\end{aligned} \tag{13}$$

where

$$\tilde{W} = 1 + E_2\left(\frac{l}{\kappa L}\right)^2 \tag{14}$$

and where

$$L^{-1} = (\eta - z)^{-1} + (H + z)^{-1}. \tag{15}$$

$\kappa = 0.4$ is the von Karman constant. Defining

$$G_H = \frac{l^2}{q^2}\frac{g}{\rho_0}\frac{\partial \rho}{\partial z} \tag{16}$$

the stability functions become

$$S_H[1 - (3A_2B_2 + 18A_1A_2)G_H] = A_2[1 - 6A_1/B_1] \tag{17}$$

and

$$S_M[1 - 9A_1A_2G_H] - S_H[18A_1^2 + 9A_1A_2)G_H] = A_1[1 - 3C_1 - 6A_1/B_1] \tag{18}$$

K_M and K_q are then computed according to

$$K_M = lqS_M \tag{19}$$
$$K_H = lqS_H \tag{20}$$
$$K_q = 0.20lq \tag{21}$$

The empirical values in the expressions above are

$$(A_1, A_2, B_1, B_2, C_1, E_1, E_2) = (0.92, 0.74, 16.6, 10.1, 0.08, 1.8, 1.33) \tag{22}$$

2.1.2 Boundary conditions

At the free surface, $z = \eta(x, y)$, we have

$$\rho_0 K_M \left(\frac{\partial U}{\partial z}, \frac{\partial V}{\partial z}\right) = (\tau_{0x}, \tau_{0y}), \tag{23}$$
$$\rho_0 K_H \left(\frac{\partial T}{\partial z}, \frac{\partial S}{\partial z}\right) = (\dot{T}_0, \dot{S}_0), \tag{24}$$
$$q^2 = B_1^{2/3} u_{\tau s}, \tag{25}$$
$$l = 0, \tag{26}$$

where $u_{\tau s} = (\vec{\tau}_0^2)^{1/2}$.

There are no volume fluxes through the side walls. On the side walls and bottom of the basin there are no advective or diffusive heat and salt fluxes. The vertical velocities at the free surface and at the bottom are given by

$$W_0 = U\frac{\partial \eta}{\partial x} + V\frac{\partial \eta}{\partial y} + \frac{\partial \eta}{\partial t}, \tag{27}$$

$$W_b = -U_b\frac{\partial H}{\partial x} - V_b\frac{\partial H}{\partial y}. \tag{28}$$

The effect of the bottom drag on horizontal velocities is given by

$$\rho_0 K_M\left(\frac{\partial U}{\partial z}, \frac{\partial V}{\partial z}\right) = (\tau_{bx}, \tau_{by}). \tag{29}$$

The bottom stress is specified by

$$\vec{\tau_b} = \rho_0 C_D |\vec{U}_b| \vec{U}_b \tag{30}$$

where the drag coefficient C_D is given by

$$C_D = \max[0.0025, \frac{\kappa^2}{(ln(z_b/z_0))^2}] \tag{31}$$

and z_b is the distance of the nearest grid point to the bottom. The von Karman constant $\kappa = 0.4$. In lack of further information we use $z_0 = 0.01m$ for the bottom roughness parameter, see Weatherly and Martin [27]. For q^2 and l the following conditions are applied at the bottom

$$q^2 = B_1^{2/3} u_{\tau b}, \tag{32}$$

$$l = 0, \tag{33}$$

where $u_{\tau b} = (\vec{\tau}_b^2)^{1/2}$.

2.2 The σ-coordinate system

The basic equations have been transformed into a bottom following sigma coordinate system [23]. The independent variables (x, y, z, t) are transformed to (x^*, y^*, σ, t^*), where

$$x^* = x \quad y^* = y \quad \sigma = \frac{z-\eta}{H+\eta} \quad t^* = t. \tag{34}$$

σ ranges from $\sigma = 0$ at $z = \eta$ to $\sigma = -1$ at $z = -H(x, y)$. Introducing the total depth, $D \equiv H + \eta$, the basic equations may now be written as (after deletion of the asterisks)

$$\frac{\partial UD}{\partial x} + \frac{\partial VD}{\partial y} + \frac{\partial \omega}{\partial \sigma} + \frac{\partial \eta}{\partial t} = 0 \tag{35}$$

where the relationship between W and the new vertical velocity ω is given by

$$W = \omega + U\left(\sigma\frac{\partial D}{\partial x} + \frac{\partial \eta}{\partial x}\right) + V\left(\sigma\frac{\partial D}{\partial y} + \frac{\partial \eta}{\partial y}\right) + (1+\sigma)\frac{\partial \eta}{\partial t} \quad . \tag{36}$$

The momentum equations on flux form become

$$\frac{\partial UD}{\partial t} + \frac{\partial U^2 D}{\partial x} + \frac{\partial UVD}{\partial y} + \frac{\partial U\omega}{\partial \sigma} - fVD + \frac{D}{\rho_0}\frac{\partial P_{atm}}{\partial x} + gD\frac{\partial \eta}{\partial x} =$$

$$\frac{\partial}{\partial \sigma}(\frac{K_M}{D}\frac{\partial U}{\partial \sigma}) - \frac{gD^2}{\rho_0}\int_\sigma^0 \left(\frac{\partial \rho}{\partial x} - \frac{\sigma}{D}\frac{\partial D}{\partial x}\frac{\partial \rho}{\partial \sigma}\right) d\sigma + DF_x, \tag{37}$$

$$\frac{\partial VD}{\partial t}+\frac{\partial UVD}{\partial x}+\frac{\partial V^2D}{\partial y}+\frac{\partial V\omega}{\partial \sigma}+fUD+\frac{D}{\rho_0}\frac{\partial P_{atm}}{\partial y}+gD\frac{\partial \eta}{\partial y}=$$
$$\frac{\partial}{\partial \sigma}(\frac{K_M}{D}\frac{\partial V}{\partial \sigma})-\frac{gD^2}{\rho_0}\int_\sigma^0\left(\frac{\partial \rho}{\partial y}-\frac{\sigma}{D}\frac{\partial D}{\partial y}\frac{\partial \rho}{\partial \sigma}\right)d\sigma+DF_y. \tag{38}$$

The new conservation equations take the form

$$\frac{\partial TD}{\partial t}+\frac{\partial TUD}{\partial x}+\frac{\partial TVD}{\partial y}+\frac{\partial T\omega}{\partial \sigma}=\frac{\partial}{\partial \sigma}(\frac{K_H}{D}\frac{\partial T}{\partial \sigma})+DF_T, \tag{39}$$

$$\frac{\partial SD}{\partial t}+\frac{\partial SUD}{\partial x}+\frac{\partial SVD}{\partial y}+\frac{\partial S\omega}{\partial \sigma}=\frac{\partial}{\partial \sigma}(\frac{K_H}{D}\frac{\partial S}{\partial \sigma})+DF_S, \tag{40}$$

and the horizontal viscosity and diffusion terms are now defined according to

$$DF_{x,y}=\frac{\partial}{\partial x}(A_M\frac{\partial(UD,VD)}{\partial x})+\frac{\partial}{\partial y}(A_M\frac{\partial(UD,VD)}{\partial y}), \tag{41}$$

$$DF_{T,S}=\frac{\partial}{\partial x}(DA_H\frac{\partial(T,S)}{\partial x})+\frac{\partial}{\partial y}(DA_H\frac{\partial(T,S)}{\partial y}). \tag{42}$$

It should be noted that several terms originating from the σ- coordinate transformation are neglected in equations (41) and (42). These simplified formulations for horizontal viscosity/diffusivity terms in σ-coordinate models are suggested by Mellor and Blumberg [21]. In [21] a description of the complete terms is also given. It should be noted that with the present model we try to run with A_H equal to zero to avoid isopycnal diffusion. Using a monotonic and stable scheme for advecting the scalar fields S and T this has proved to be feasible without introducing instabilities.

2.2.1 Vertical boundary conditions

The new boundary conditions for the vertical velocity, ω, in equation (35) become

$$\omega(0)=\omega(-1)=0. \tag{43}$$

The new conditions at the surface ($\sigma=0$) becomes

$$\frac{K_M}{D}\left(\frac{\partial U}{\partial \sigma},\frac{\partial V}{\partial \sigma}\right)=\frac{1}{\rho_0}(\tau_{0x},\tau_{0y}), \tag{44}$$

$$\frac{K_H}{D}\left(\frac{\partial T}{\partial \sigma},\frac{\partial S}{\partial \sigma}\right)=(\dot{T}_0,\dot{S}_0), \tag{45}$$

and at the bottom ($\sigma=-1$) the boundary conditions become

$$\frac{K_M}{D}\left(\frac{\partial U}{\partial \sigma},\frac{\partial V}{\partial \sigma}\right)=\frac{1}{\rho_0}(\tau_{bx},\tau_{by}), \tag{46}$$

$$\frac{K_H}{D}\left(\frac{\partial T}{\partial \sigma},\frac{\partial S}{\partial \sigma}\right)=0. \tag{47}$$

3 Mode splitting

To be able to represent gravity waves and the effects of these correctly, the time step must be chosen such that the Courant number become less than unity. To avoid this restriction when propagating the 3-D fields, mode splitting very similar to the splitting applied by Slagstad [24] and later described in [1] is applied.

The 3-D velocity field is split into its baroclinic part and its depth integrated part according to:

$$(U(x,y,\sigma),V(x,y,\sigma)) \;=\; (U_A(x,y)+U_B(x,y,\sigma),V_A(x,y)+V_B(x,y,\sigma)) \tag{48}$$

where

$$(U_A(x,y),V_A(x,y)) \;=(\int_{-1}^{0}U(x,y,\sigma)d\sigma,\int_{-1}^{0}V(x,y,\sigma)d\sigma).$$

Depth integrating the moment equations and the continuity equation gives, neglecting for a moment the atmospheric pressure terms and the vertical viscosity terms, gives:

$$\frac{\partial U_A D}{\partial x}+\frac{\partial V_A D}{\partial y}+\frac{\partial \eta}{\partial t}=0, \tag{49}$$

$$\begin{aligned}&\frac{\partial U_A D}{\partial t}-fV_A D+gD\frac{\partial \eta}{\partial x}=\\ &\quad\frac{\partial}{\partial x}(A_{M2D}\frac{\partial U_A D}{\partial x})+\frac{\partial}{\partial y}(A_{M2D}\frac{\partial U_A D}{\partial y})+A_x\end{aligned} \tag{50}$$

and

$$\begin{aligned}&\frac{\partial V_A D}{\partial t}+fU_A D+gD\frac{\partial \eta}{\partial y}=\\ &\quad\frac{\partial}{\partial y}(A_{M2D}\frac{\partial V_A D}{\partial y})+\frac{\partial}{\partial x}(A_{M2D}\frac{\partial V_A D}{\partial x})+A_y,\end{aligned} \tag{51}$$

where

$$(A_x,A_y)=(\int_{-1}^{0}\Delta U d\sigma,\int_{-1}^{0}\Delta V d\sigma), \tag{52}$$

$$\Delta U=-\frac{gD^2}{\rho_0}\int_{\sigma}^{0}\left(\frac{\partial \rho}{\partial x}-\frac{\sigma}{D}\frac{\partial D}{\partial x}\frac{\partial \rho}{\partial \sigma}\right)d\sigma-\frac{\partial U^2 D}{\partial x}+\frac{\partial UVD}{\partial y}+\frac{\partial U\omega}{\partial \sigma}, \tag{53}$$

$$\Delta V=-\frac{gD^2}{\rho_0}\int_{\sigma}^{0}\left(\frac{\partial \rho}{\partial y}-\frac{\sigma}{D}\frac{\partial D}{\partial y}\frac{\partial \rho}{\partial \sigma}\right)d\sigma-\frac{\partial UVD}{\partial x}+\frac{\partial V^2 D}{\partial y}+\frac{\partial V\omega}{\partial \sigma}. \tag{54}$$

The non-linear and the internal pressure terms are represented through A_x and A_y. The vertical integration is exact except for the horizontal viscosity terms. These terms take mainly care of small scale oscillations, and the 2-D A_{M2D} field is computed according to (11) where (U,V) is replaced by (U_A,V_A).

The equations for the baroclinic fields U_B and V_B become after subtracting (50) from (37) and (51) from (38) :

$$\frac{\partial U_B D}{\partial t} - fV_B D + \frac{1}{\rho_0}(\tau_{0x} - \tau_{bx}) + A_x = \frac{\partial}{\partial x}(A_M \frac{\partial U_B D}{\partial x}) + \frac{\partial}{\partial y}(A_M \frac{\partial U_B D}{\partial y}) + \frac{\partial}{\partial \sigma}(\frac{K_M}{D}\frac{\partial U_B}{\partial \sigma}) + \Delta U \tag{55}$$

and

$$\frac{\partial V_B D}{\partial t} + fU_B D + \frac{1}{\rho_0}(\tau_{0y} - \tau_{by}) + A_y = \frac{\partial}{\partial y}(A_M \frac{\partial V_B D}{\partial y}) + \frac{\partial}{\partial x}(A_M \frac{\partial V_B D}{\partial x}) + \frac{\partial}{\partial \sigma}(\frac{K_M}{D}\frac{\partial V_B}{\partial \sigma}) + \Delta V. \tag{56}$$

4 Model setup for Ormen Lange

4.1 Discretization

The geographic location of the model area is shown in Figure 1. The coordinates of the corners are

(5.088241°E, 63.755029°N)	(5.651078°E, 63.745778°N)
(5.058392°E, 63.344280°N)	(5.613203°E, 63.335193°N)

The bathymetry is given in Figure 2 and has a depth varying between 198.4 m and 1210.5 m with a mean value of 876.7 m.

The grid size is 70×115 cells horizontally with a resolution of 400 m. One experiment is done using a 140×230 grid with 200 m resolution. Vertically 30 σ-layers are distributed according to a formulae given in Lynch et al. (1995) [19]. At 1000 m depth their thicknesses in meters are (10, 11, 13, 16, 20, 24, 28, 33, 38, 43, 47, 51, 54, 56, 57, 57, 56, 54, 51, 47, 43, 38, 33, 28, 24, 20, 16, 13, 11, 10).

The time integration is split into a two-dimensional external mode and a three-dimensional internal mode. The time steps are determined by the CFL requirement related to external and internal wave speed respectively. In the external mode surface elevation and vertically integrated velocities are propagated with a short time step equaling 1.8 s. The internal mode updates all three-dimensional fields using a longer time step of 72 s. For the 140×230 grid these time steps are halved.

The model is run for 48 hours forward in time.

4.2 Initial values

Initial values for salinity temperature and horizontal velocity, see Figure 3, are based on the diagnostic climatology of Engedahl et al. (1998) [16]. The initial fields are depth varying, but set to be horizontally constant. The horizontal velocities are simplified as

$$|\vec{U}| = 1.05 + \frac{0.15}{\pi} \arctan\left(\frac{z+700}{50}\right) + 0.05\, e^{z/50}$$
$$U = |\vec{U}| \sin(\theta)$$
$$V = |\vec{U}| \cos(\theta)$$

where θ is the deviation from a northward direction. Figure 4 gives initial values of current speeds through Section I given in Figure 2.

The initial surface elevation, η, is derived from geostrophic balance

$$fV_A = g\frac{\partial \eta}{\partial x}$$
$$-fU_A = g\frac{\partial \eta}{\partial y}$$

and adjusted so that $\overline{\eta} = 0$. See Figure 5.

4.3 Forcing

The simulations are driven by forcing through relaxation towards climatology at the open boundaries and by the Coriolis force. No tidal or atmospheric forcing is applied.

At the open boundaries there are seven grid cell wide flow relaxation zones where the prognostic variables are relaxed towards a specified forced solution. See Martinsen & Engedahl (1987) [20]. The initial values are used as the specified forced solution.

Each prognostic variable, ϕ, in the zone is after each model time step updated according to

$$\phi = (1 - \alpha)\phi_M + \alpha\phi_F,$$

where ϕ_M contains the unrelaxed values computed by the model and ϕ_F is a specified forced solution in the zone. The relaxation parameter α varies from 1 at the model boundary to 0 at the end of the zone facing the interior model domain.

4.4 Experiments

Simulation of different scenarios are carried out by varying magnitude and direction of the initial velocity field. These experiments are numbered 1–4 as given by Table 1.

	Speed $\times$ 1	Speed $\times$ 2
$\theta = 30°$	1	2
$\theta = 60°$	3	4

Table 1: Experiments 1–4.

Experiment 5 uses estimated maximum speed over a 10 year period as initial values, see Figure 6. The direction of the flow is chosen as $\theta = 30°$.

Experiment 6 is carried out to test the effects of enhanced resolution. The grid size is doubled giving a horizontal resolution of 200 m. The same number of σ-layers, 30, is applied vertically. The time steps for both the external and internal modes are halved. Initial values are as in experiment 4, i.e., double speed and $\theta = 60°$.

The model is in all experiments run with constant and fairly large viscosities, see Table 2, to avoid $2\Delta x$ and $2\Delta t$ noise in the solutions. Notice from the table that when using the stronger forcing in experiment 5 the viscosity had to be increased. When the resolution was refined in experiment 6 the values could be reduced because more of the smaller scale phenomena could be resolved. Smaller values of viscosities than those given in Table 2 give more noisy results. Larger values may be used, but detail in the solutions will gradually be lost as the values are increased.

4.5 Output

The plots presented at the end of each experiment are

Experiment	AM	AM2D
1–4	$70\,\mathrm{m^2\,s^{-1}}$	$2777\,\mathrm{m^2\,s^{-1}}$
5	$112\,\mathrm{m^2\,s^{-1}}$	$4444\,\mathrm{m^2\,s^{-1}}$
6	$42\,\mathrm{m^2\,s^{-1}}$	$1667\,\mathrm{m^2\,s^{-1}}$

Table 2: Viscosities.

- Contour plots of speed and vector plots of velocity at 100 m depth, at 50 m over bottom, and at 10 m over bottom.
- Contour plots of speed along $J = 30$ and along $J = 80$.

In addition, for experiments 1 and 2 the average kinetic energy as a function of time is given.

(a) Contours at depths 200, 400, 800, **1000**, 1500, 2000, 2500, ...

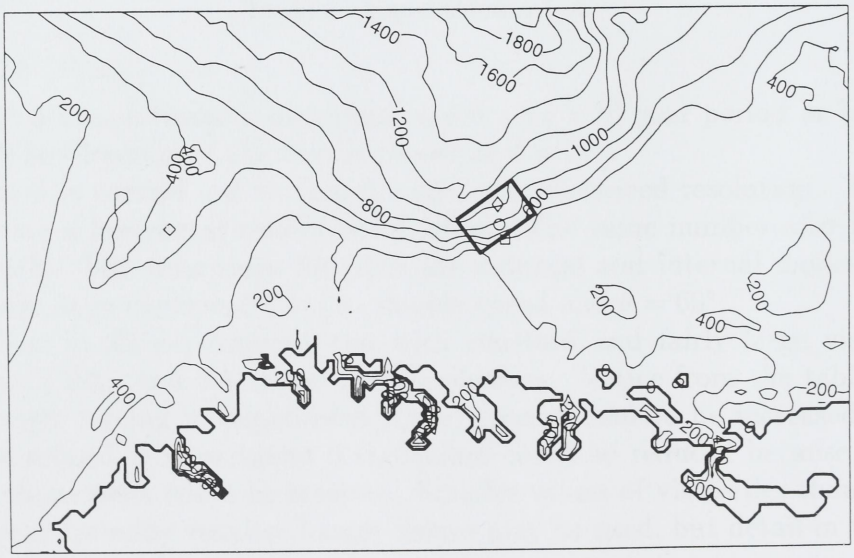

(b) Measurements positions at ◊, ○ and □.

Figure 1: Location of the model area.

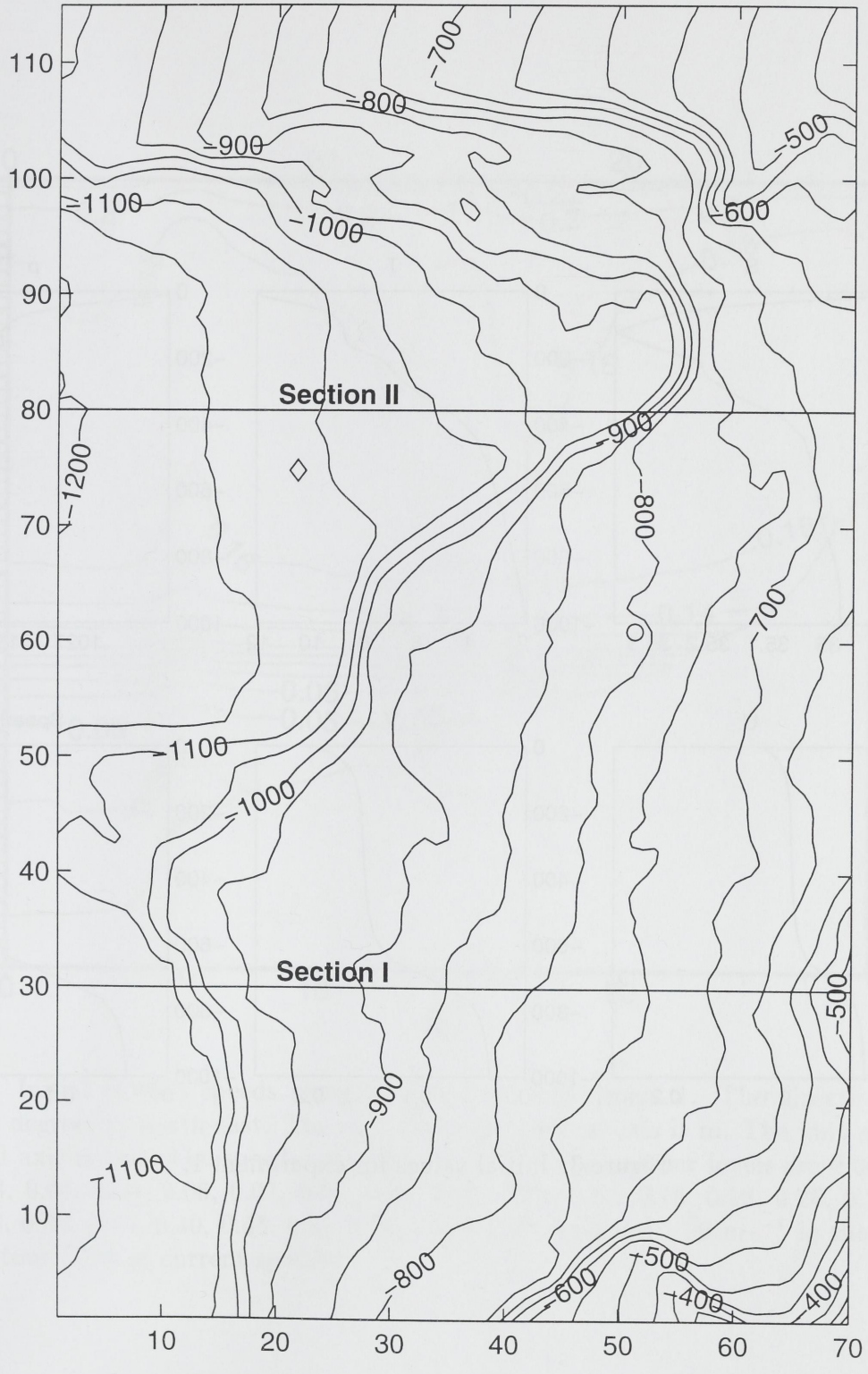

Figure 2: Model area bathymetry.

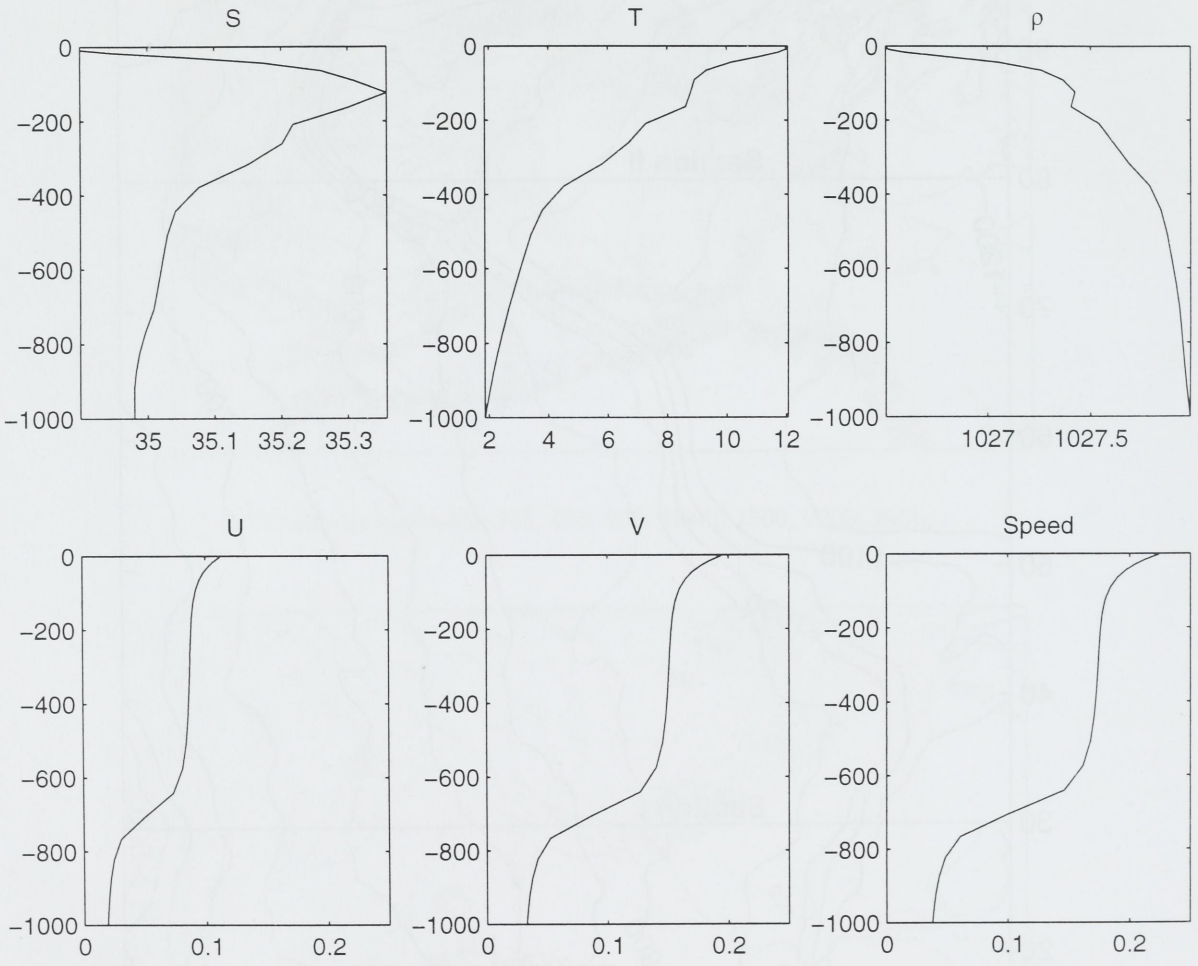

Figure 3: Initial values for experiment 1.

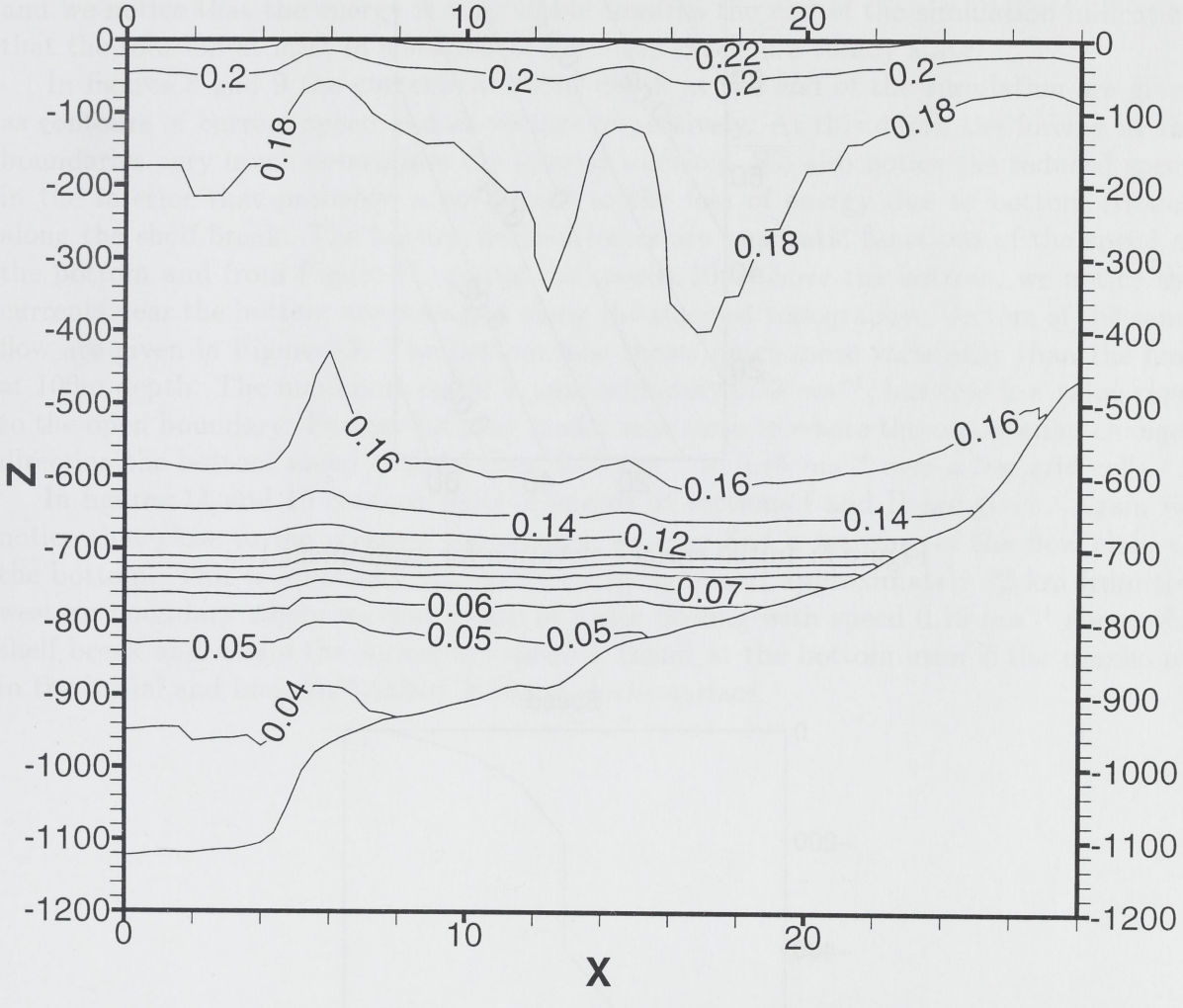

Figure 4: Initial current speeds along Section I for experiment 1. The direction of the flow is 30 degrees to north-east. The unit along the vertical axis is m. The unit along the horizontal axis is km. The speeds are given in $\mathrm{m\,s^{-1}}$. The contour levels are 0.005, 0.01, 0.02, 0.03, 0.04, 0.05, 0.06, 0.07, 0.08, 0.09, 0.10, 0.12, 0.14, 0.16, 0.18, 0.20, 0.22, 0.24, 0.26, 0.28, 0.30, 0.35, 0.40, 0.45, 0.50, 0.60, 0.70, 0.80, 0.90 and 1.00 $\mathrm{m\,s^{-1}}$ in this and all other contour plots of current speeds.

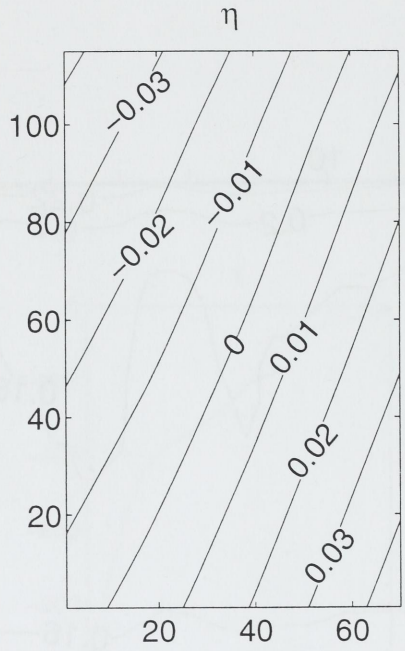

Figure 5: Initial surface elevation for experiment 1.

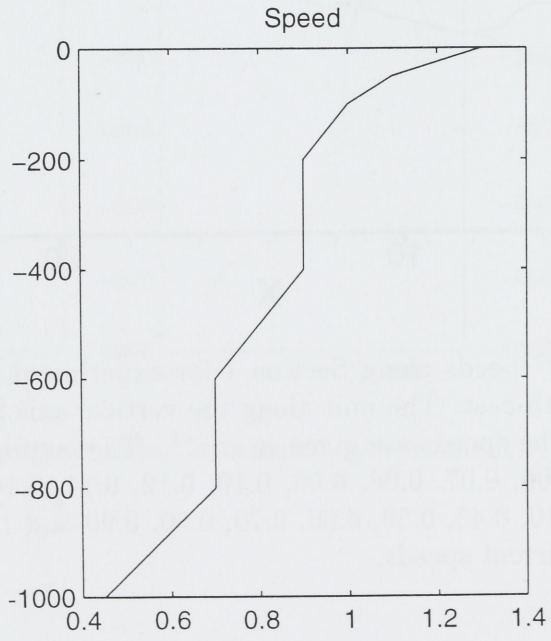

Figure 6: Estimated maximum speed over 10 years.

5 Numerical experiments

5.1 Numerical experiment 1

In Figure 7 the average kinetic energy over the model area is given as a function of time and we notice that the energy is very stable towards the end of the simulation indicating that the solution at least in a statistical sense has reached a steady state.

In figures 8 and 9 the currents at 100m depth at the end of the simulation are given as contours of current speed and as vectors respectively. At this depth the forcing at the boundaries very much determines the interior solution. We also notice the reduced speed in the interior that probably is connected to the loss of energy due to bottom friction along the shelf break. The bottom friction losses are quadratic functions of the speed at the bottom and from Figure 12, giving the speeds 10m above the bottom, we notice the currents near the bottom are strongest along the steepest topography. Vectors of the same flow are given in Figure 13. The bottom flow shows much more variability than the flow at 100m depth. The maximum speed is approximately 0.23 ms^{-1}, but this is a value close to the open boundary. Further into the model area close to where the topography changes direction the bottom speed changes from 0.05 ms^{-1} to 0.16 ms^{-1} over a few grid cells.

In figures 14 and 15 contour plots of speeds at sections I and II are given. Again we notice that close to the steepest topography we may find a focusing of the flow close to the bottom. This is especially noticeable along section II approximately 22 km from the western boundary where we find a core of water flowing with speed 0.16 ms^{-1} above the shelf break and where the maximum speed is found at the bottom even if the maximum in the initial and boundary values is found at the surface.

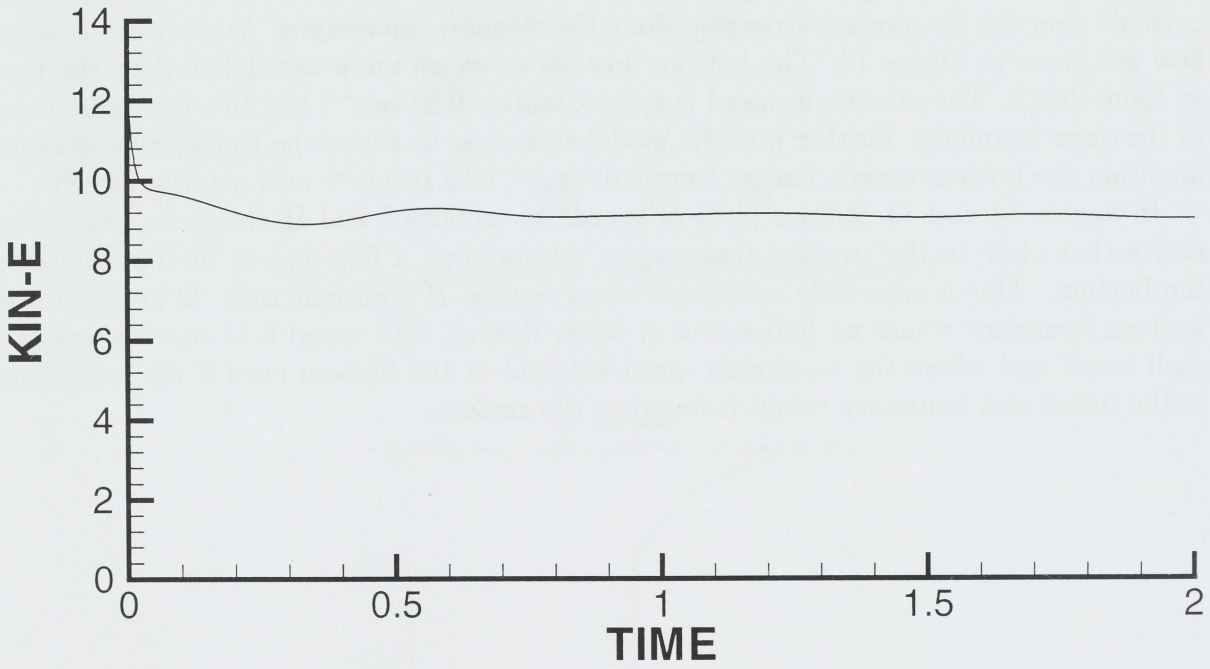

Figure 7: Volume averaged kinetic energy in Jm^{-3} as a function of time in days.

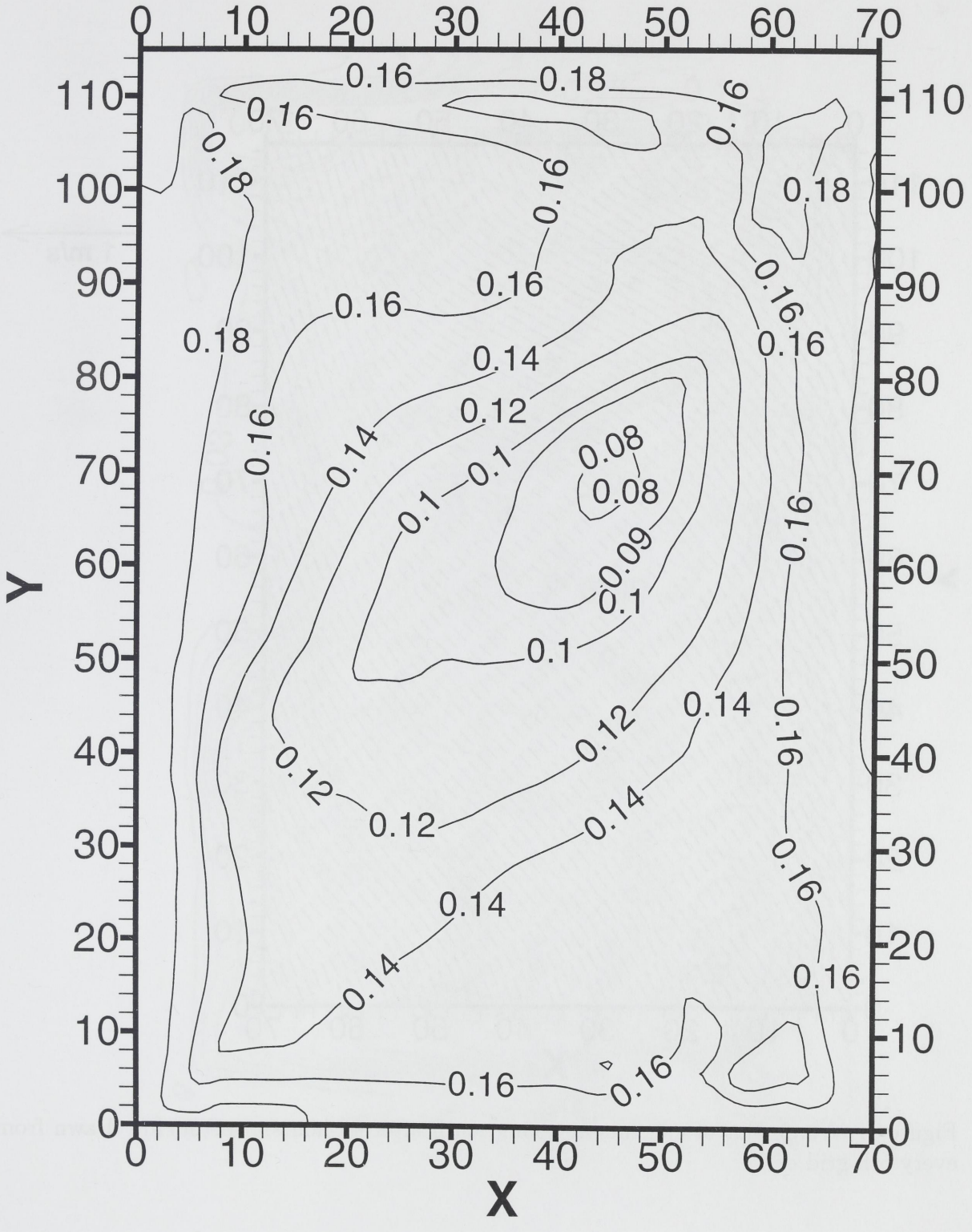

Figure 8: Current speeds at 100m depth after 48 hours.

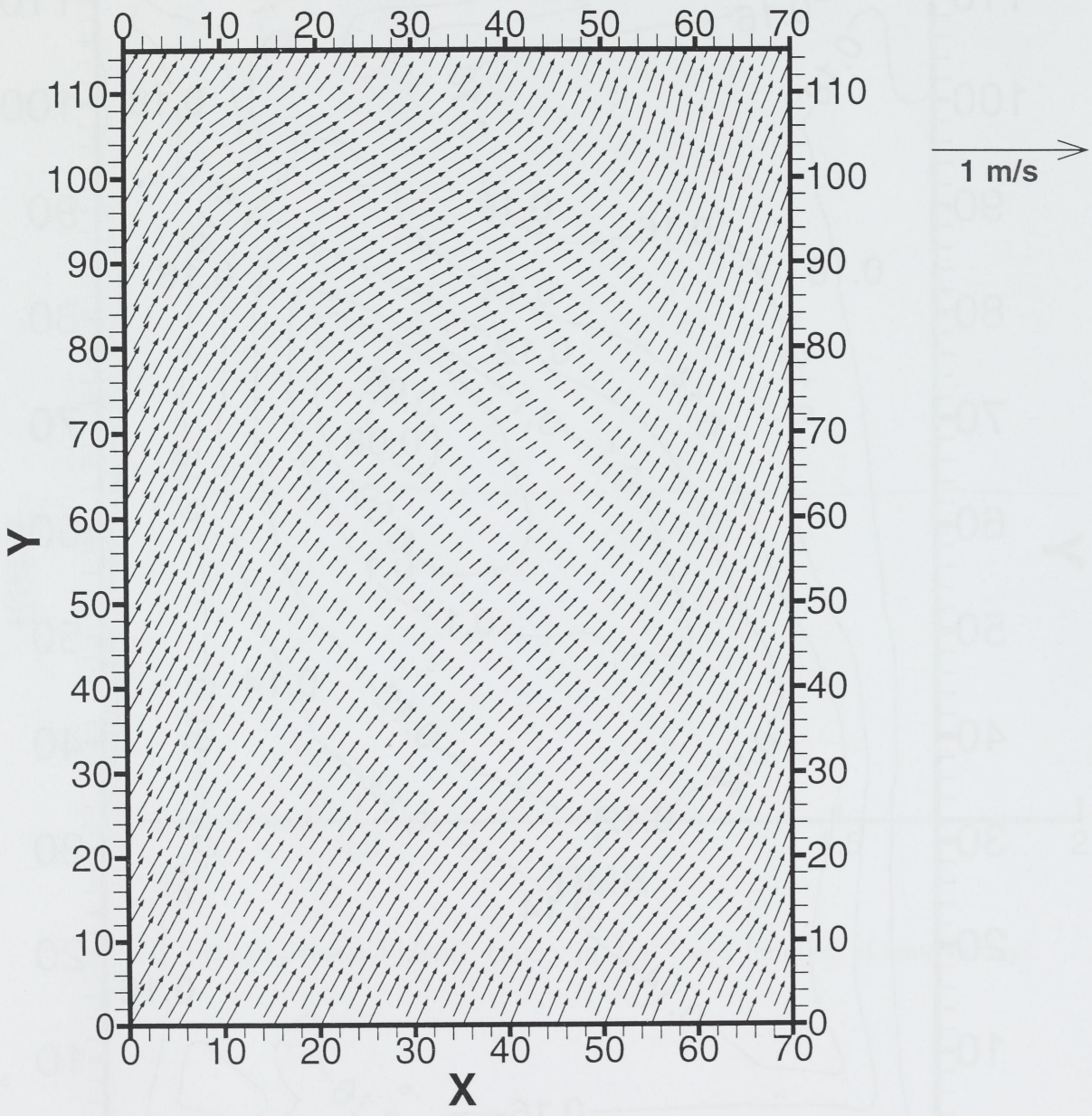

Figure 9: Vector plot of currents at 100m depth after 48 hours. Vectors are drawn from every 5th grid cell.

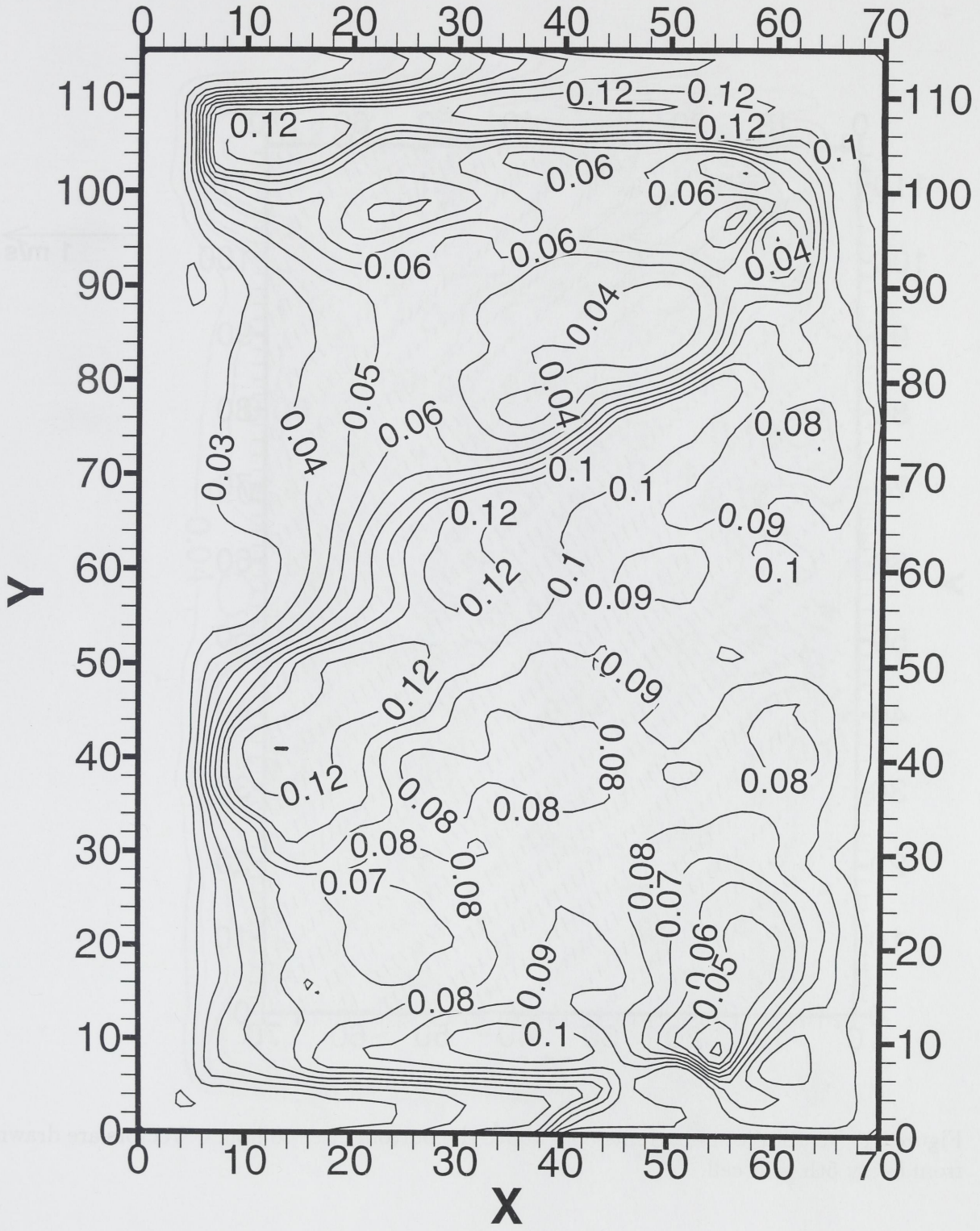

Figure 10: Current speeds 50m above the bottom after 48 hours.

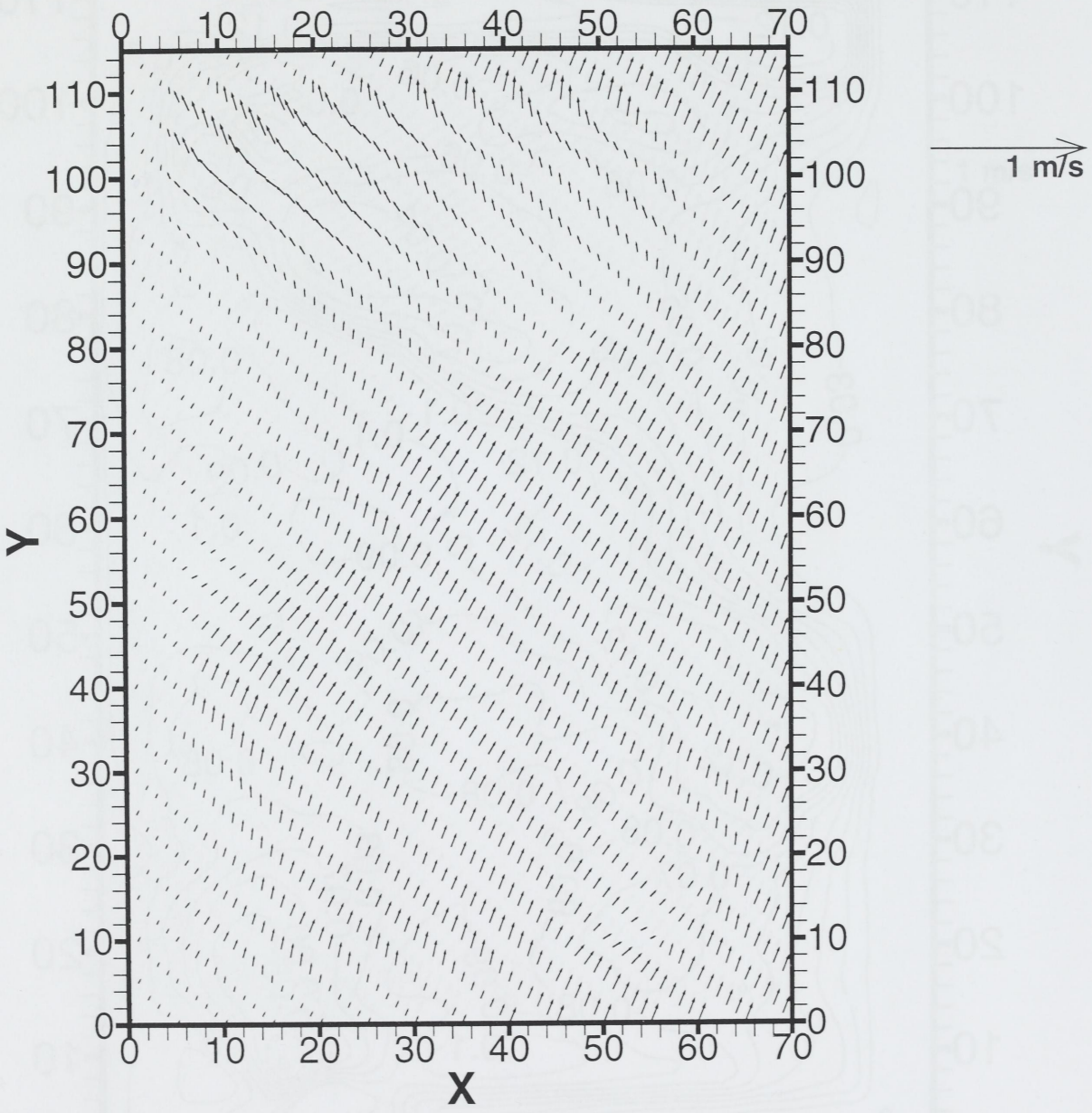

Figure 11: Vector plot of currents 50m above the bottom after 48 hours. Vectors are drawn from every 5th grid cell.

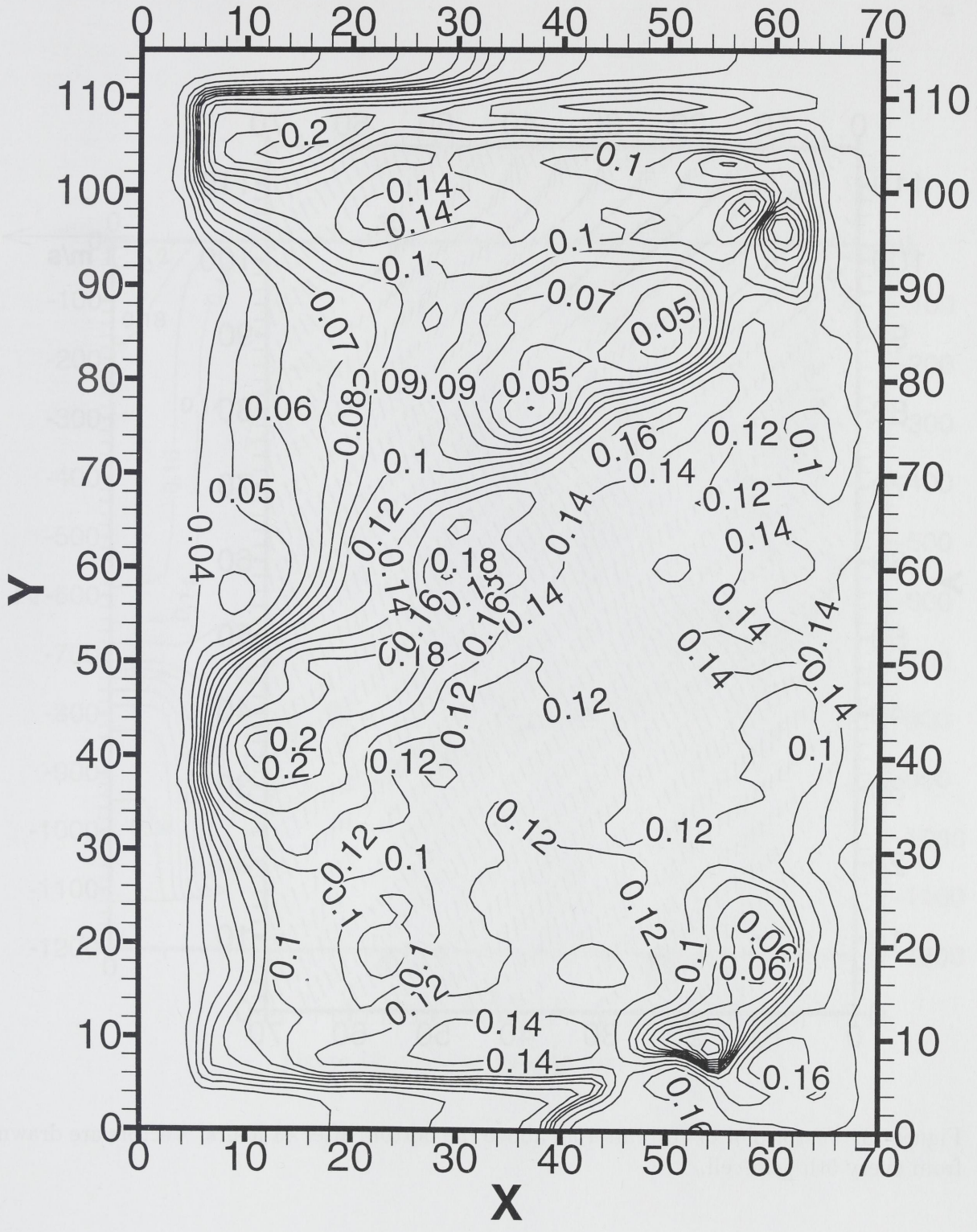

Figure 12: Current speeds 10m above the bottom after 48 hours.

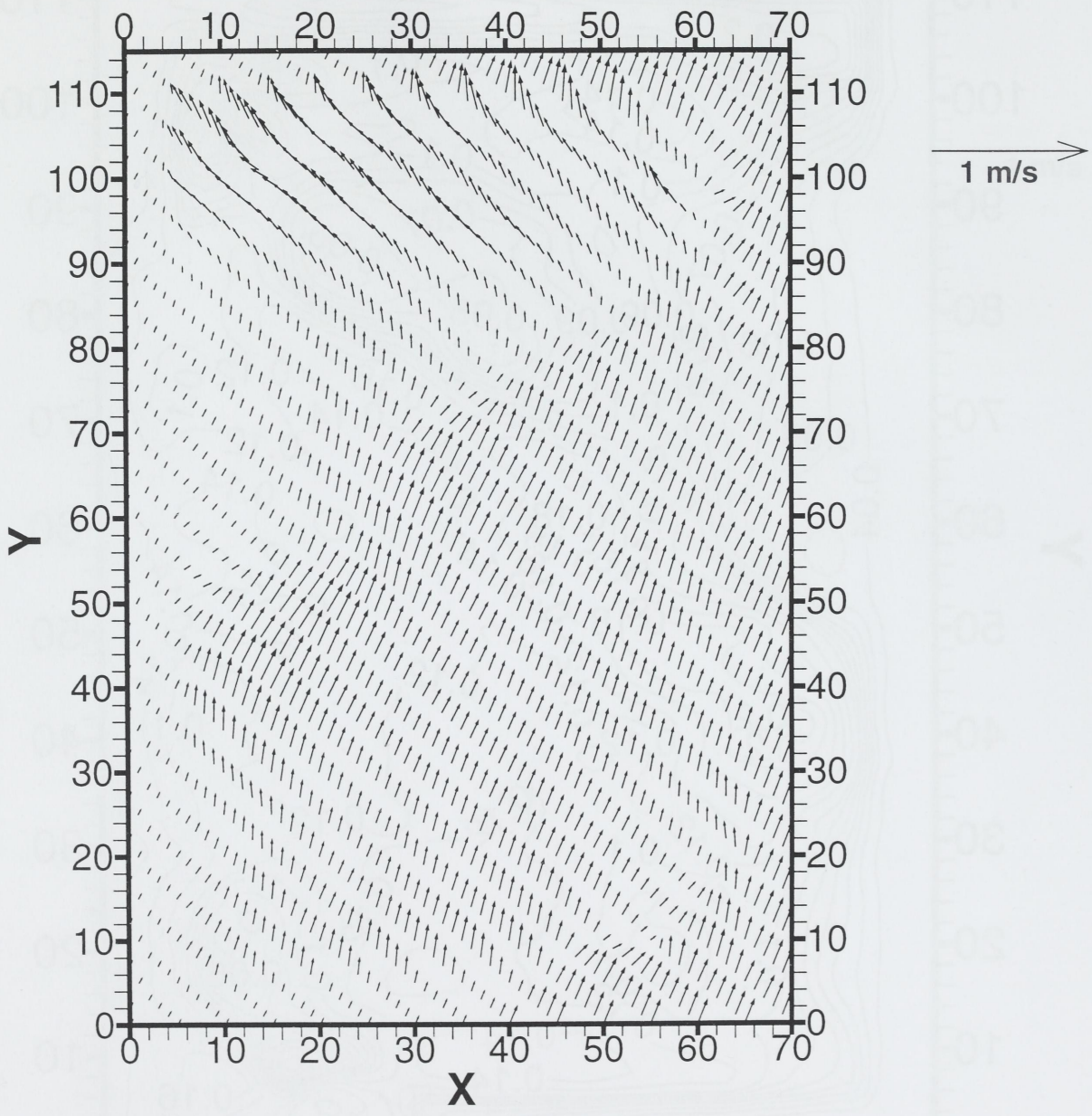

Figure 13: Vector plot of currents 10m above the bottom after 48 hours. Vectors are drawn from every 5th grid cell.

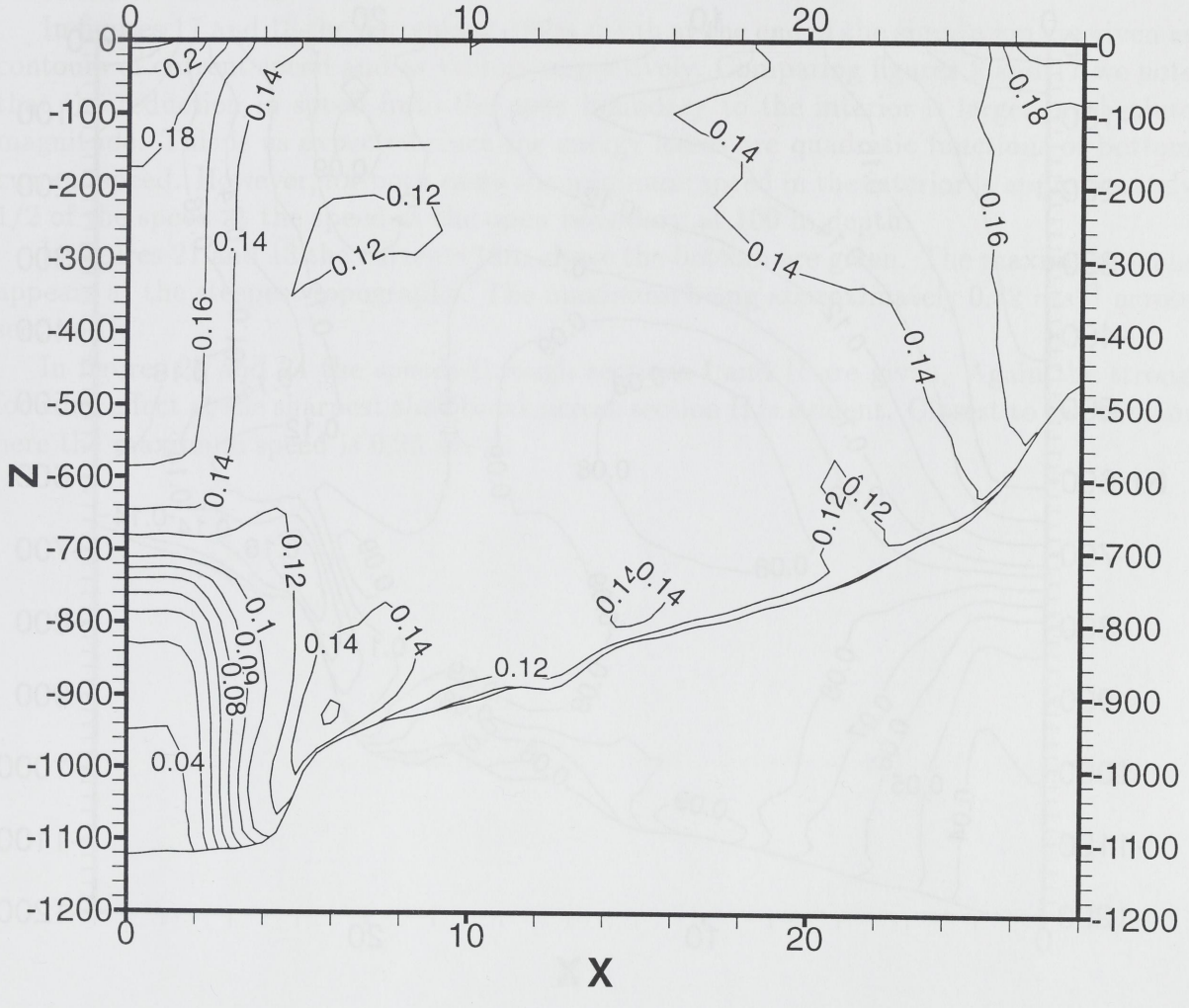

Figure 14: Current speeds at section I.

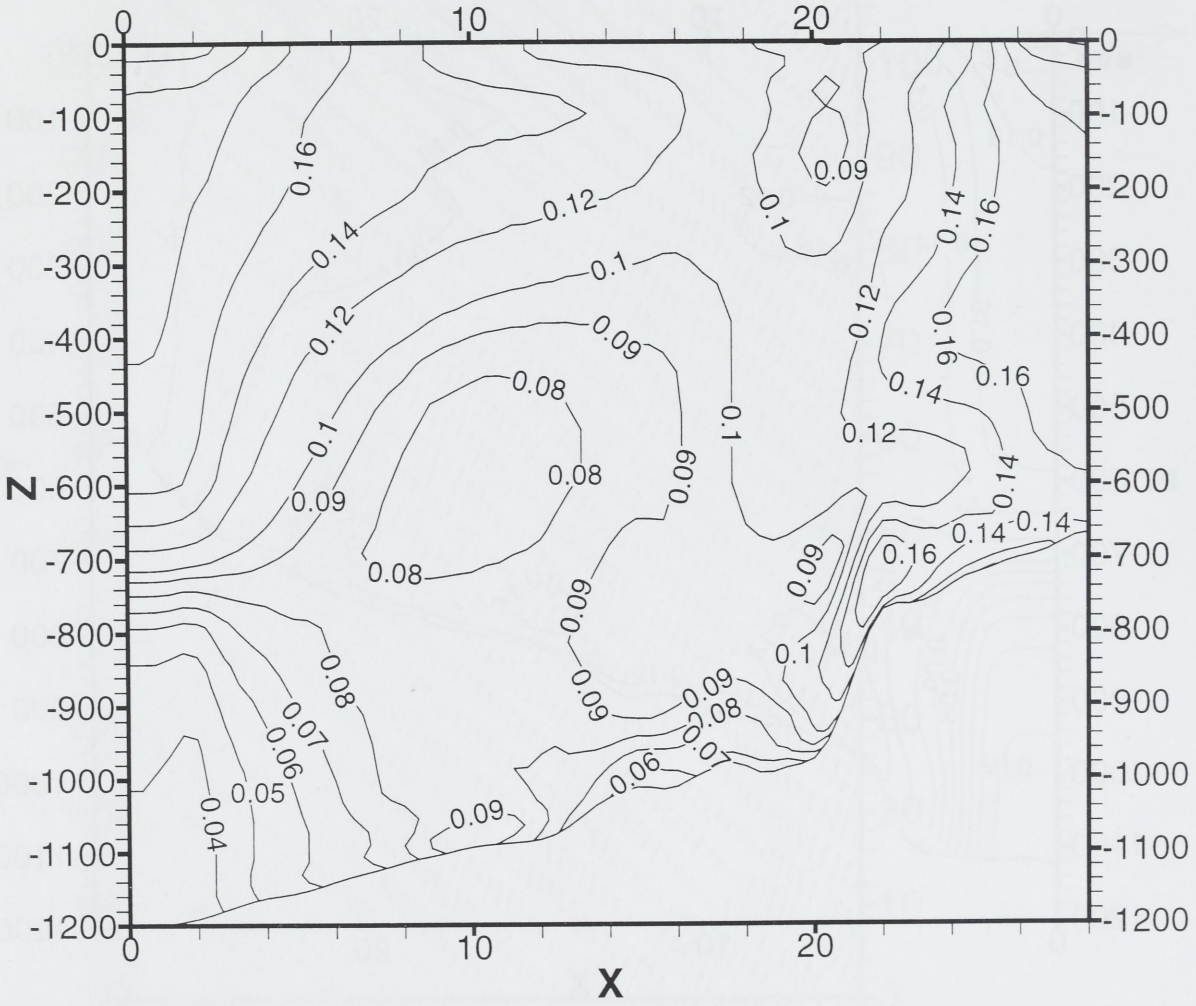

Figure 15: Current speeds at section II.

5.2 Numerical experiment 2

In the second experiment the only modification is that all velocities used as initial and boundary conditions in experiment 1 are multiplied by 2.

In Figure 16 the average kinetic energy over the model area is given as a function of time. We notice that the energy stabilizes at approximately 36 Jm^{-3} which is 4 times higher than in the previous experiment. This is as expected since energies are quadratic functions of velocities.

In figures 17 and 18 the currents at 100m depth at the end of the simulation are given as contours of current speed and as vectors respectively. Comparing figures 8 and 17 we note that the reduction in speed from the open boundary to the interior is larger in absolute magnitude. This is as expected since the energy losses are quadratic functions of bottom current speed. However, for both cases the minimum speed in the interior is approximately 1/2 of the speed at the speed at the open boundary at 100 m depth.

In figures 21 and 13 the currents 10m above the bottom are given. The maximum again appears at the steepest topography. The maximum being approximately 0.32 ms^{-1} across section II.

In figures 23 and 24 the speeds through sections I and II are given. Again the strong focusing effect at the sharpest shelf break across section II is evident. Closest to the bottom here the maximum speed is 0.35 ms^{-1}.

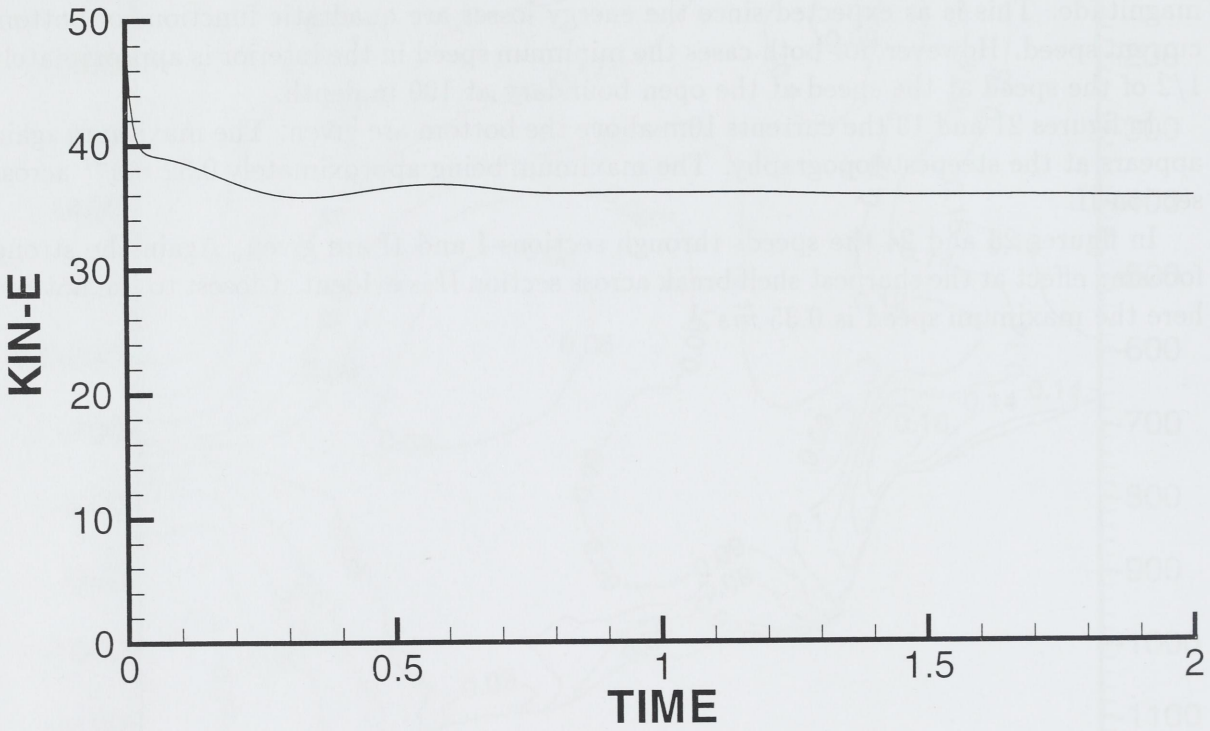

Figure 16: Volume averaged kinetic energy in Jm^{-3} as a function of time in days.

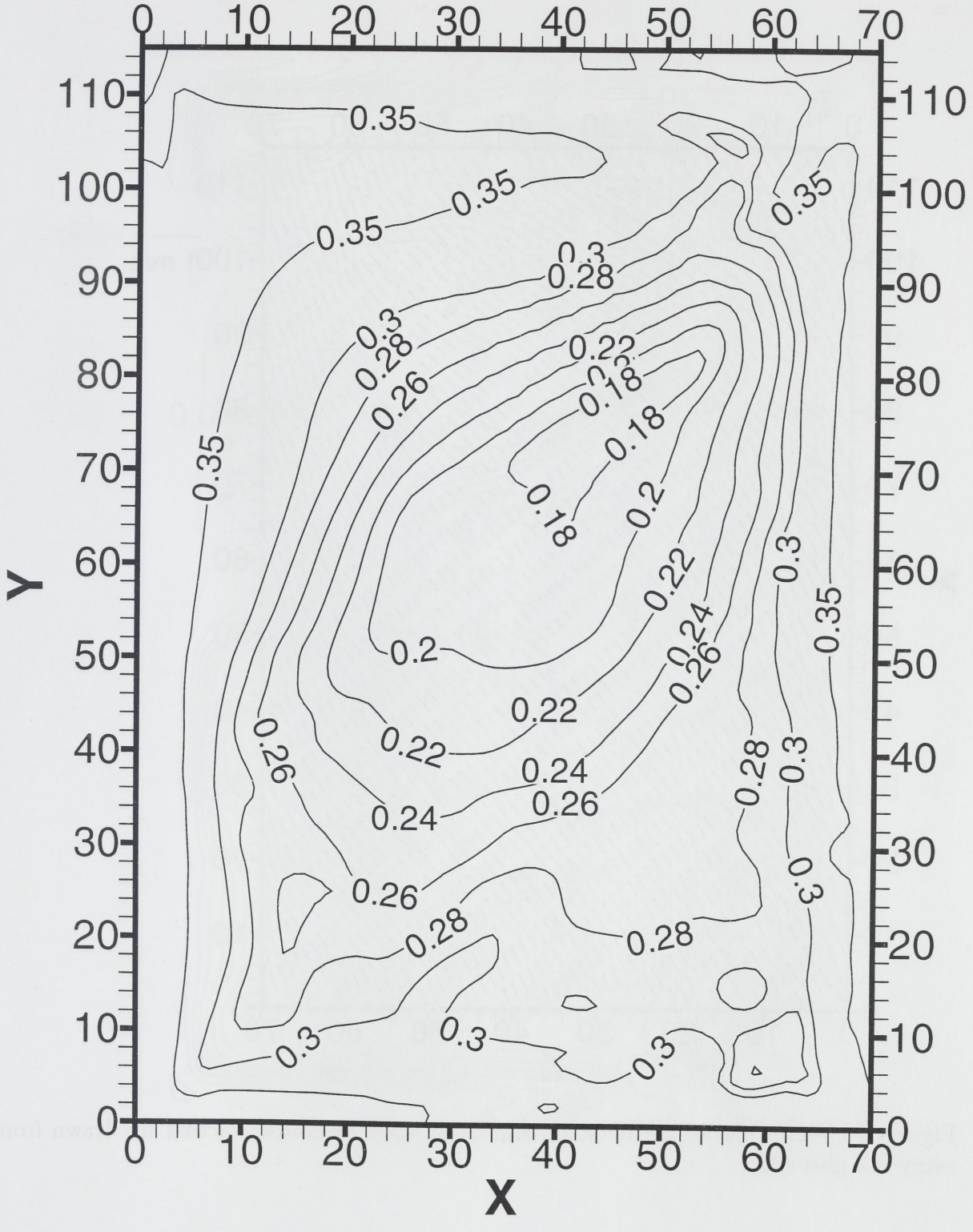

Figure 17: Current speeds at 100m depth after 48 hours.

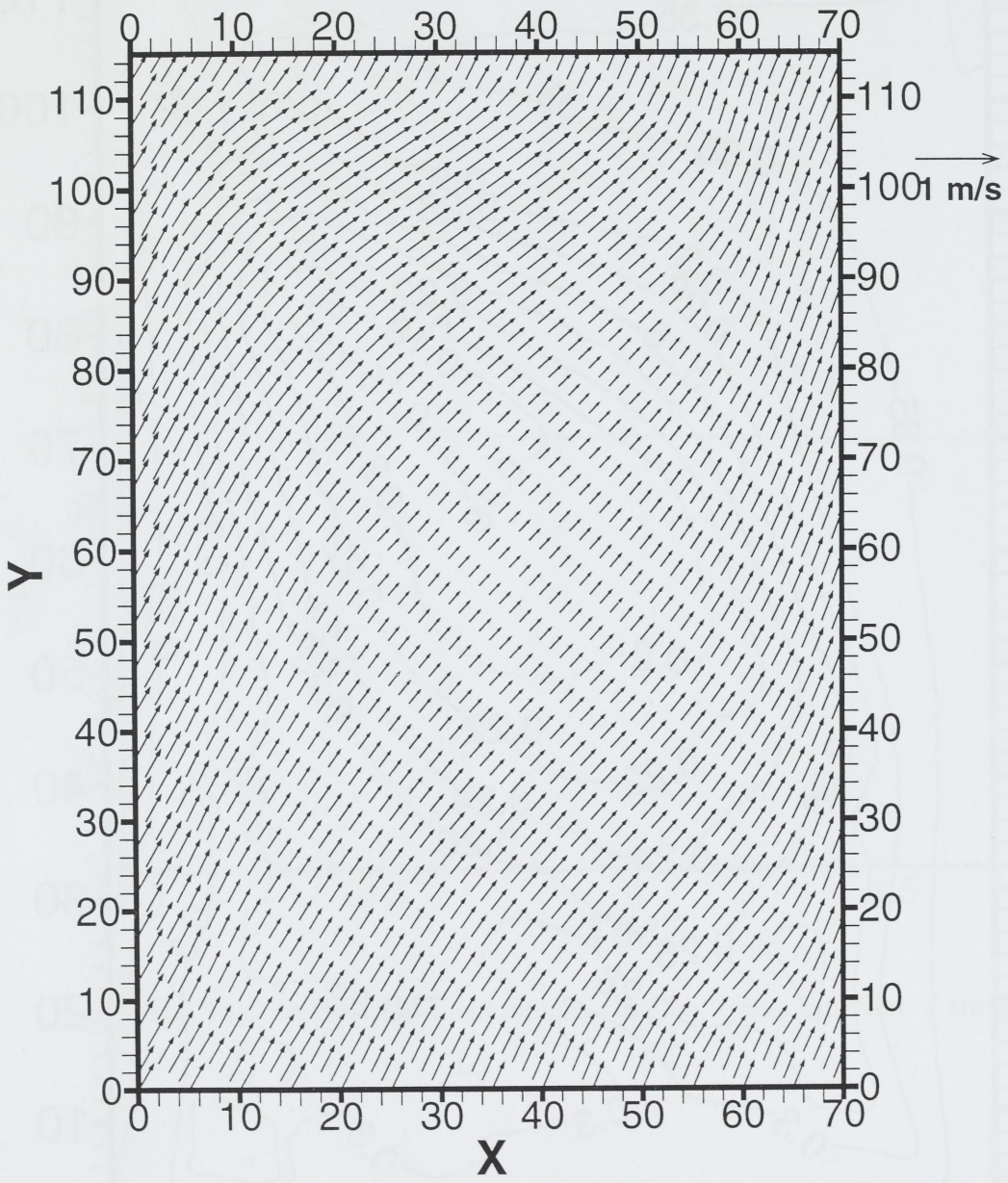

Figure 18: Vector plot of currents at 100m depth after 48 hours. Vectors are drawn from every 5th grid cell.

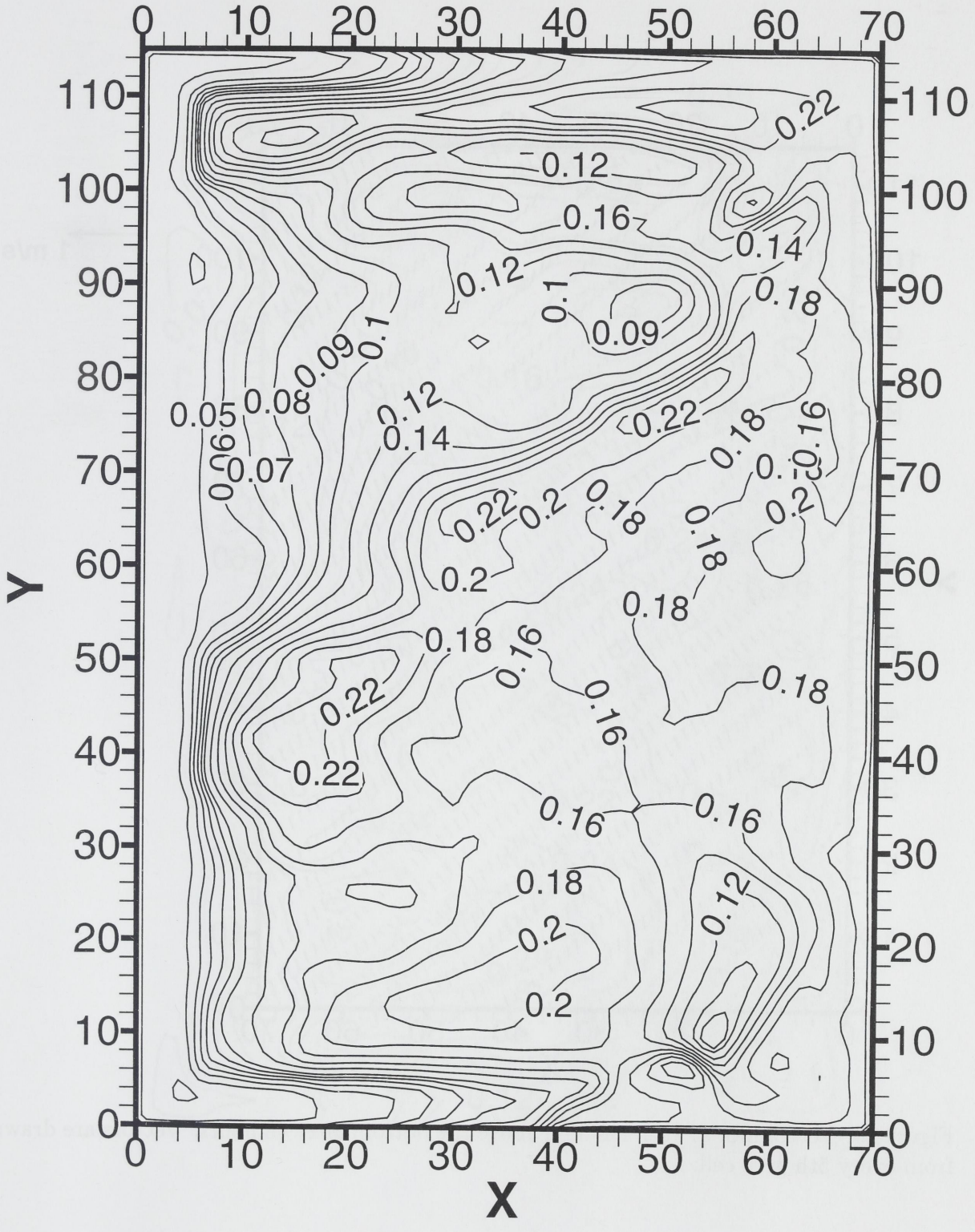

Figure 19: Current speeds 50m above the bottom after 48 hours.

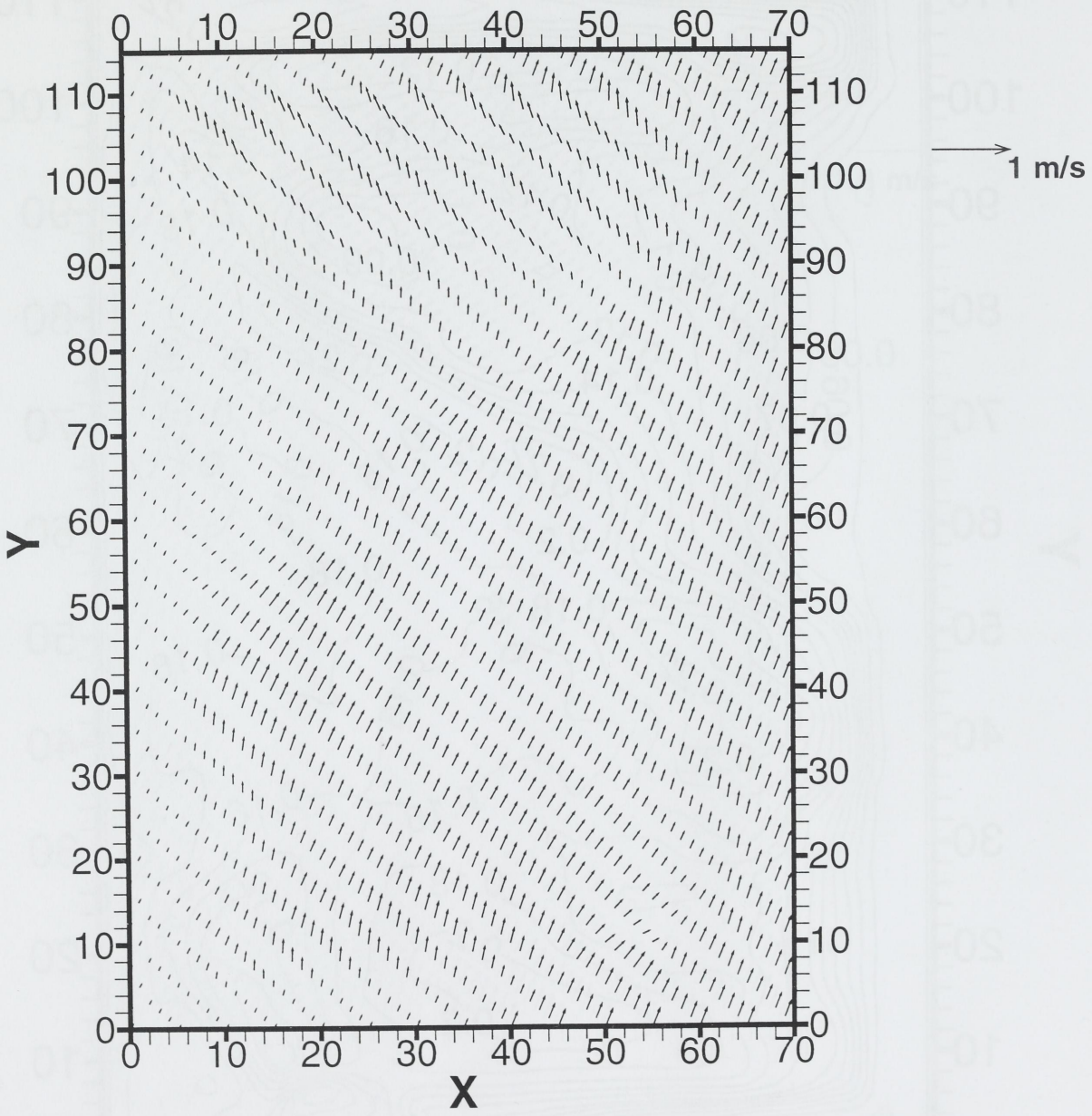

Figure 20: Vector plot of currents 50m above the bottom after 48 hours. Vectors are drawn from every 5th grid cell.

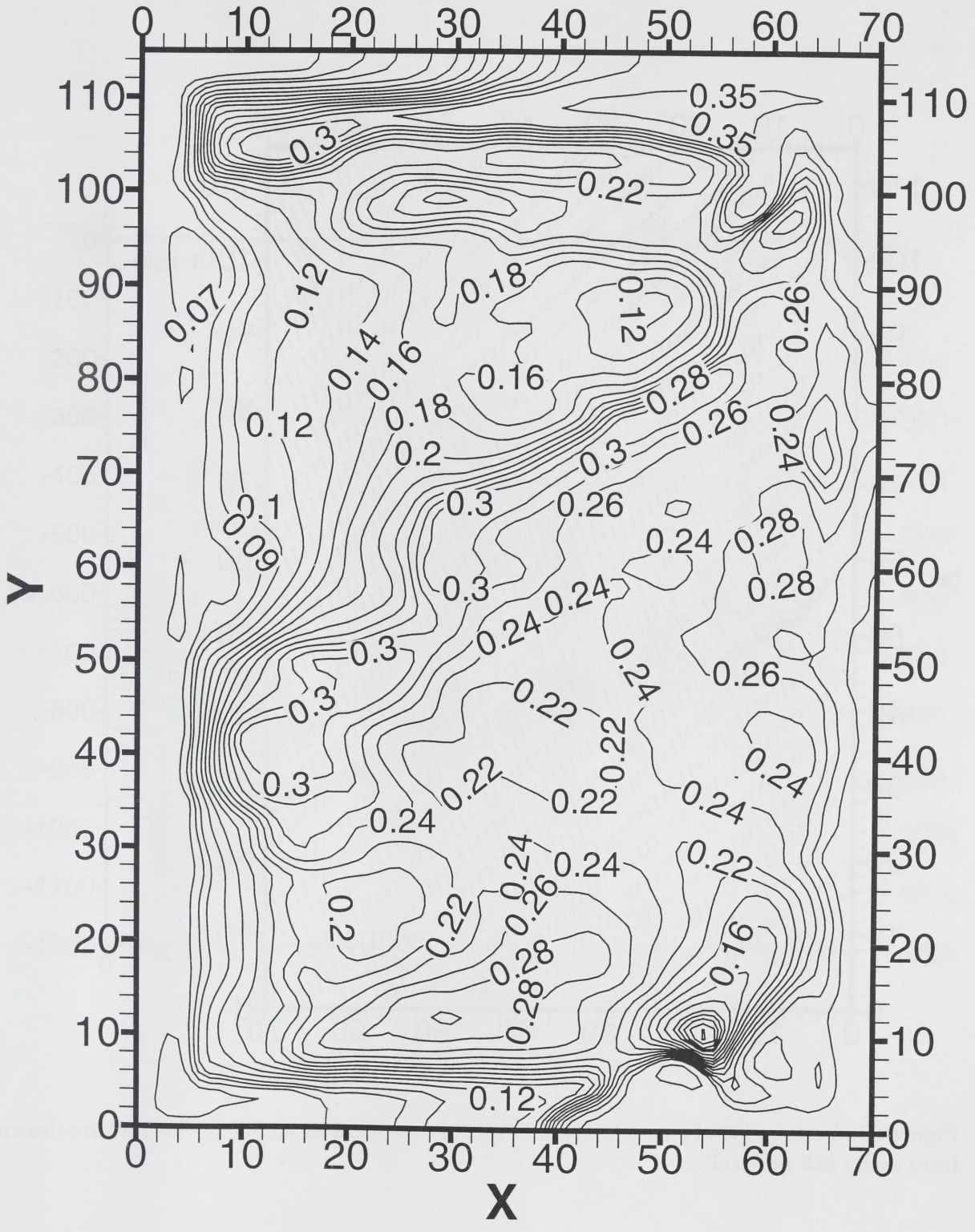

Figure 21: Current speeds 10m above the bottom after 48 hours.

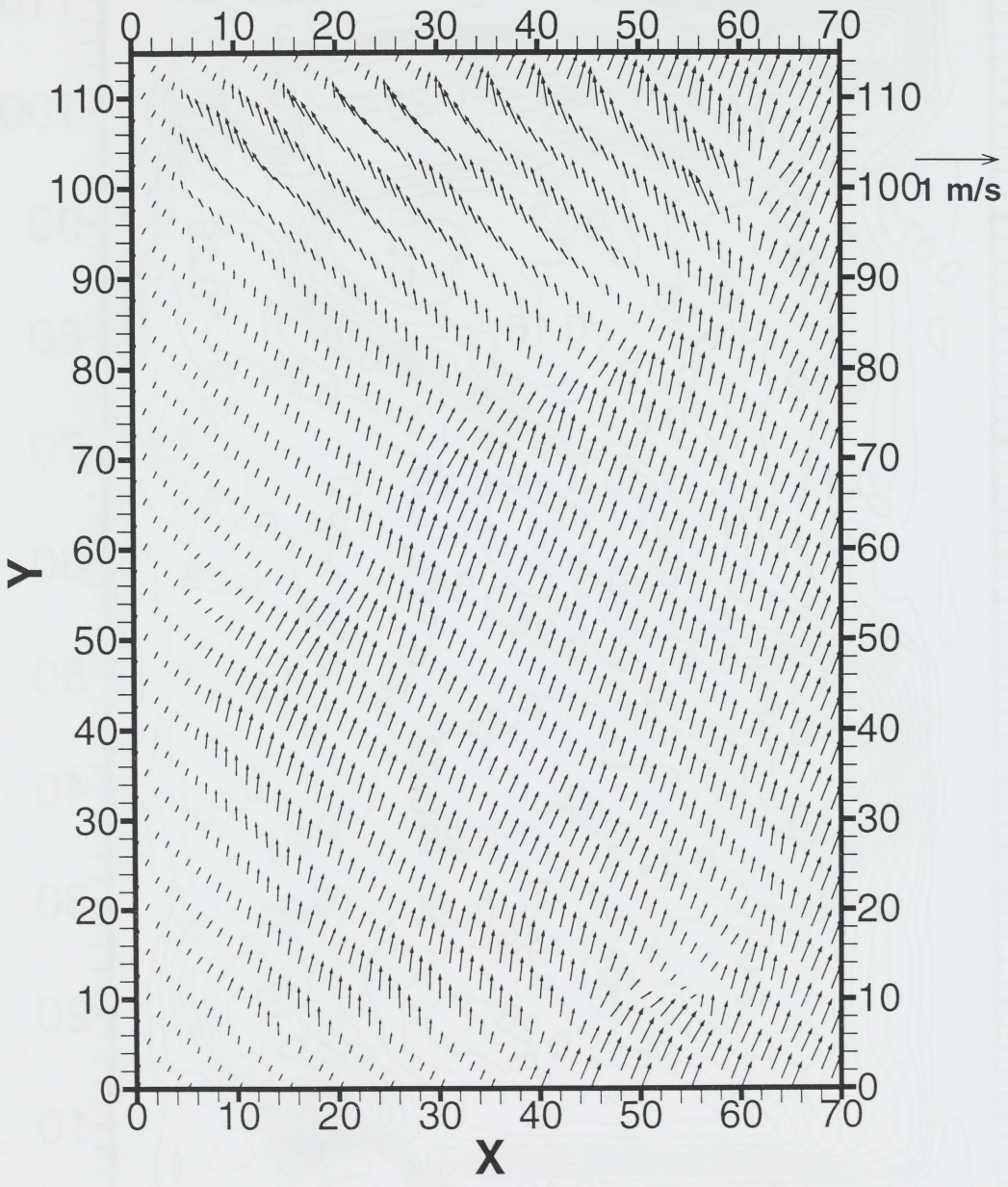

Figure 22: Vector plot of currents 10m above the bottom after 48 hours. Vectors are drawn from every 5th grid cell.

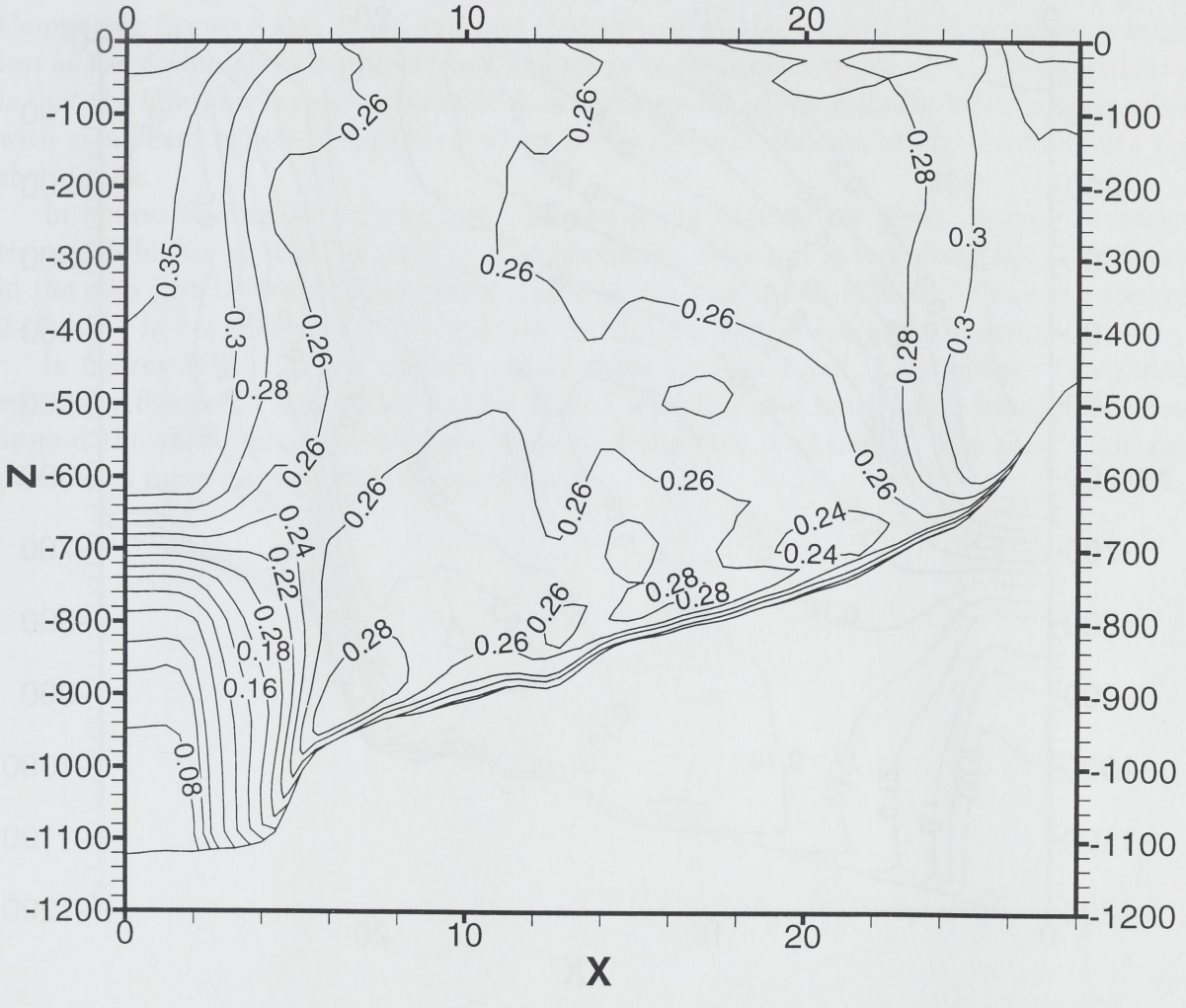

Figure 23: Current speeds at section I.

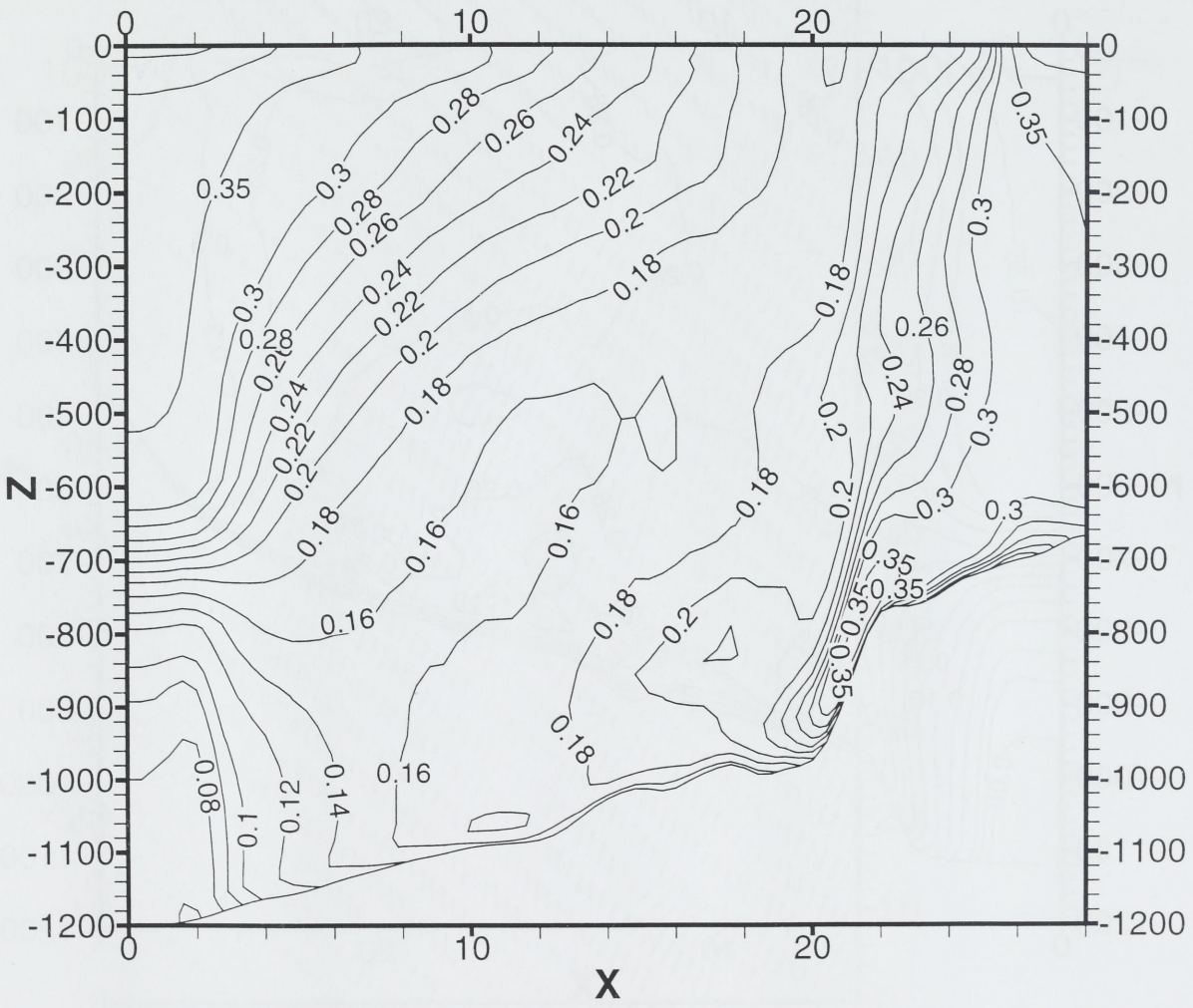

Figure 24: Current speeds at section II.

5.3 Numerical experiment 3

In the third experiment the only modification compared to experiment 1 is that all currents used as initial and boundary conditions in experiment 1 are rotated more towards the east and are now making a 60 degree angle with the south-north axis. This means that the flow now to a larger extent becomes cross shelf instead of along shelf.

The average kinetic energies develop very much as in experiment 1 and after 48 hours the solution is stationary. In figures 25 and 26 the currents at 100m depth are given. Comparing figures 8 and 25 we now find that the reduction in speed in the interior is much less as the flow angle is modified from 30 degrees to 60 degrees north east. The explanation is that the flow now is more cross shelf than along shelf and the distance traveled over areas with significant effects of bottom friction becomes much shorter before the flow hits the shelf break.

In figures 29 and 30 the currents 10m above the bottom are given. Again we notice the much higher spatial variability. The maximum values of speed along the shelf break in the area just before the topography turns is now more than 0.20 ms^{-1} as compared to 0.16 ms^{-1} in experiment 1. The explanation is probably the one given above.

In figures 31 and 32 the current speeds along sections I and II are given. Comparing especially figures 15 and 32 for section II it is amazing how much more focused the flow around the shelf break gets as the direction of the flow is changed. The maximum also penetrates more deeply along the shelf break.

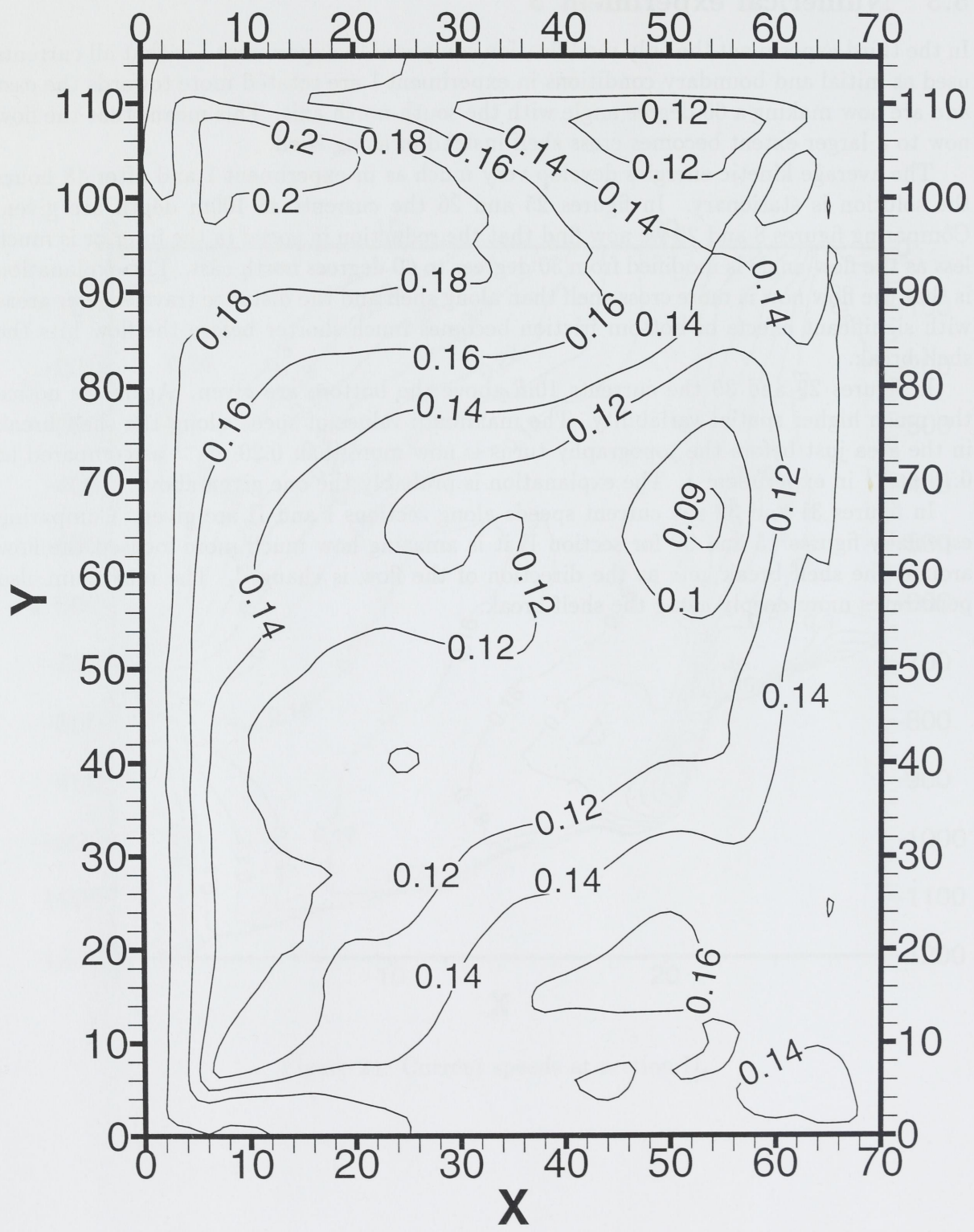

Figure 25: Current speeds at 100m depth after 48 hours.

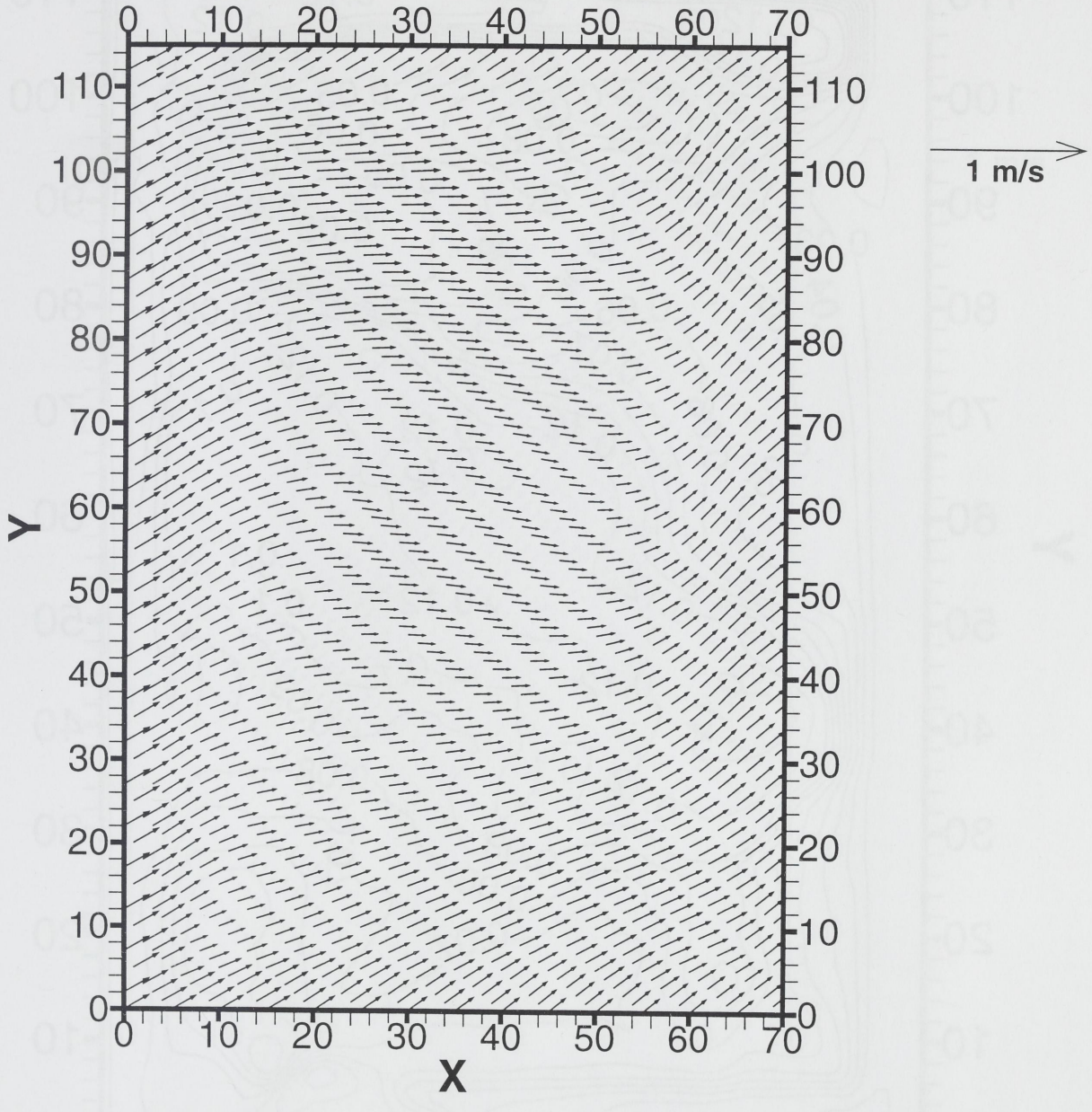

Figure 26: Vector plot of currents at 100m depth after 48 hours. Vectors are drawn from every 5th grid cell.

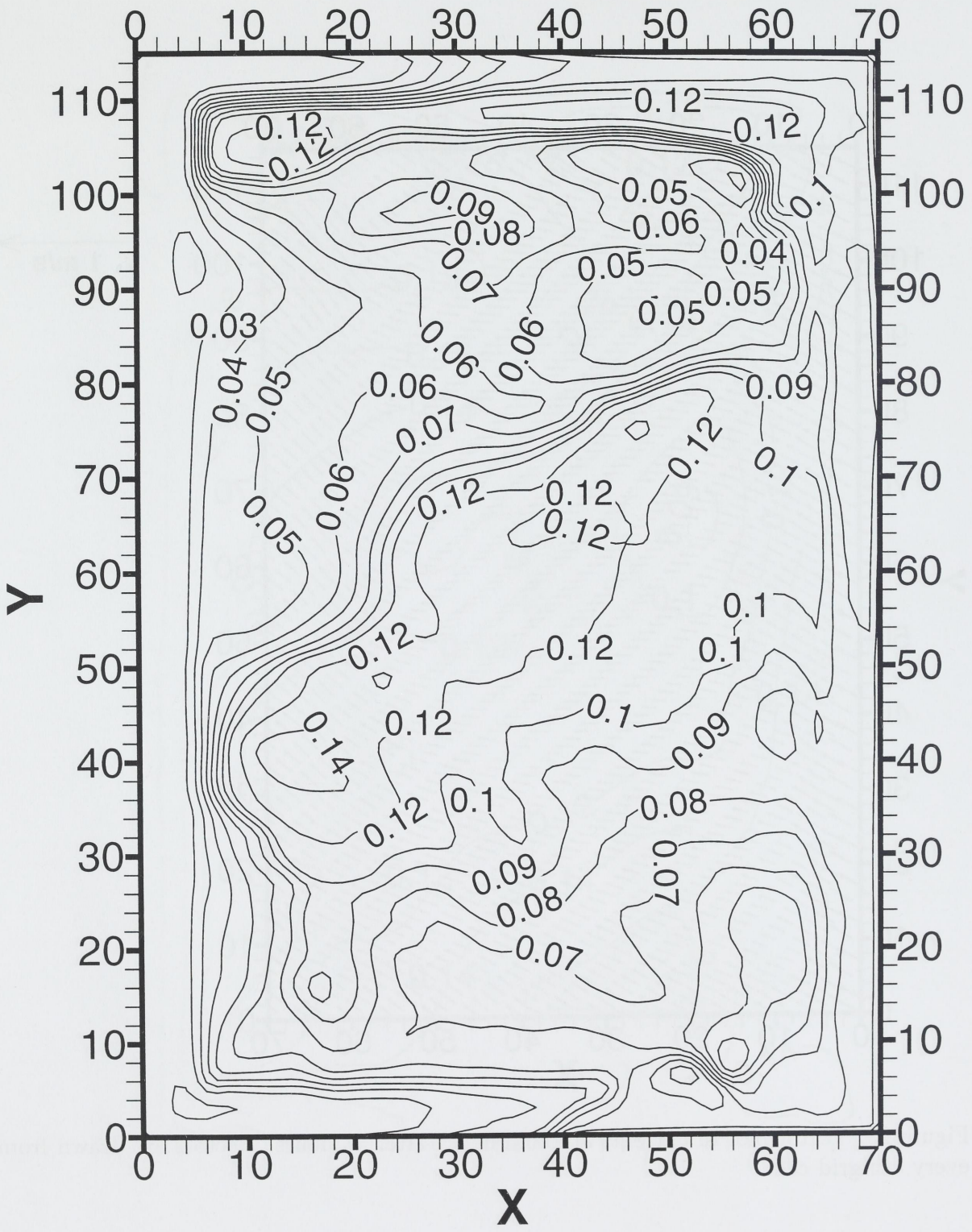

Figure 27: Current speeds 50m above the bottom after 48 hours.

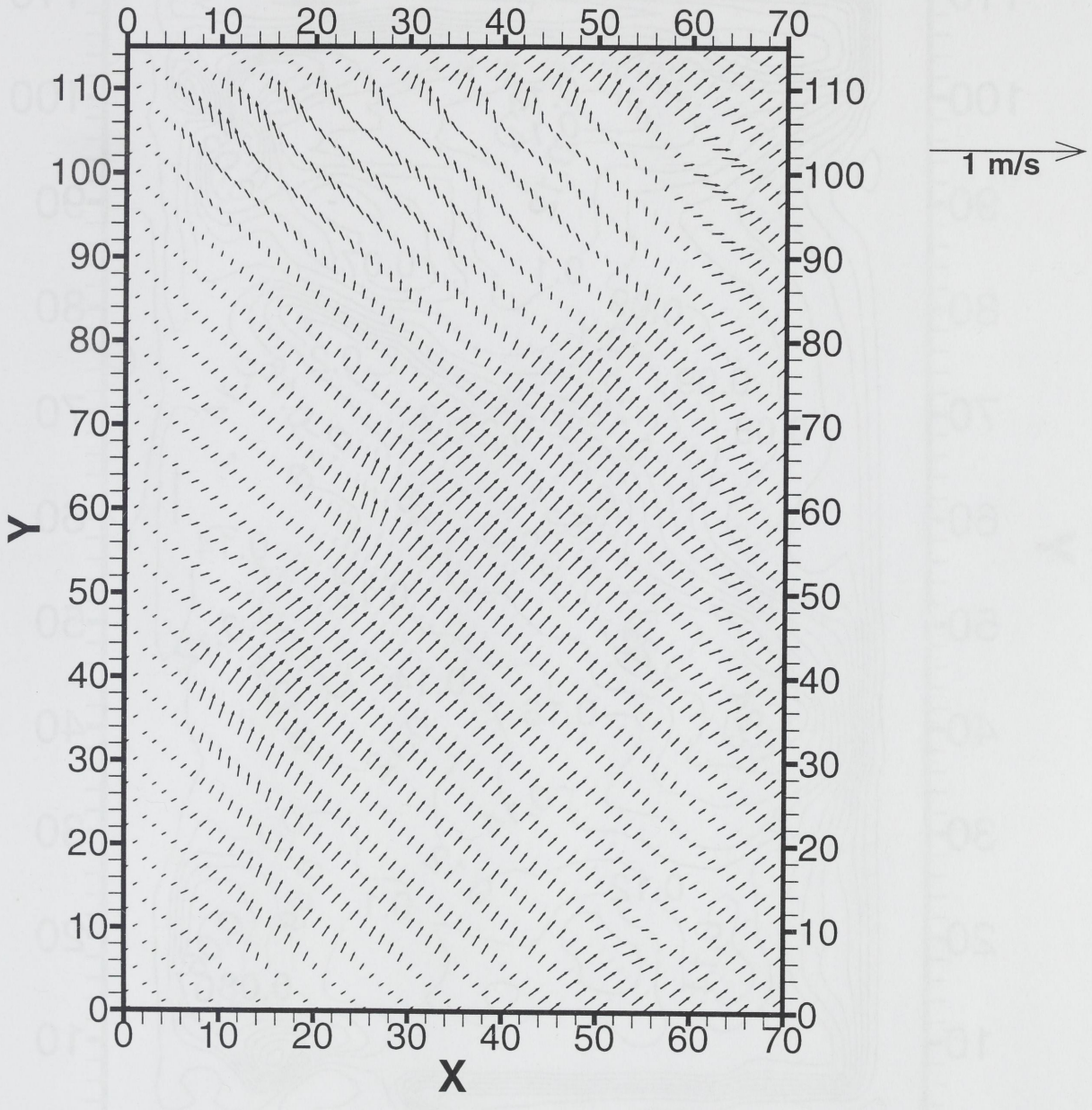

Figure 28: Vector plot of currents 50m above the bottom after 48 hours. Vectors are drawn from every 5th grid cell.

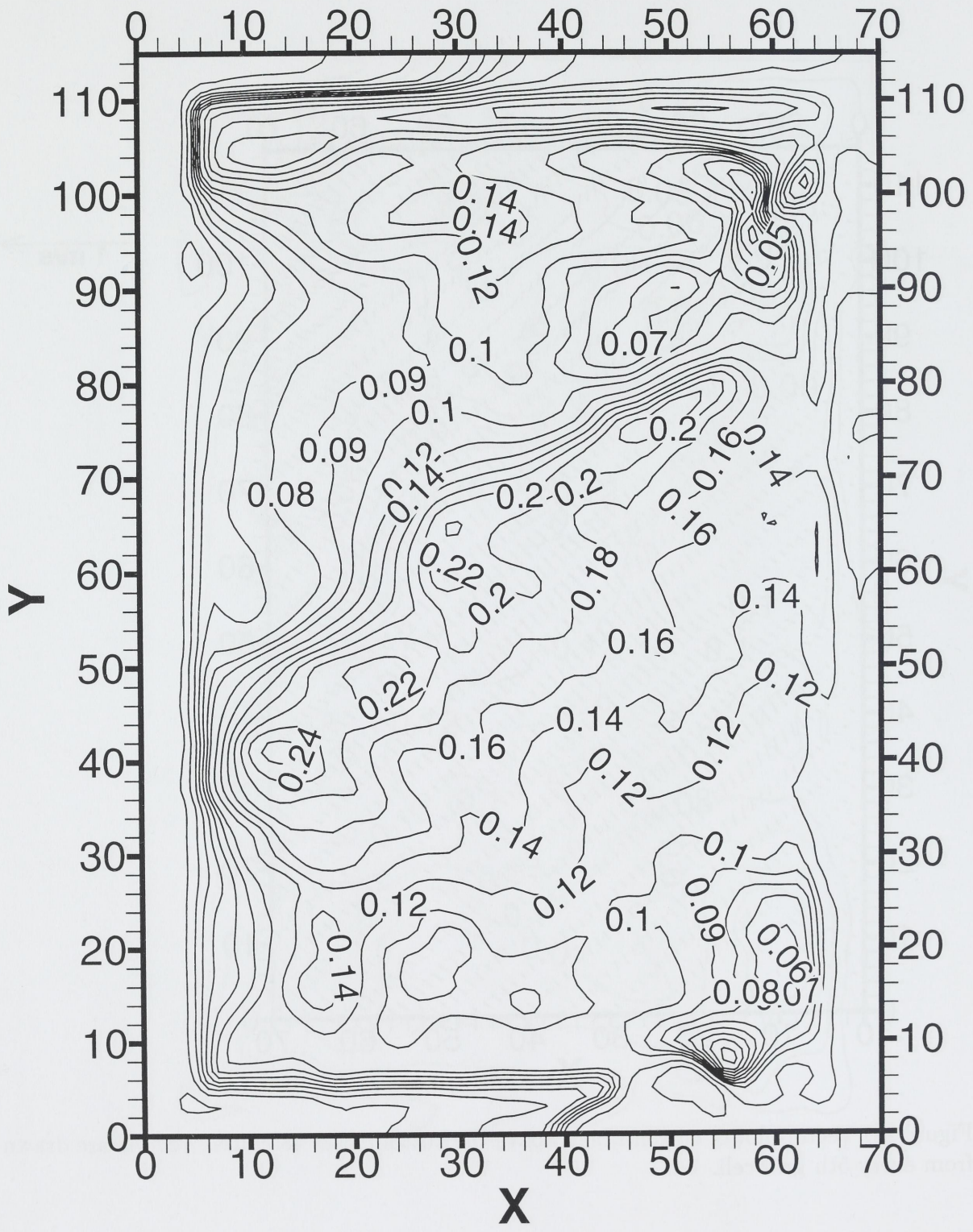

Figure 29: Current speeds 10m above the bottom after 48 hours.

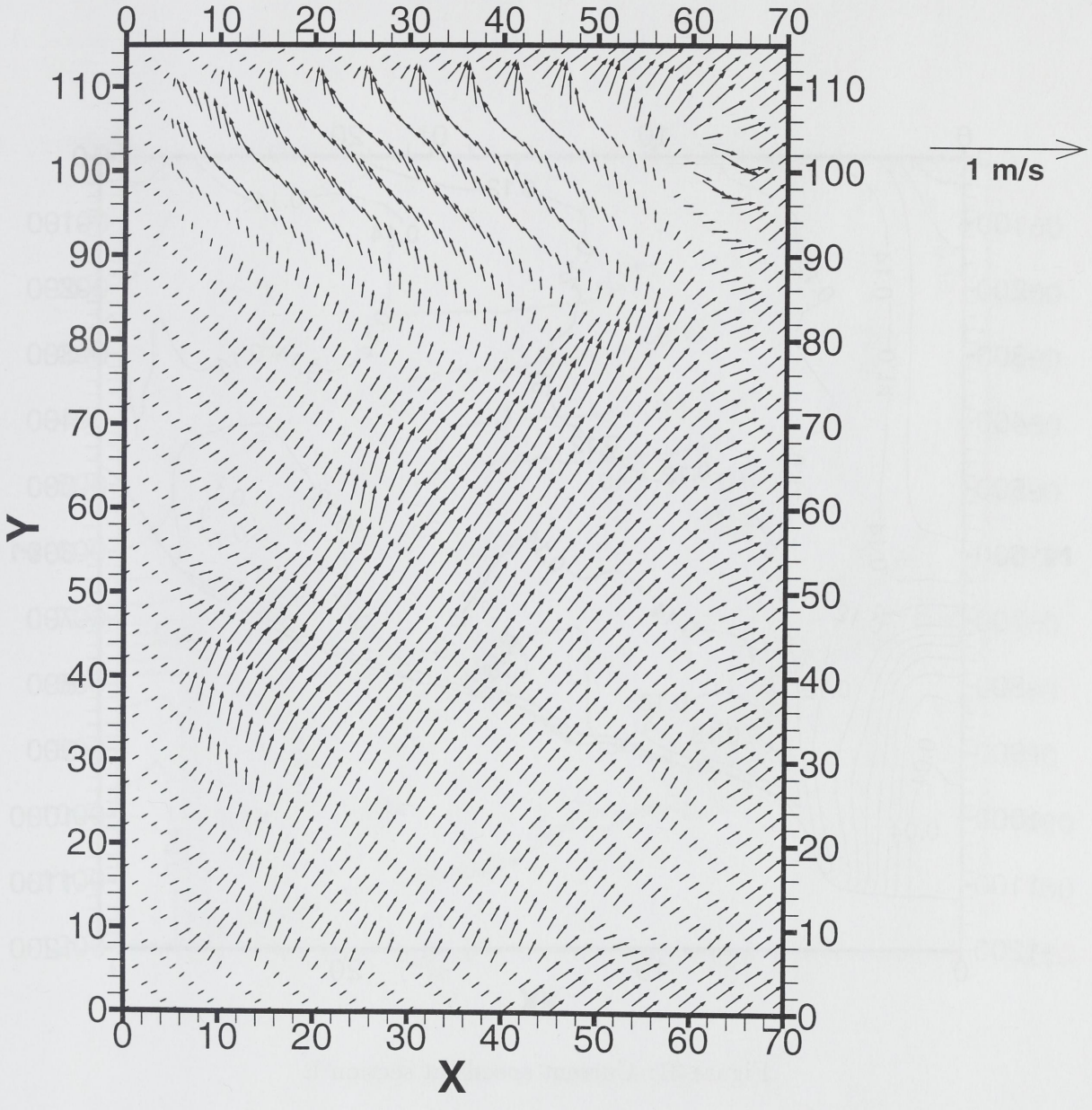

Figure 30: Vector plot of currents 10m above the bottom after 48 hours. Vectors are drawn from every 5th grid cell.

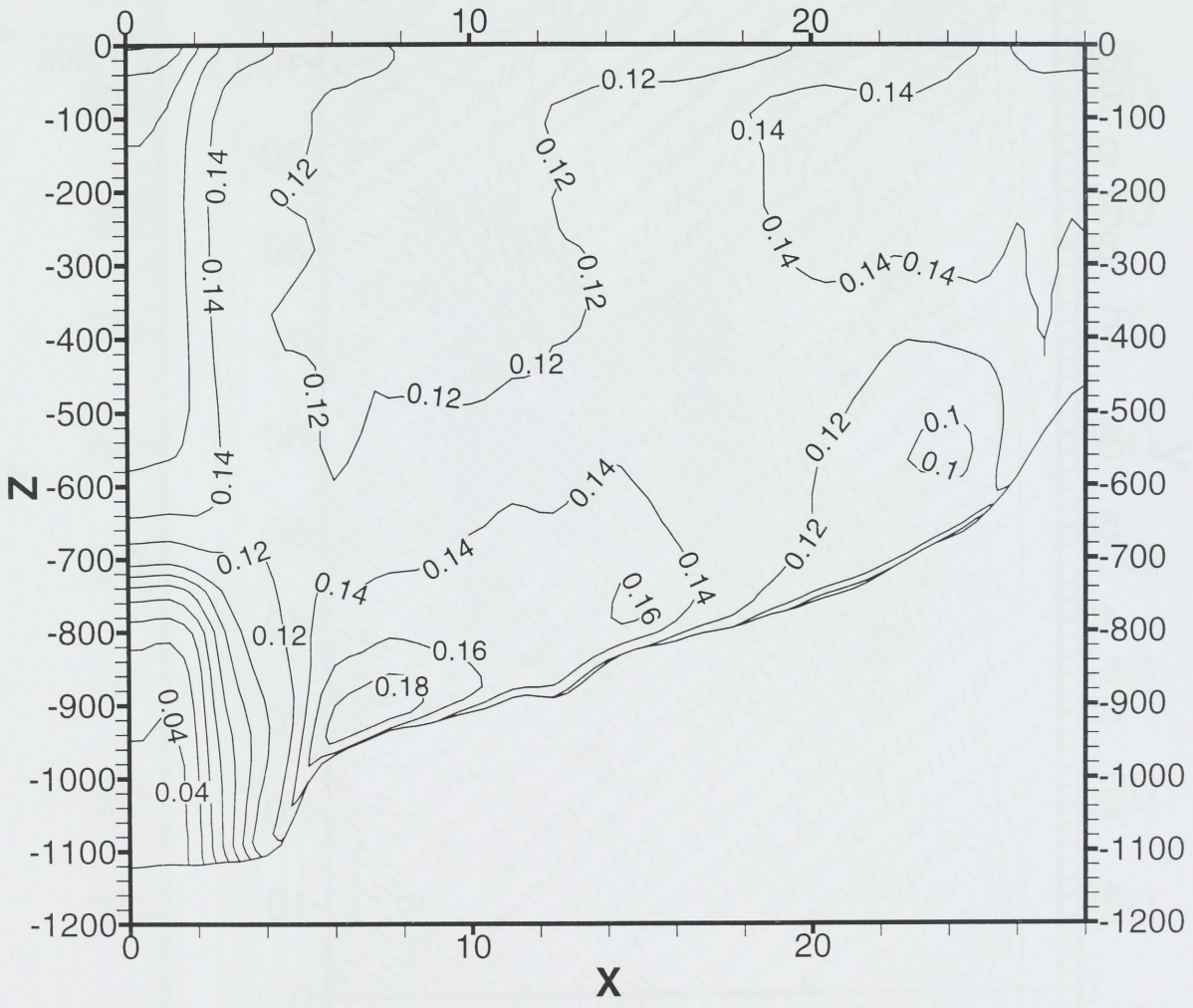

Figure 31: Current speeds at section I.

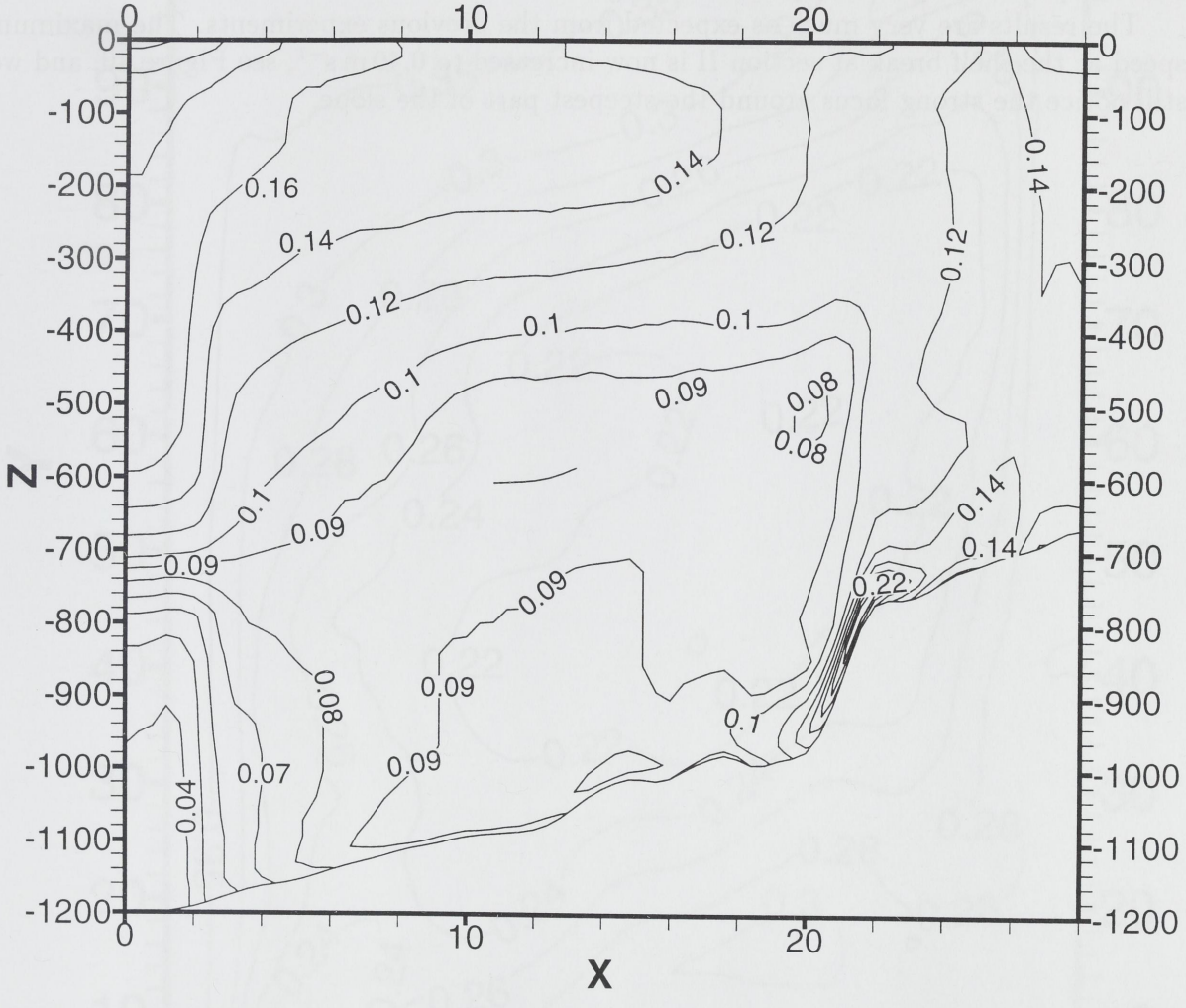

Figure 32: Current speeds at section II.

5.4 Numerical experiment 4

In the fourth experiment the only modification compared to the third experiment is that all velocities used as initial and boundary conditions in experiment 3 are multiplied by 2.

The average kinetic energies develop very much as in experiment 2 and after 48 hours the solution is stationary. In figures 33 and 34 the currents at 100m depth are given. In figures 37 and 38 the currents 10m above the bottom are given. In figures 39 and 40 the current speeds along sections I and II are given.

The results are very much as expected from the previous experiments. The maximum speed at the shelf break at section II is now increased to $0.40\,\mathrm{m\,s^{-1}}$, see Figure 40, and we still notice the strong focus around the steepest part of the slope.

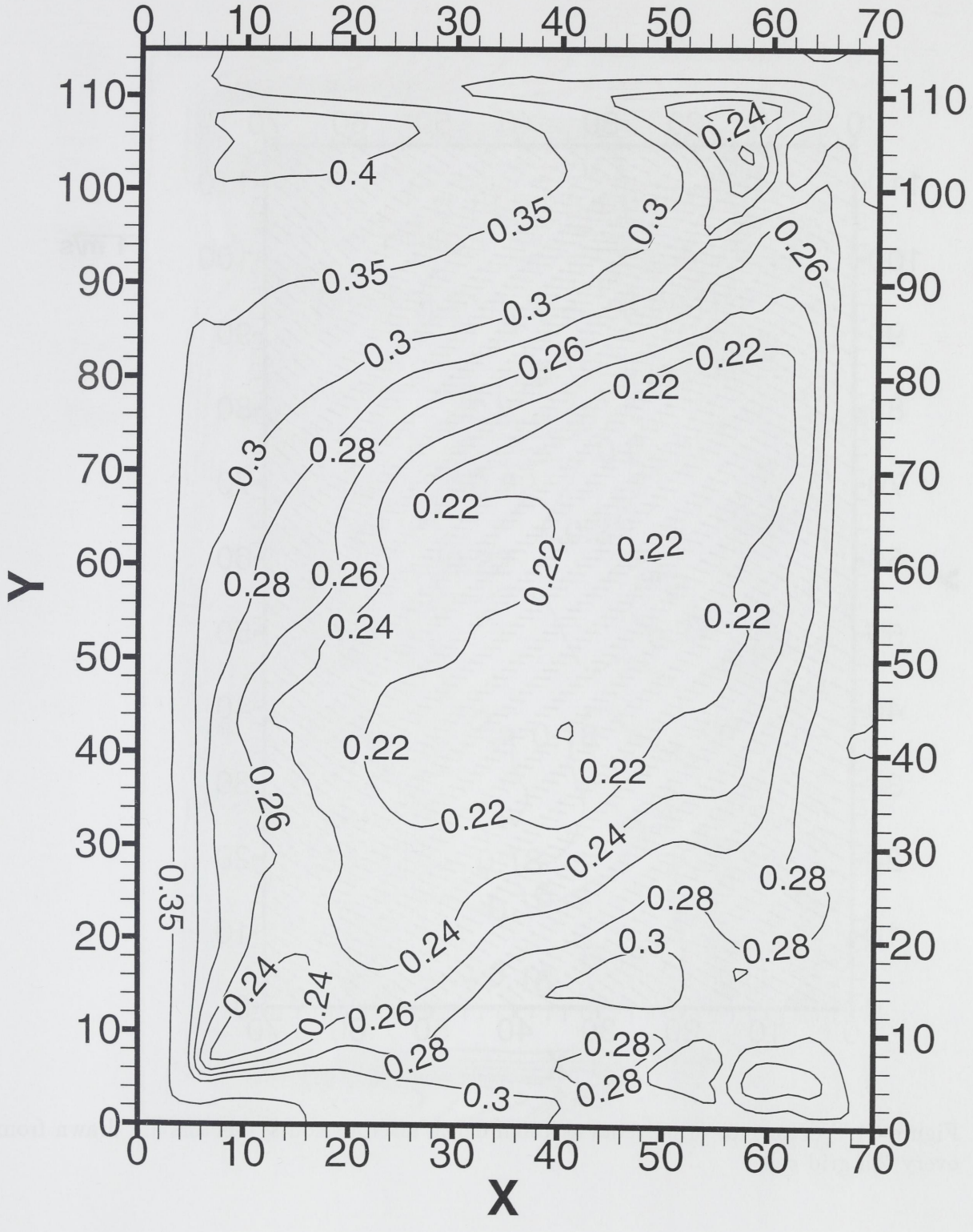

Figure 33: Current speeds at 100m depth after 48 hours.

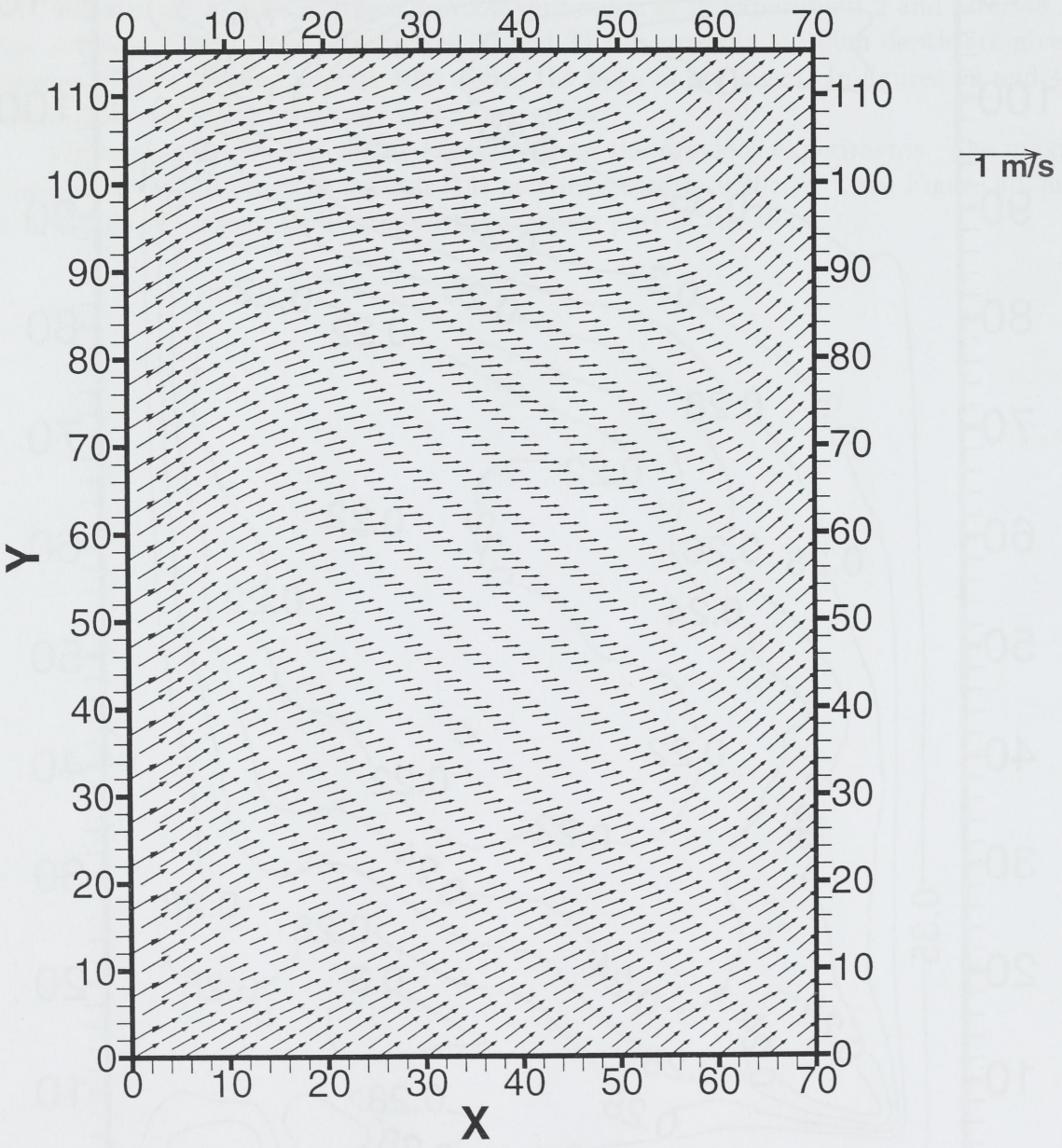

Figure 34: Vector plot of currents at 100m depth after 48 hours. Vectors are drawn from every 5th grid cell.

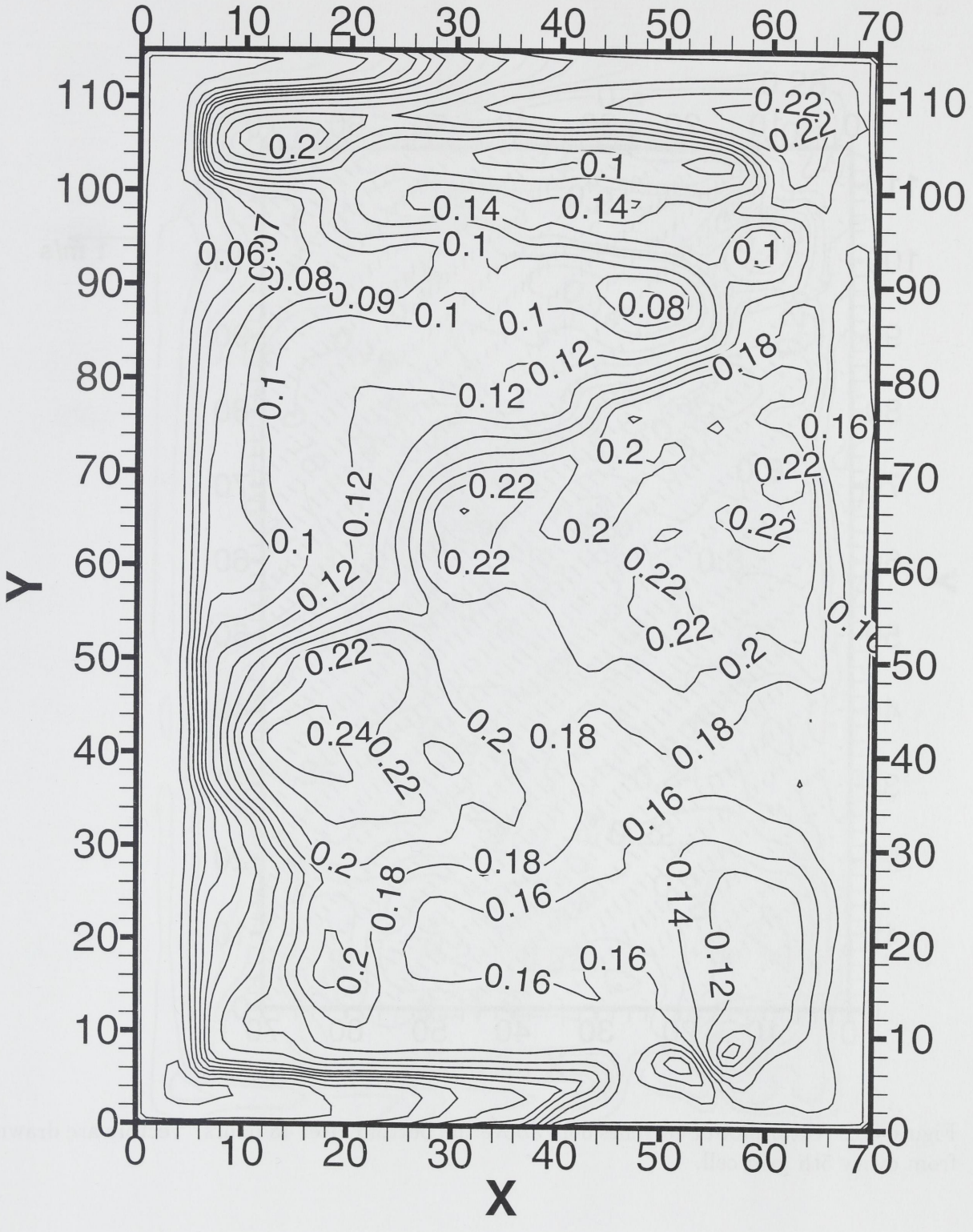

Figure 35: Current speeds 50m above the bottom after 48 hours.

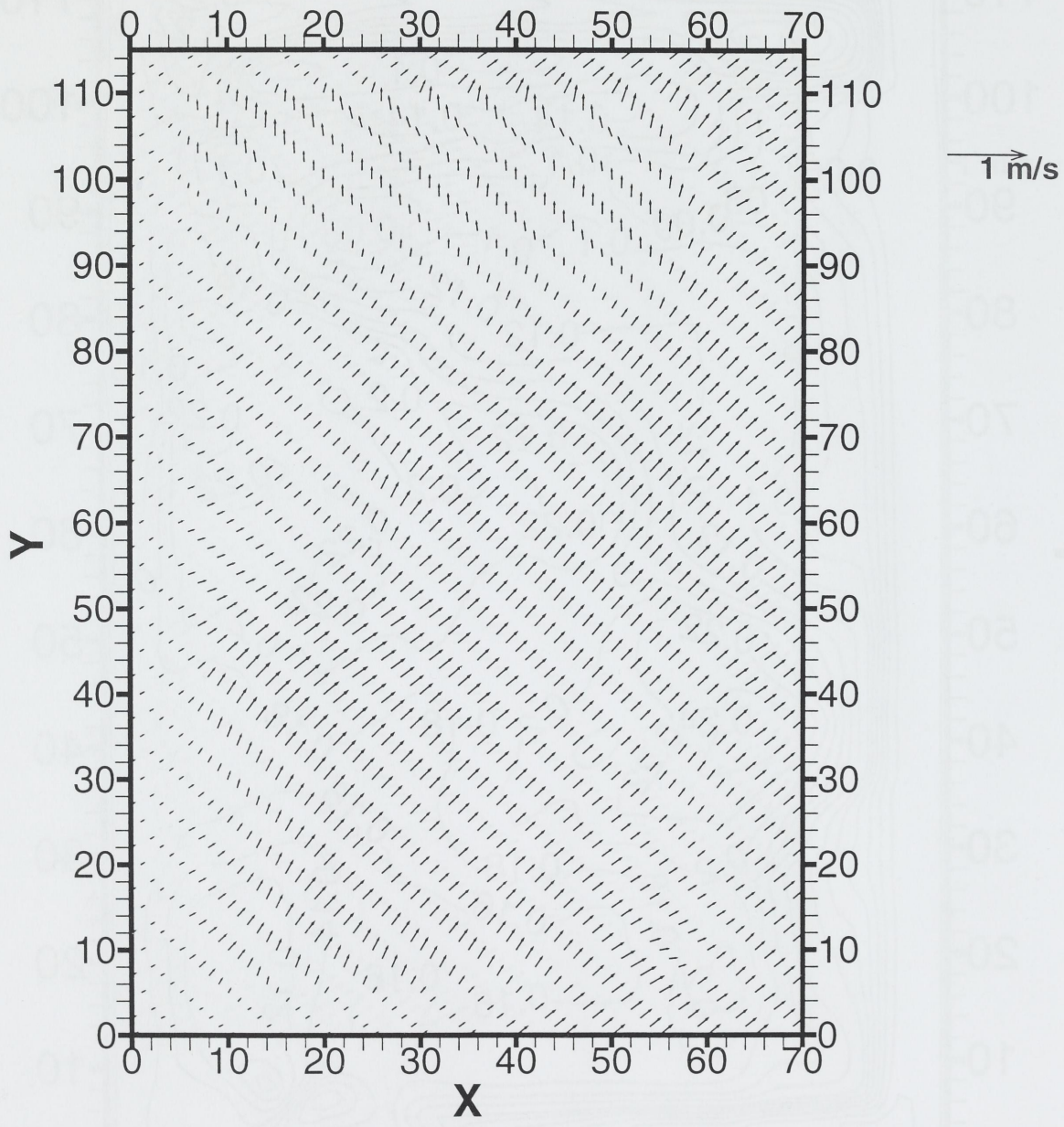

Figure 36: Vector plot of currents 50m above the bottom after 48 hours. Vectors are drawn from every 5th grid cell.

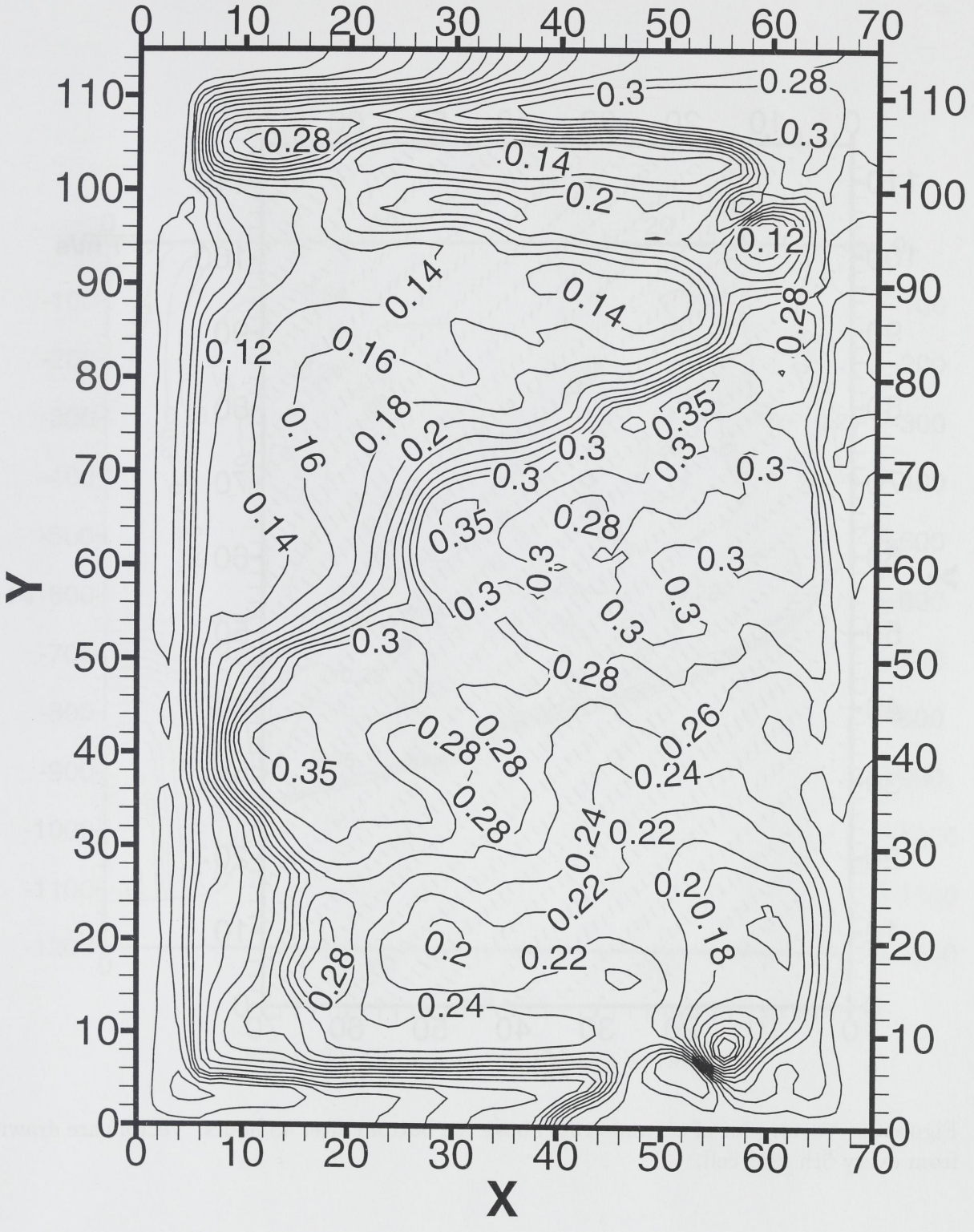

Figure 37: Current speeds 10m above the bottom after 48 hours.

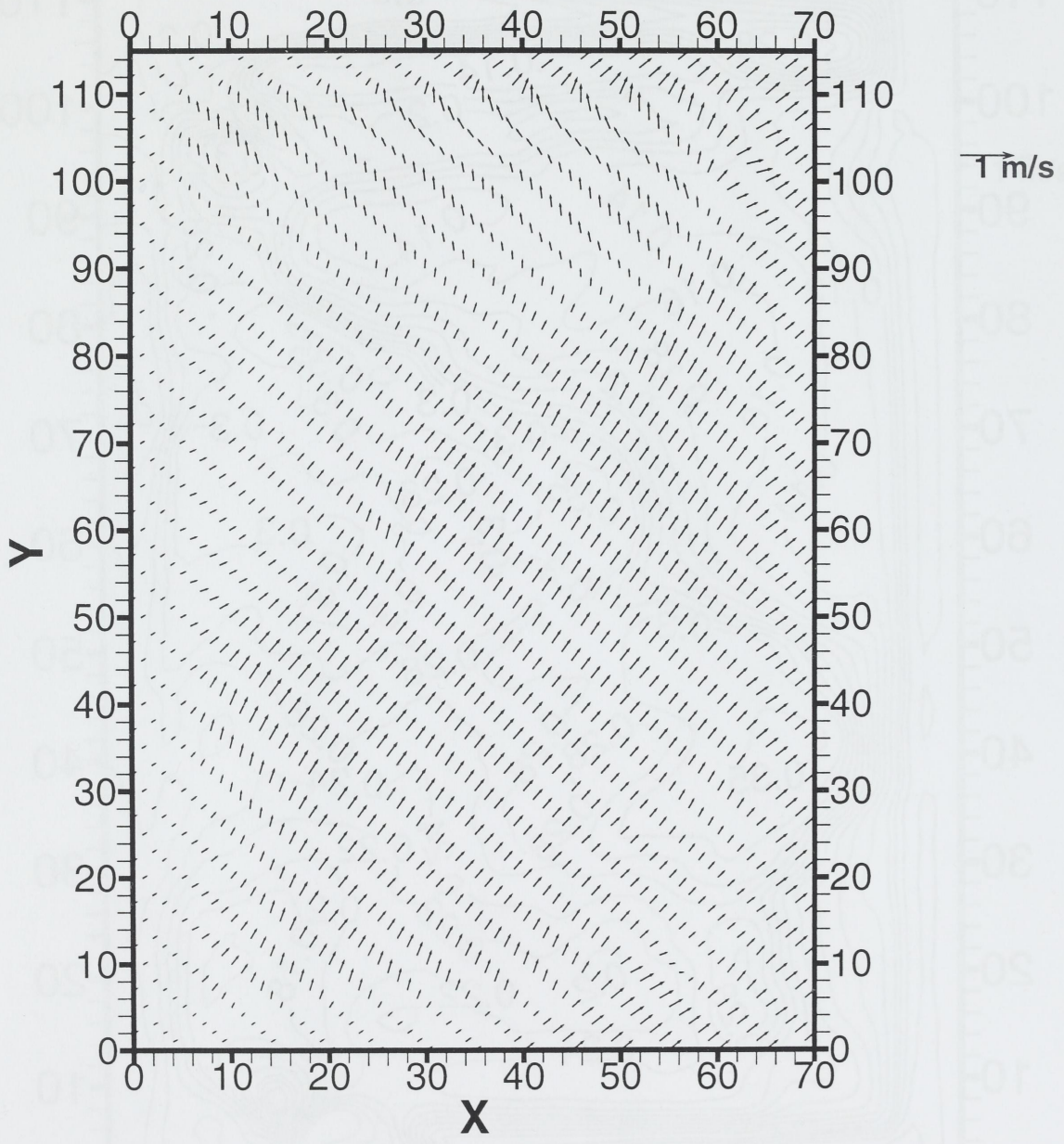

Figure 38: Vector plot of currents 10m above the bottom after 48 hours. Vectors are drawn from every 5th grid cell.

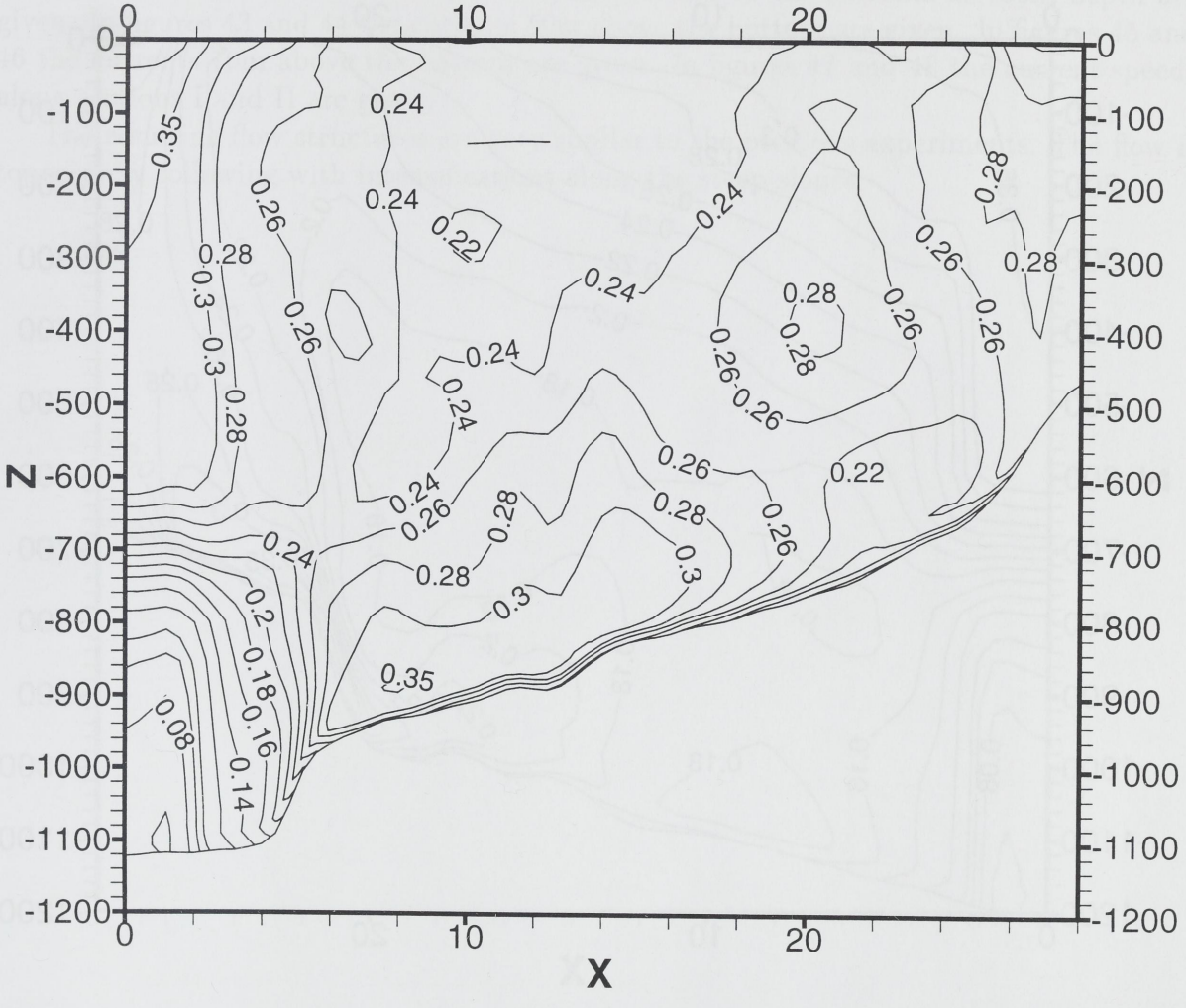

Figure 39: Current speeds through section I.

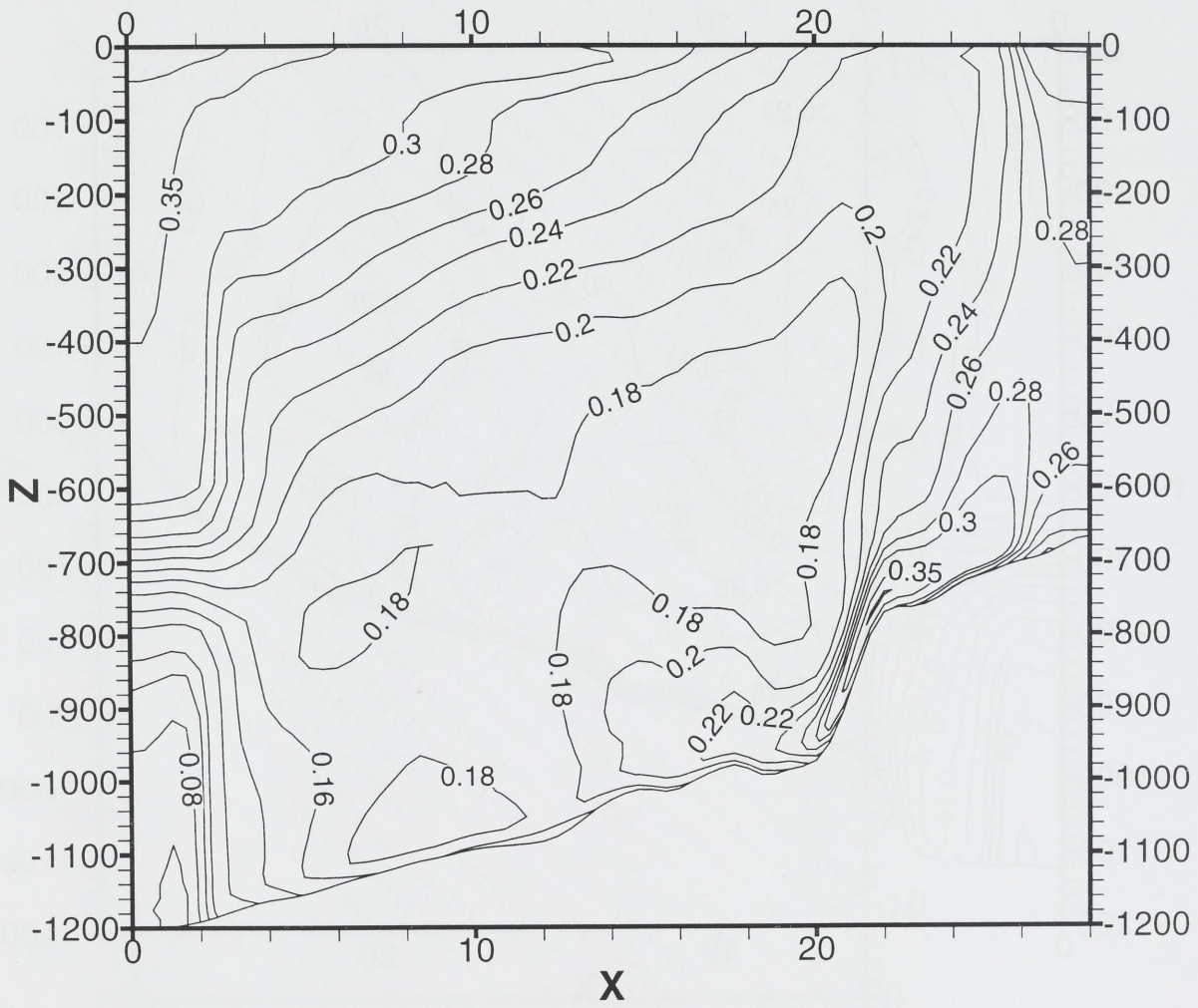

Figure 40: Current speeds through section II.

5.5 Numerical experiment 5

In the fifth experiment the modification compared to the first and third experiments is that the velocities used as initial and boundary conditions are given by the 10 year maximum estimates in Figure 6. Because of the stronger forcing the viscosities had to be increased for stability reasons, see Table 2.

The average kinetic energies develop very much like the previous experiments and after 48 hours the solution is stationary. In figures 41 and 42 the currents at 100m depth are given. In figures 43 and 44 the currents 50m above the bottom are given. In figures 45 and 46 the currents 10m above the bottom are given. In figures 47 and 48 the current speeds along sections I and II are given.

The resulting flow structures are very similar to the previous experiments. The flow is topography following with intensifications along the steep slopes.

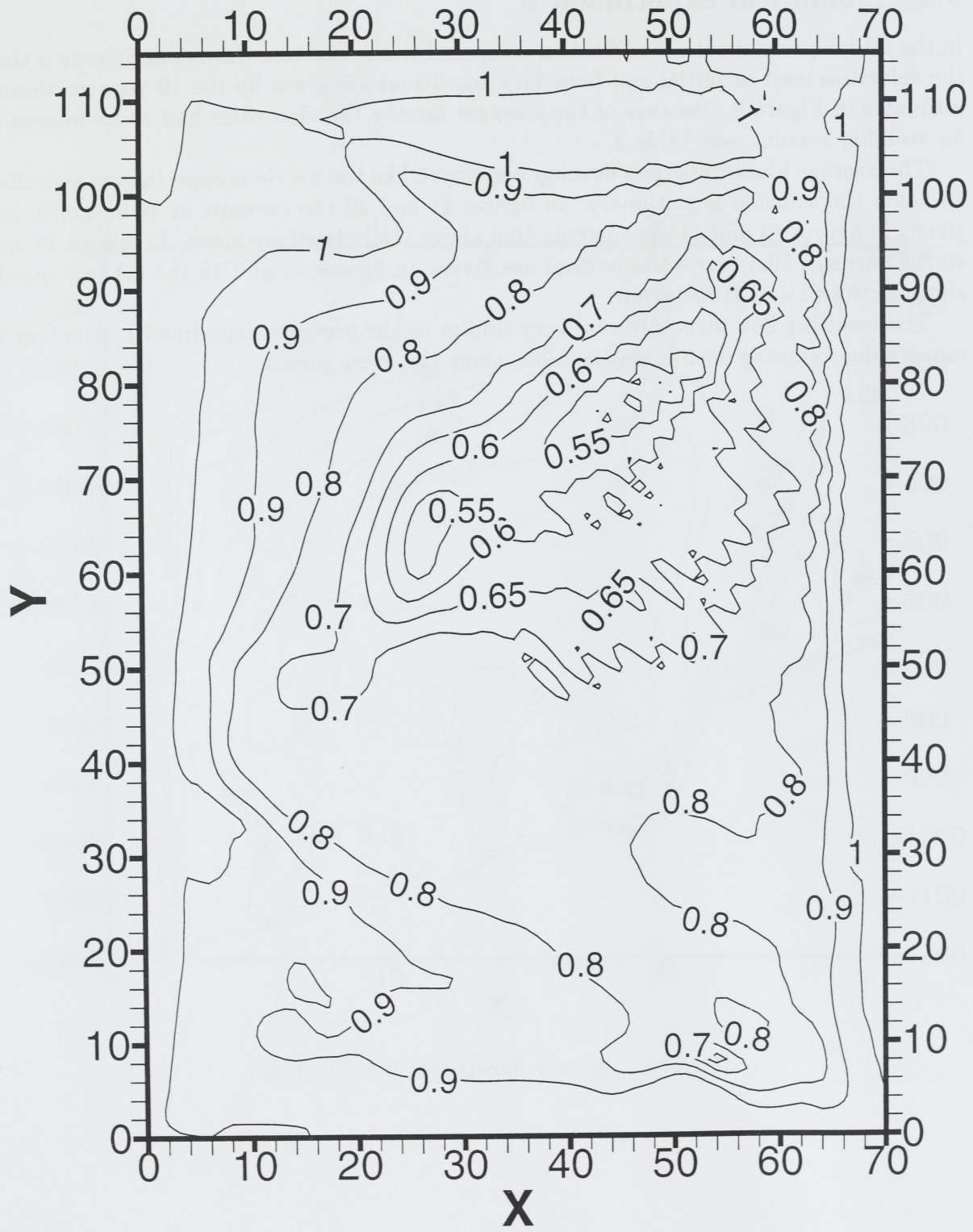

Figure 41: Current speeds at 100m depth after 48 hours.

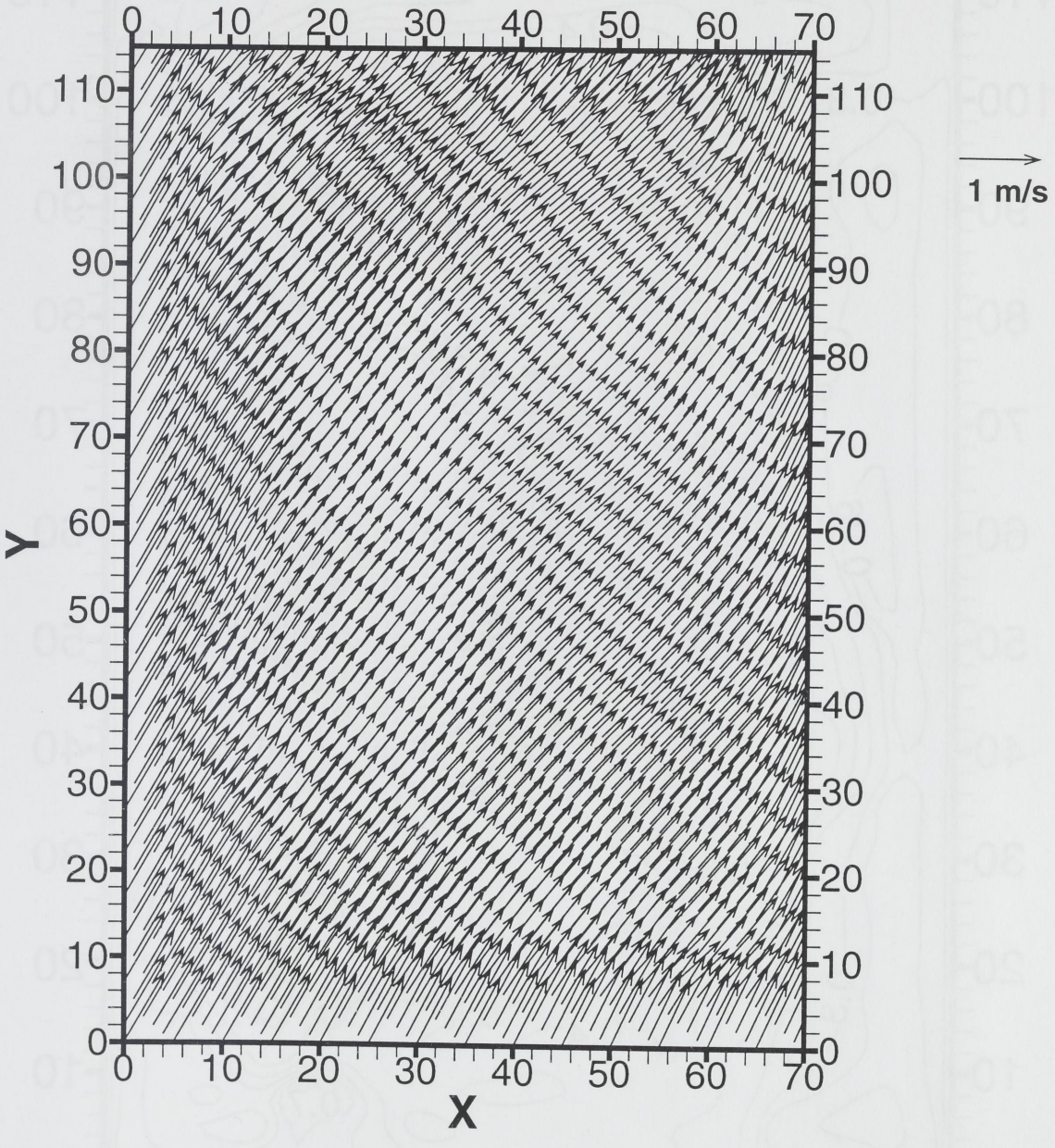

Figure 42: Vector plot of currents at 100m depth after 48 hours. Vectors are drawn from every 5th grid cell.

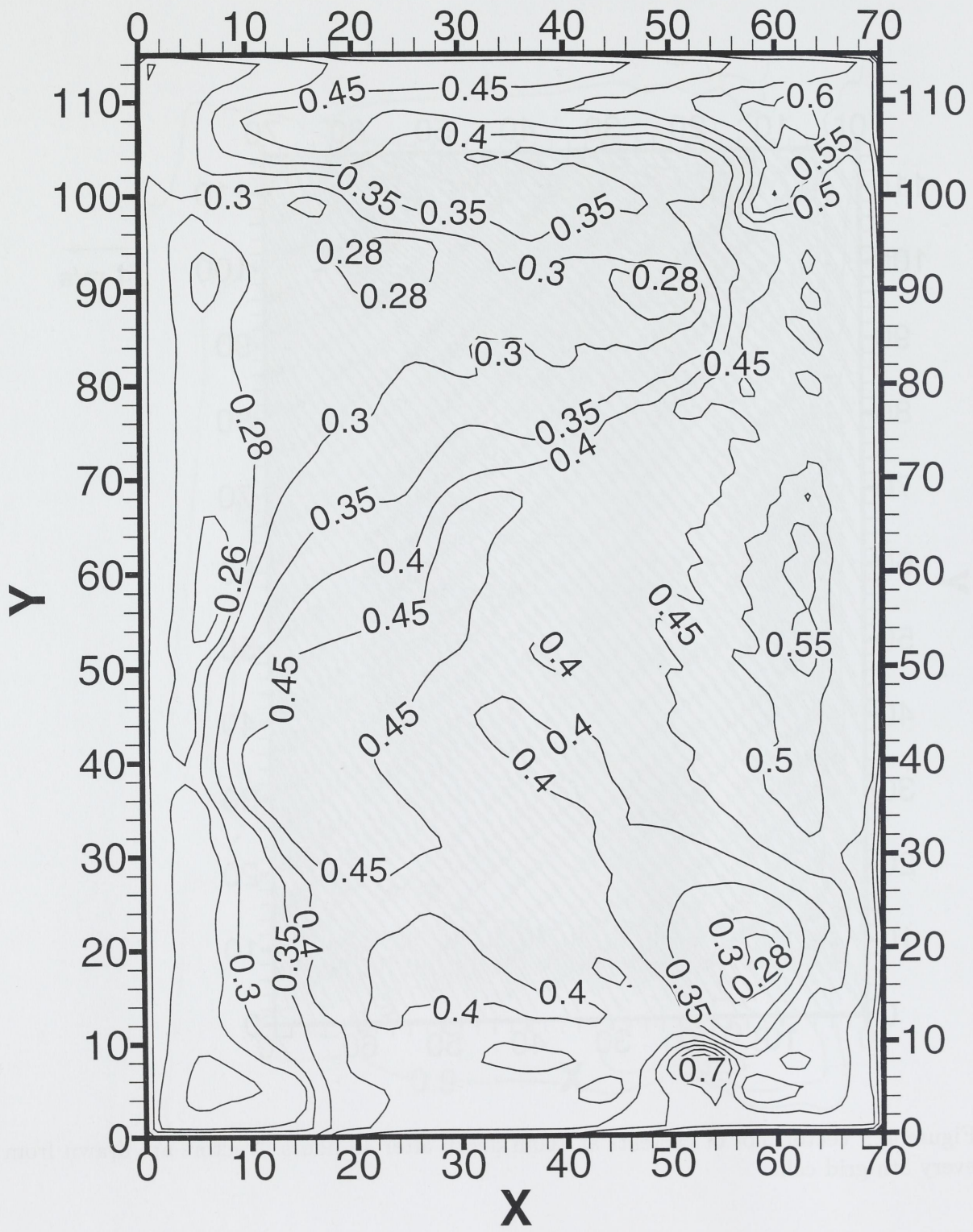

Figure 43: Current speeds 50m above the bottom after 48 hours.

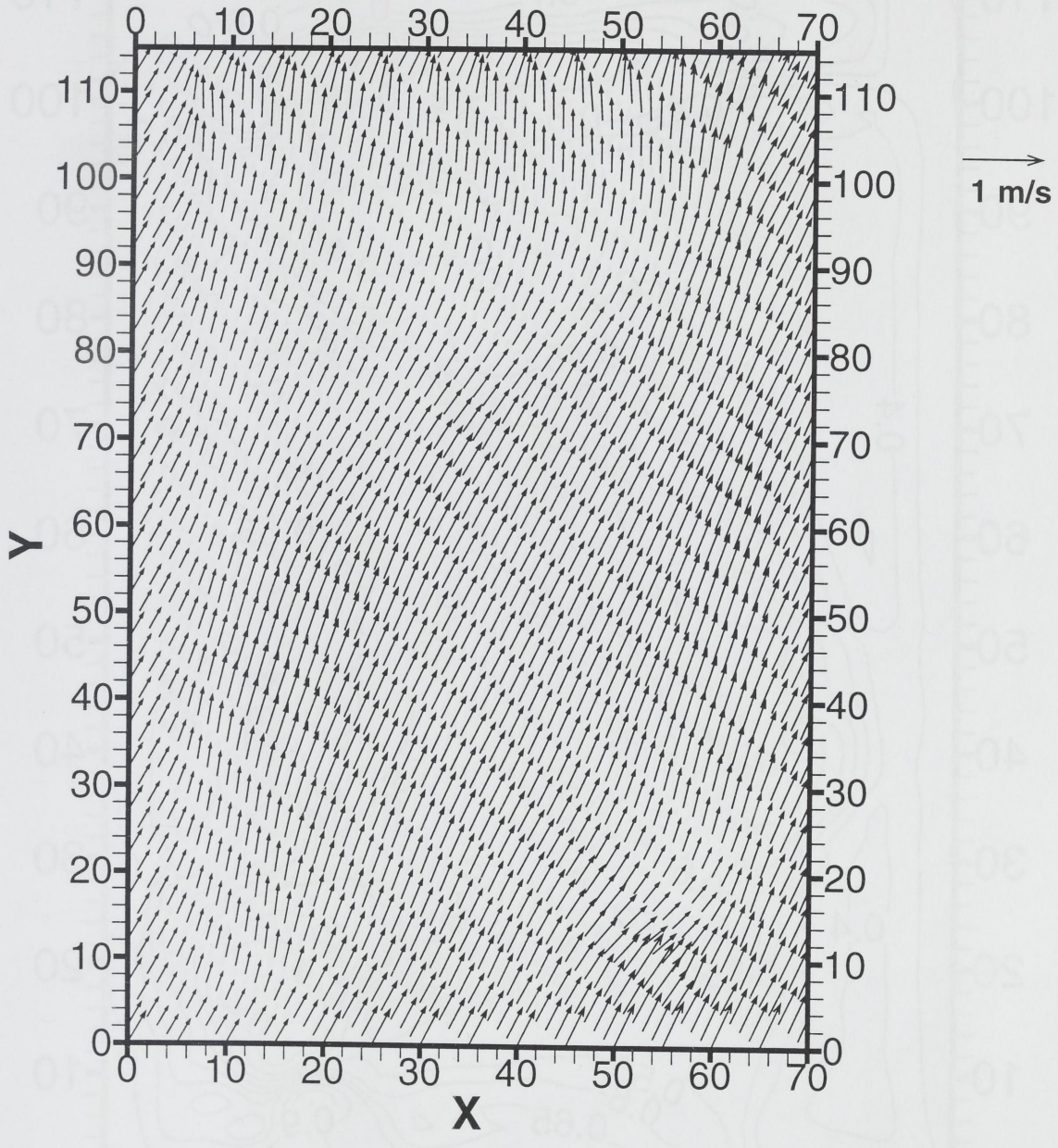

Figure 44: Vector plot of currents 50m above the bottom after 48 hours. Vectors are drawn from every 5th grid cell.

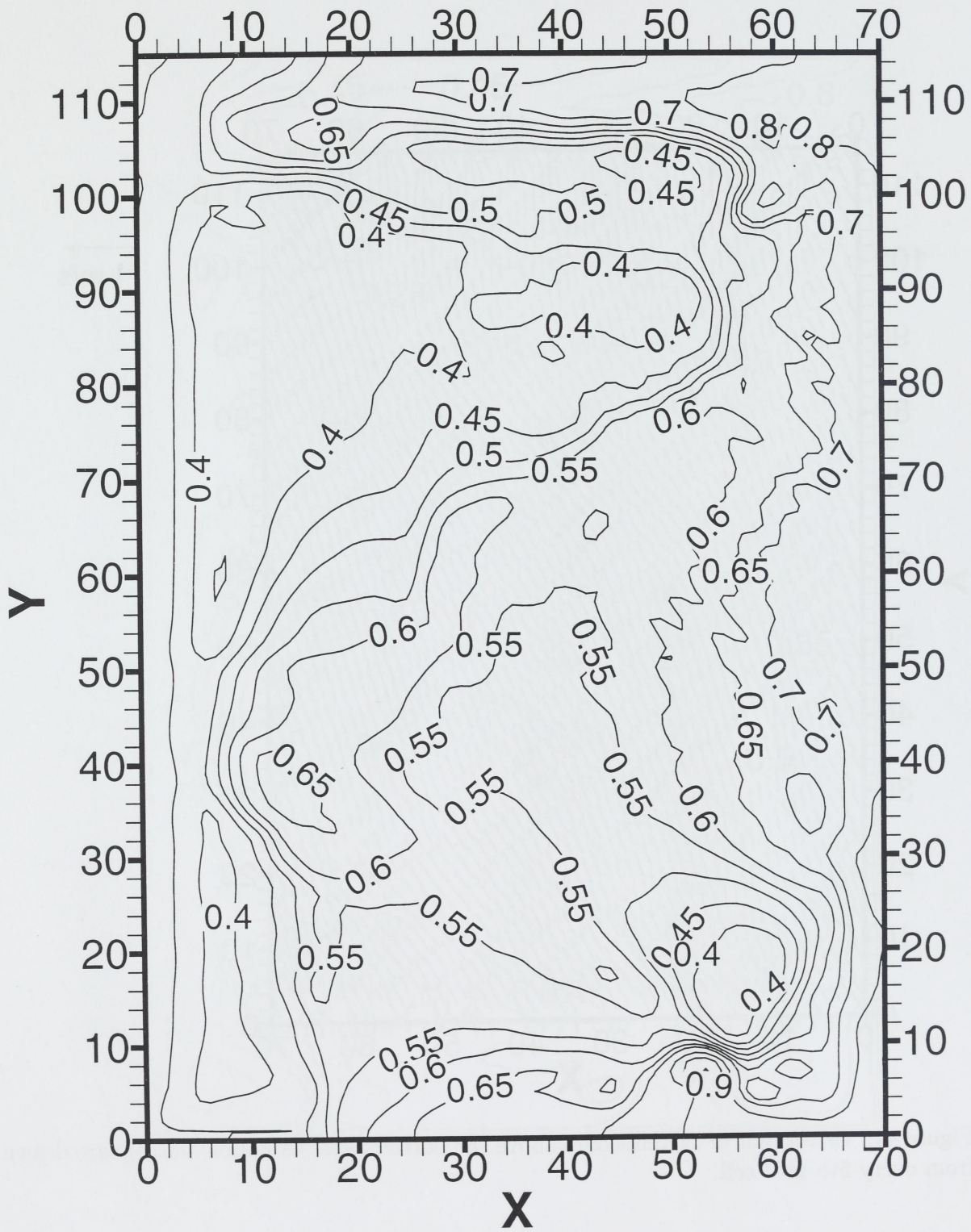

Figure 45: Current speeds 10m above the bottom after 48 hours.

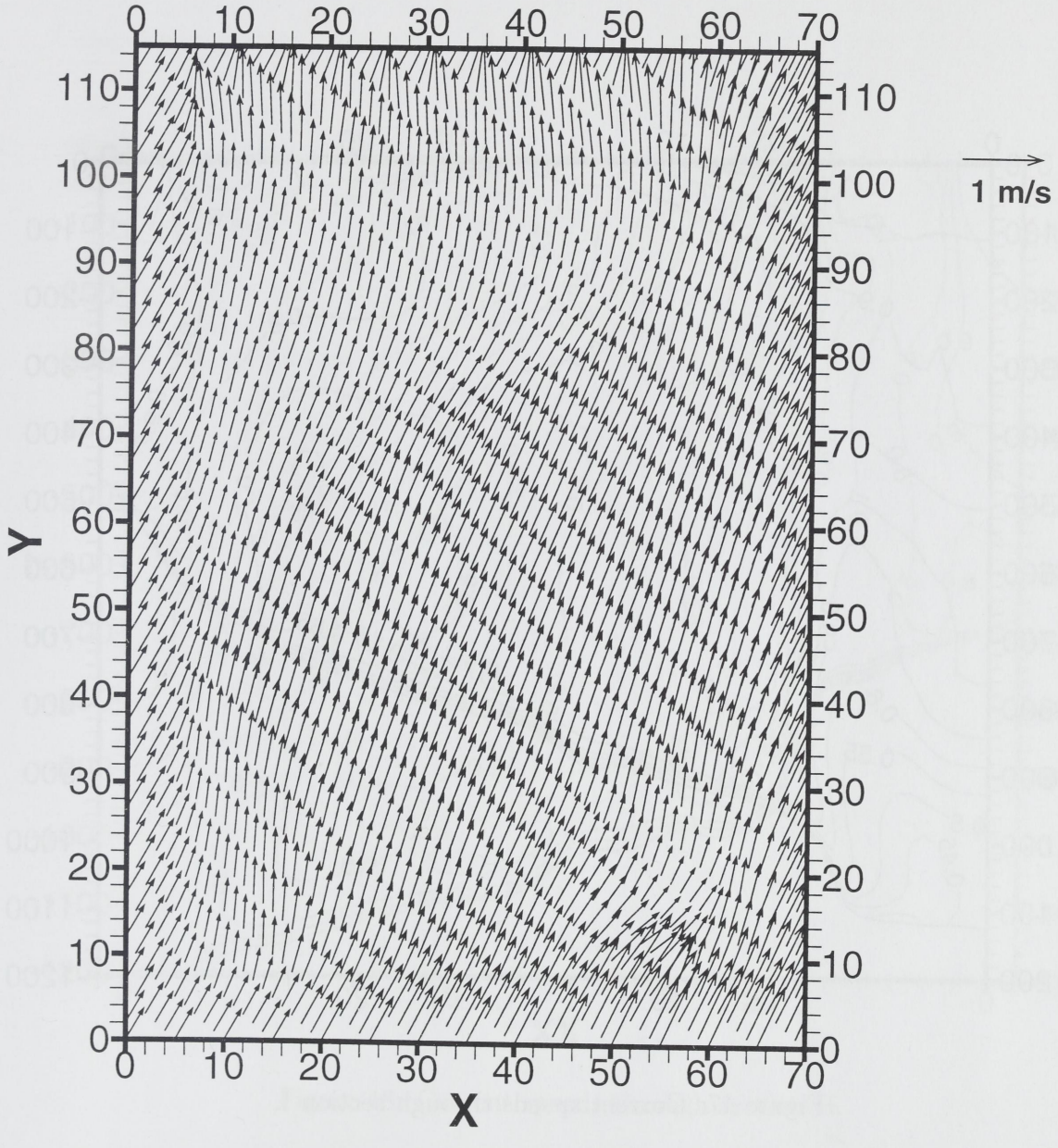

Figure 46: Vector plot of currents 10m above the bottom after 48 hours. Vectors are drawn from every 5th grid cell.

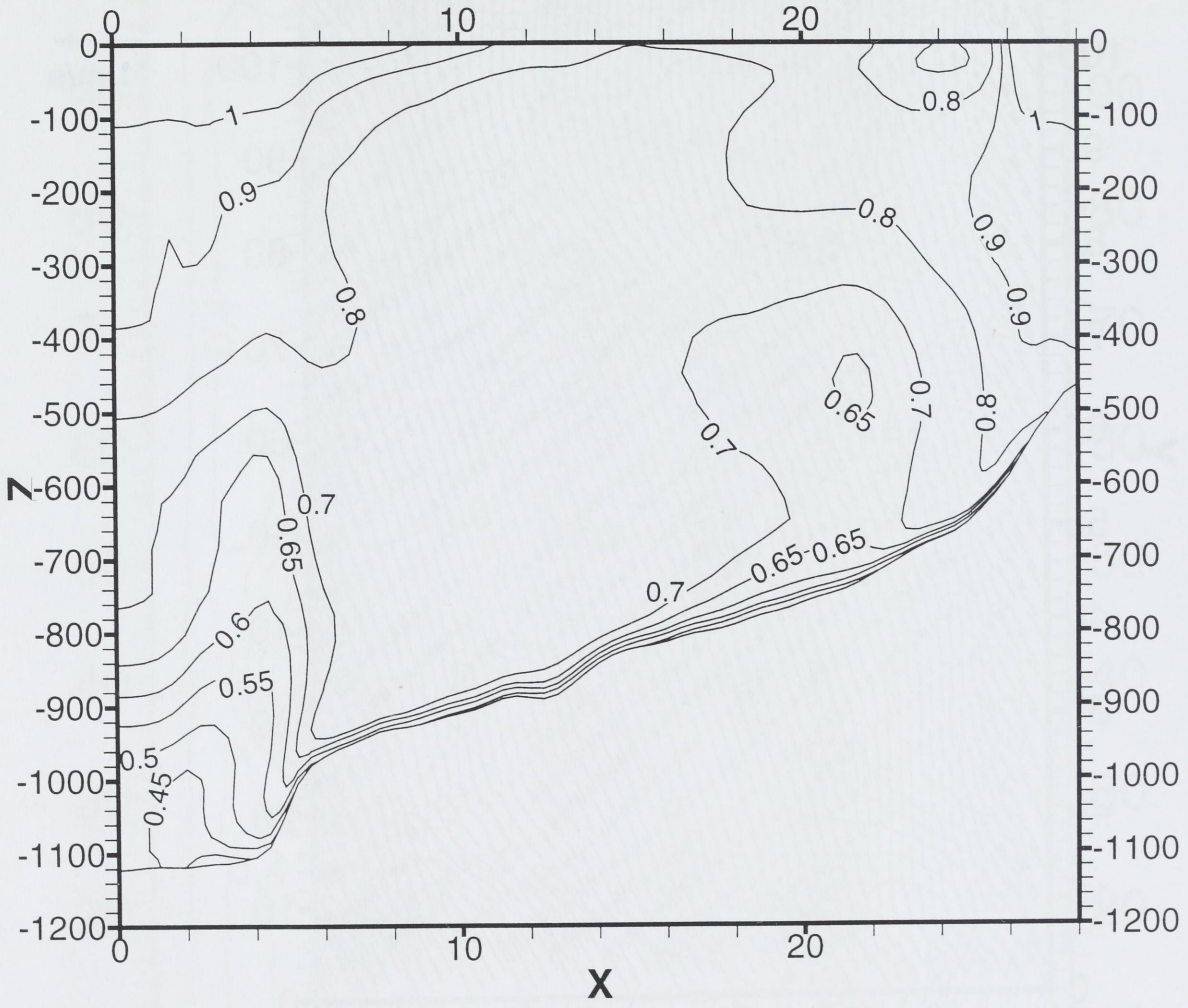

Figure 47: Current speeds through section I.

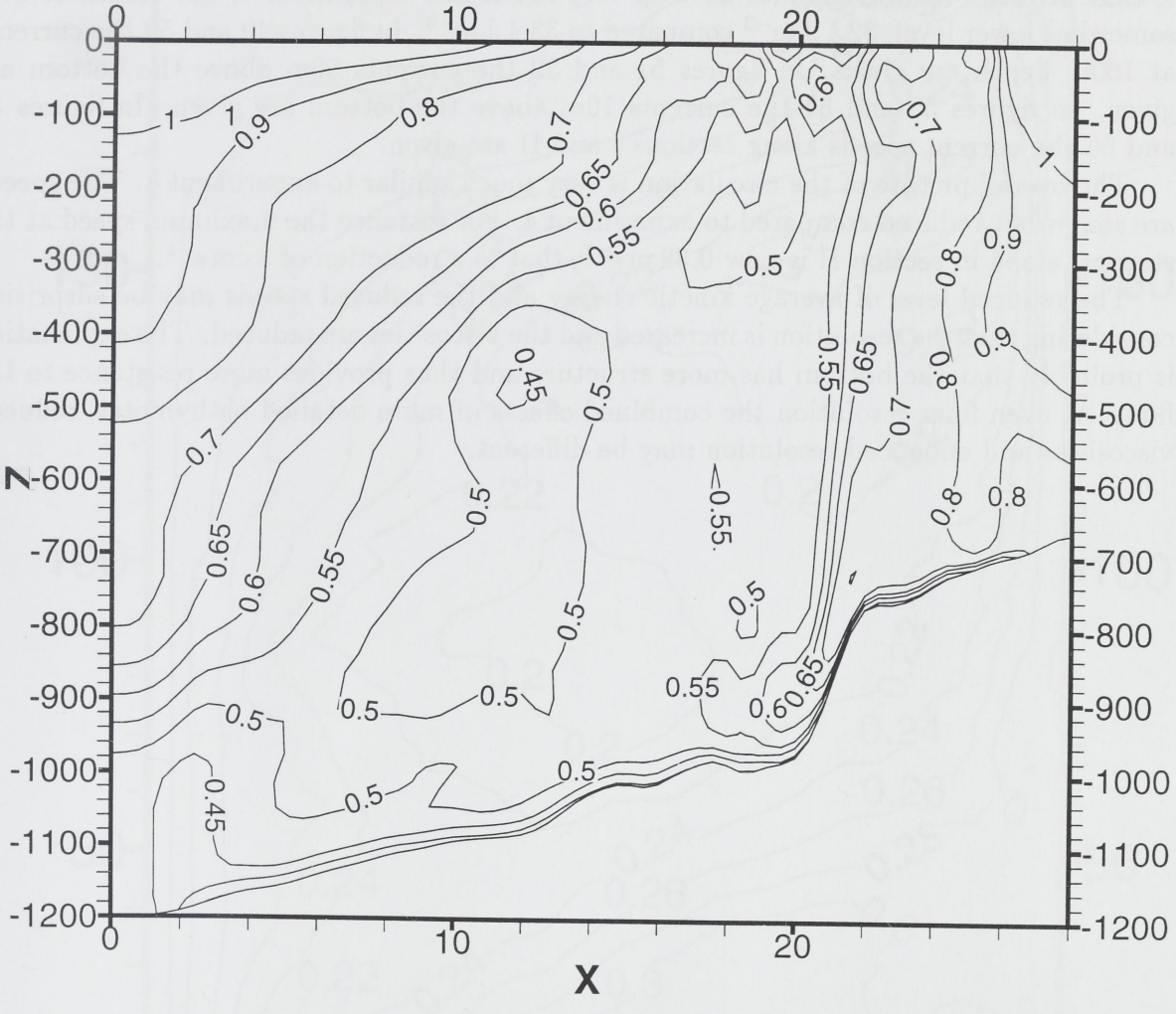

Figure 48: Current speeds through section II.

5.6 Numerical experiment 6

In the sixth experiment the major modification compared to the forth experiment is that the grid size is doubled to 140 × 230 giving a horizontal resolution of 200m. This also changes the bottom topography by allowing smaller structures. Furthermore, because smaller scale phenomena in the flow now are resolved the viscosities may be reduced, see Table 2.

The average kinetic energies develop very much like experiment 4, but stabilizes at a somewhat lower level, 32.1 J m^{-3} compared to 33.4 J m^{-3}. In figures 49 and 50 the currents at 100m depth are given. In figures 51 and 52 the currents 50m above the bottom are given. In figures 53 and 54 the currents 10m above the bottom are given. In figures 55 and 56 the current speeds along sections I and II are given.

The overall picture of the circulation is very much similar to experiment 4. The speeds are somewhat reduced compared to experiment 4. For instance the maximum speed at the steepest slope in section II is now 0.39 m s^{-1}, that is a reduction of 1 cm s^{-1}.

The reduced level of average kinetic energy and the reduced speeds may be surprising considering that the resolution is increased and the viscosities are reduced. The explanation is probably that the bottom has more structure and thus provides more resistance to the flow. At even finer resolution the combined effects of more detailed bathymetry, reduced viscosities and enhanced resolution may be different.

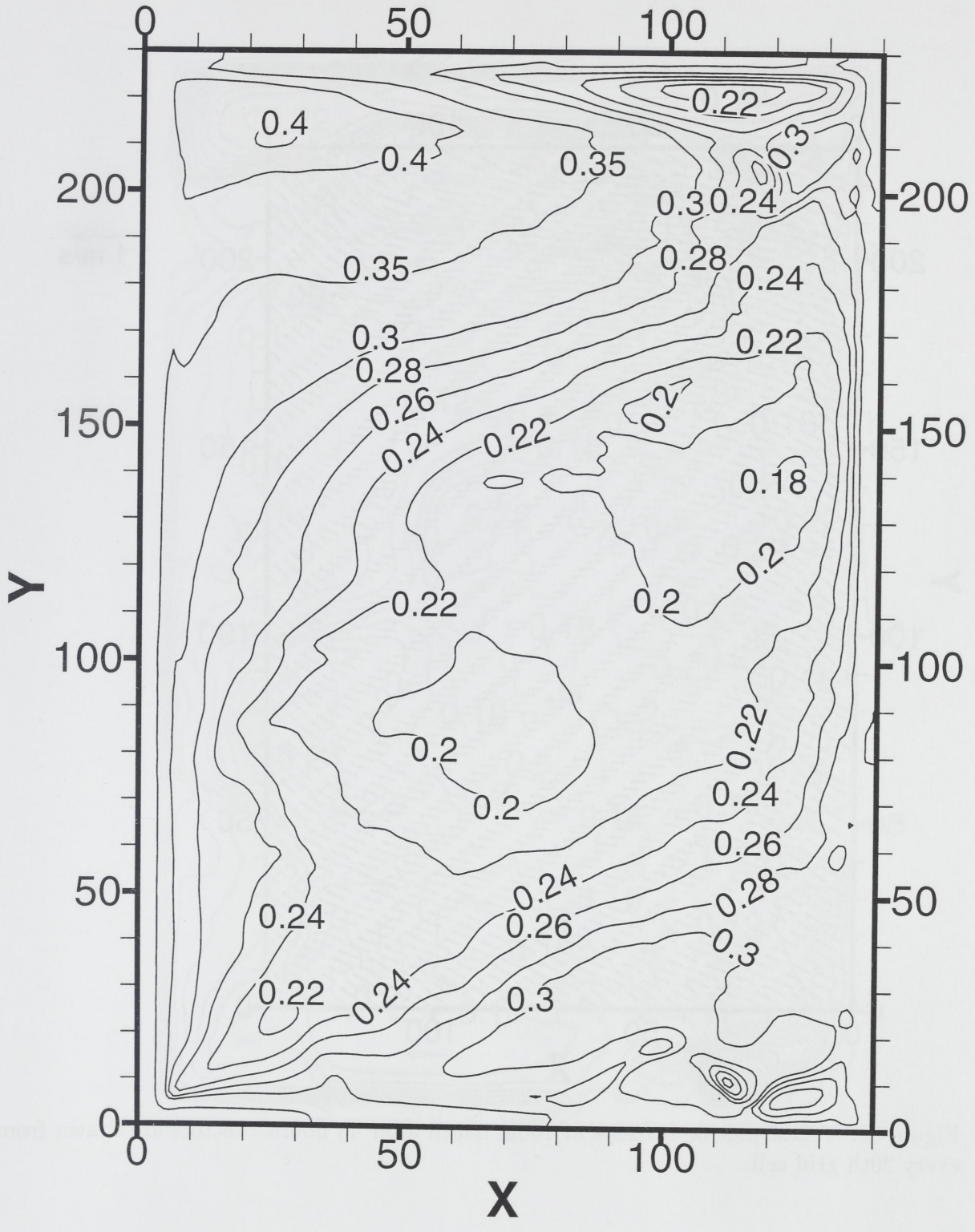

Figure 49: Current speeds at 100m depth after 48 hours.

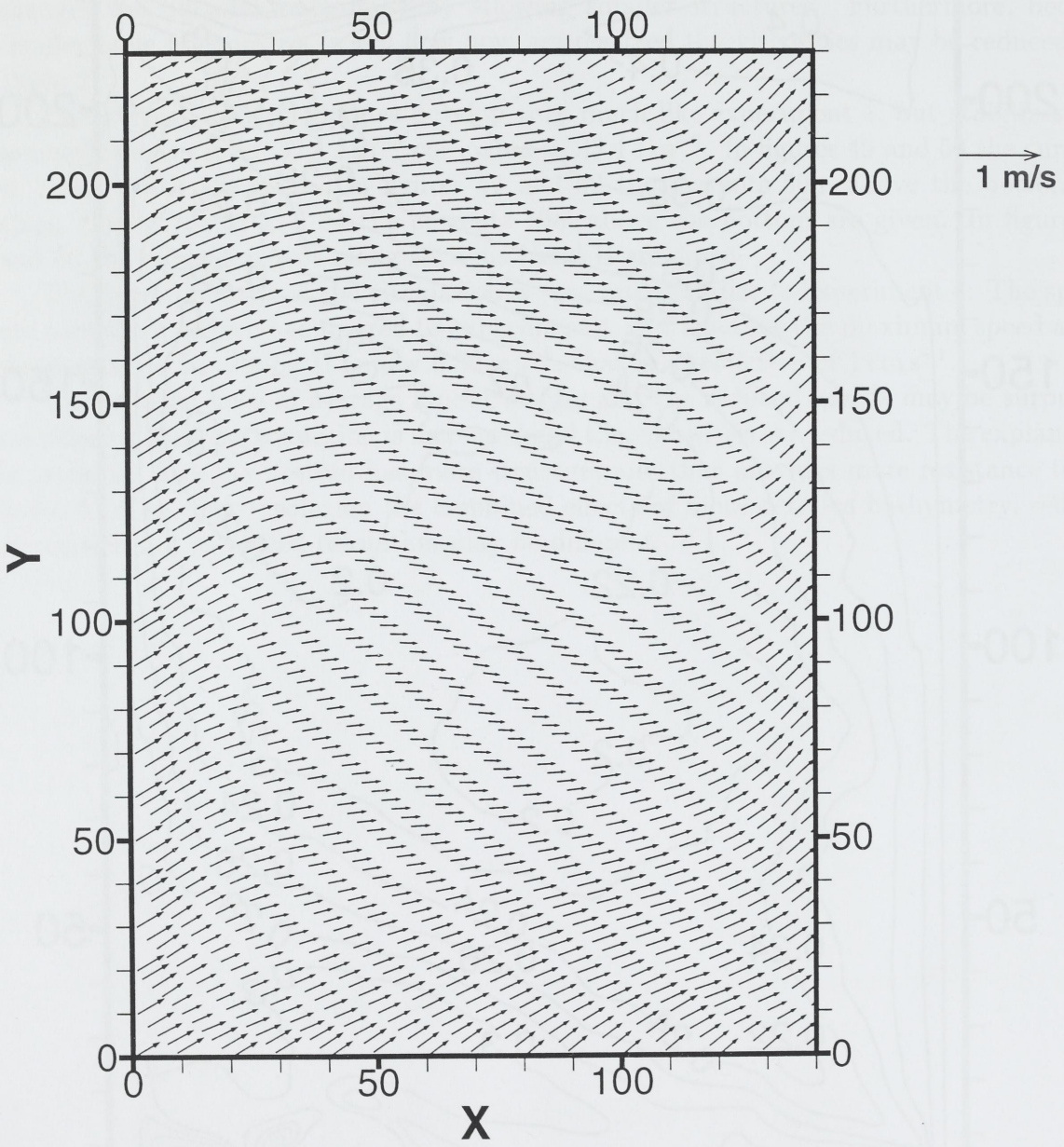

Figure 50: Vector plot of currents at 100m depth after 48 hours. Vectors are drawn from every 20th grid cell.

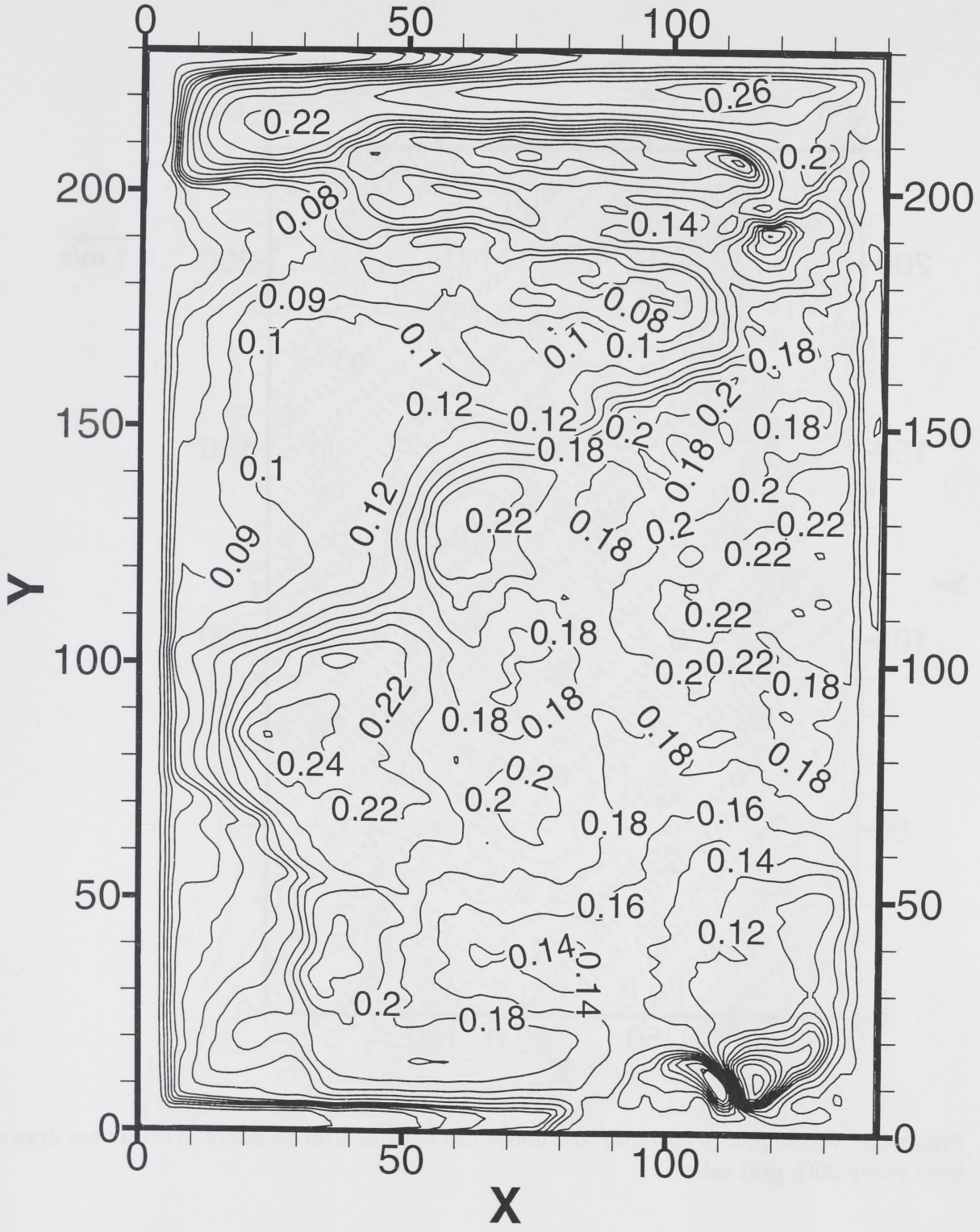

Figure 51: Current speeds 50m above the bottom after 48 hours.

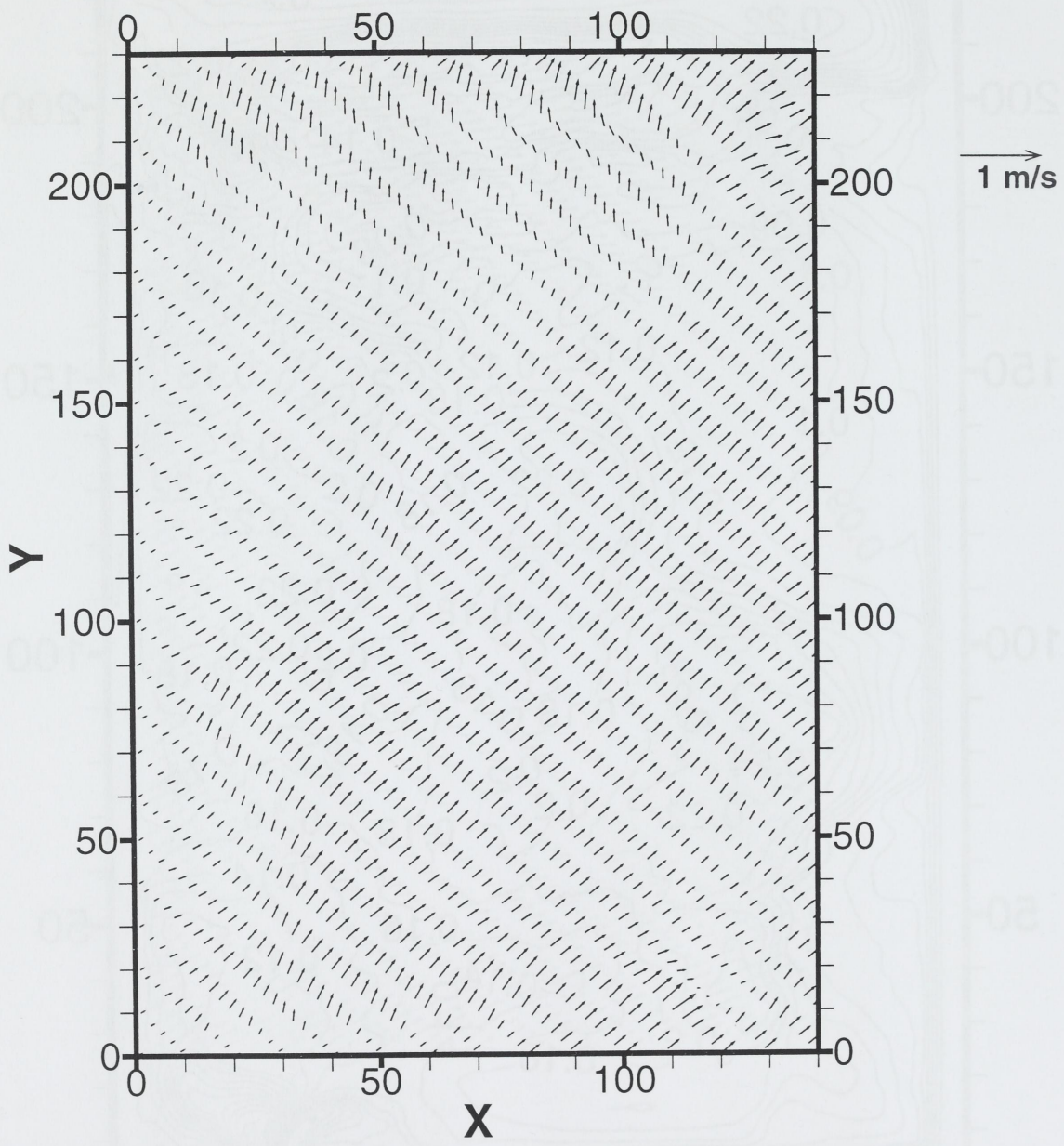

Figure 52: Vector plot of currents 50m above the bottom after 48 hours. Vectors are drawn from every 20th grid cell.

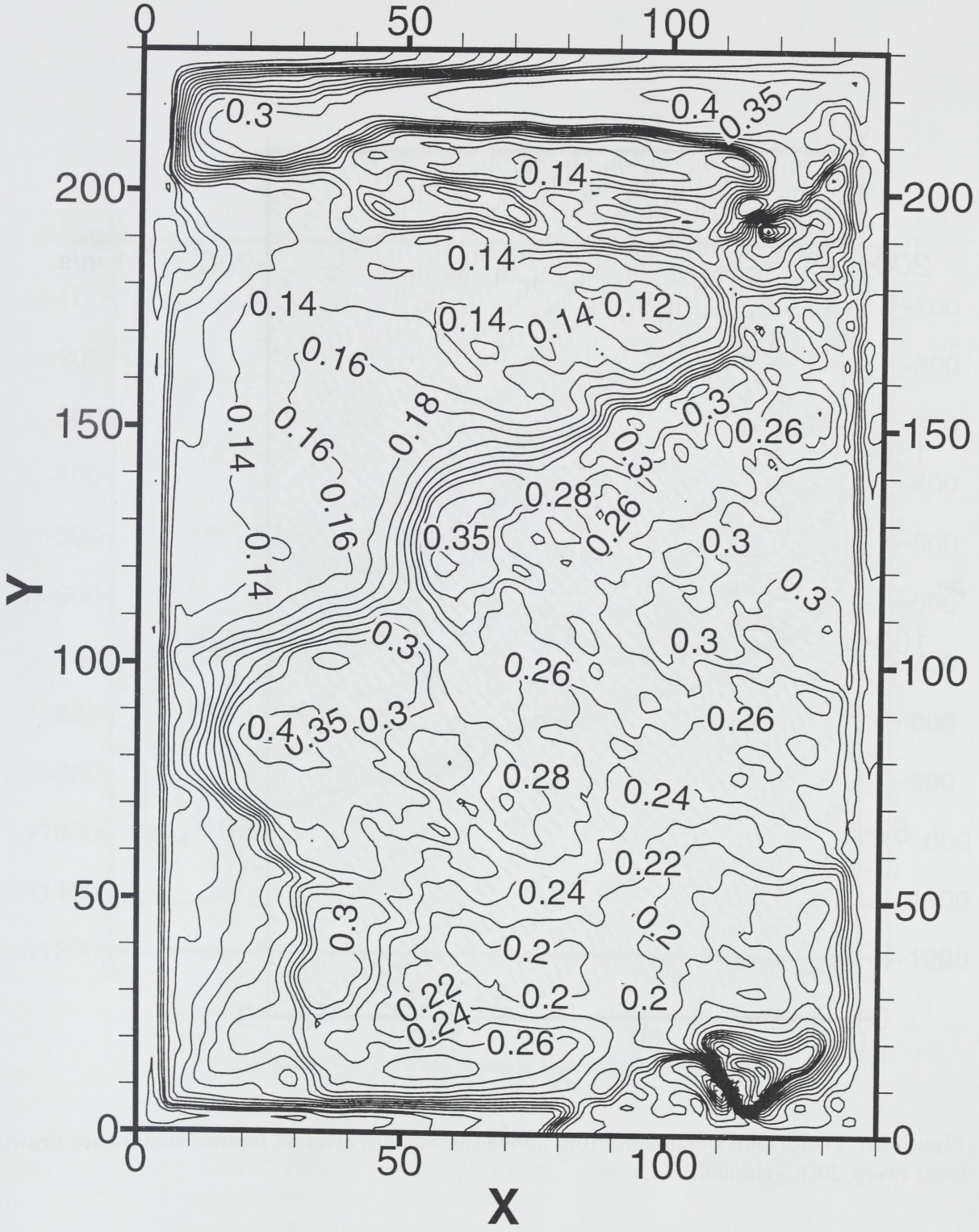

Figure 53: Current speeds 10m above the bottom after 48 hours.

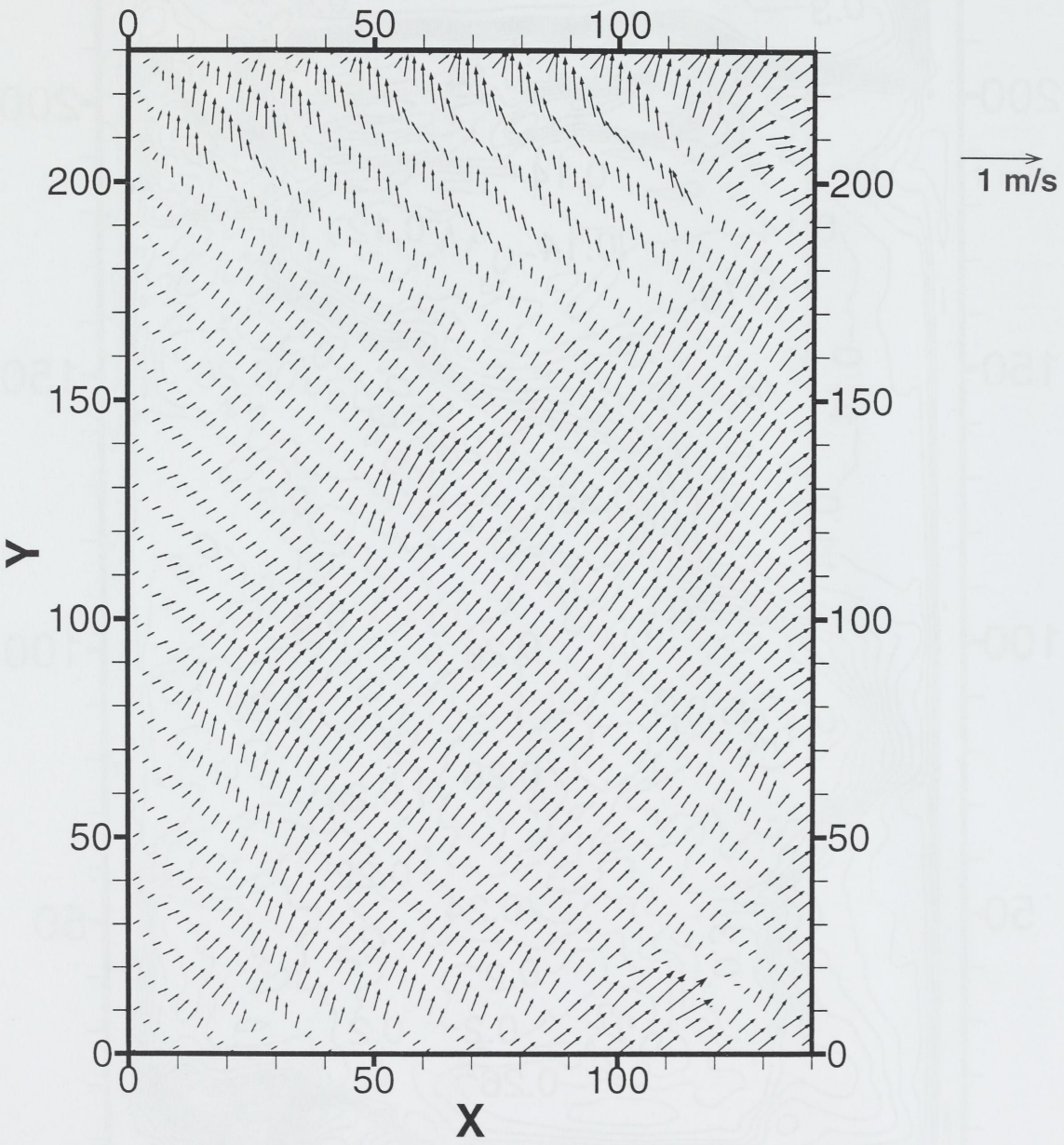

Figure 54: Vector plot of currents 10m above the bottom after 48 hours. Vectors are drawn from every 20th grid cell.

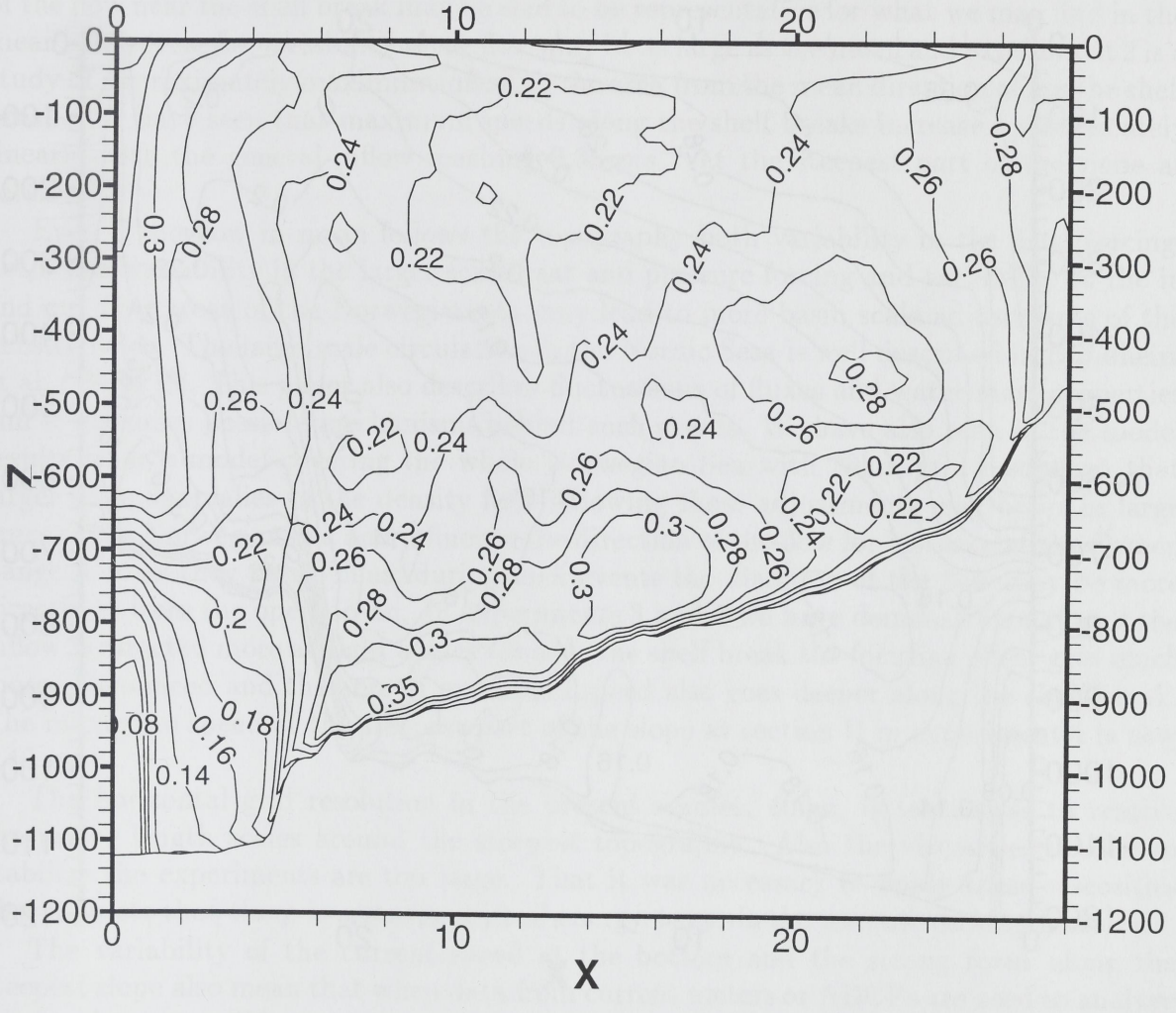

Figure 55: Current speeds through section I.

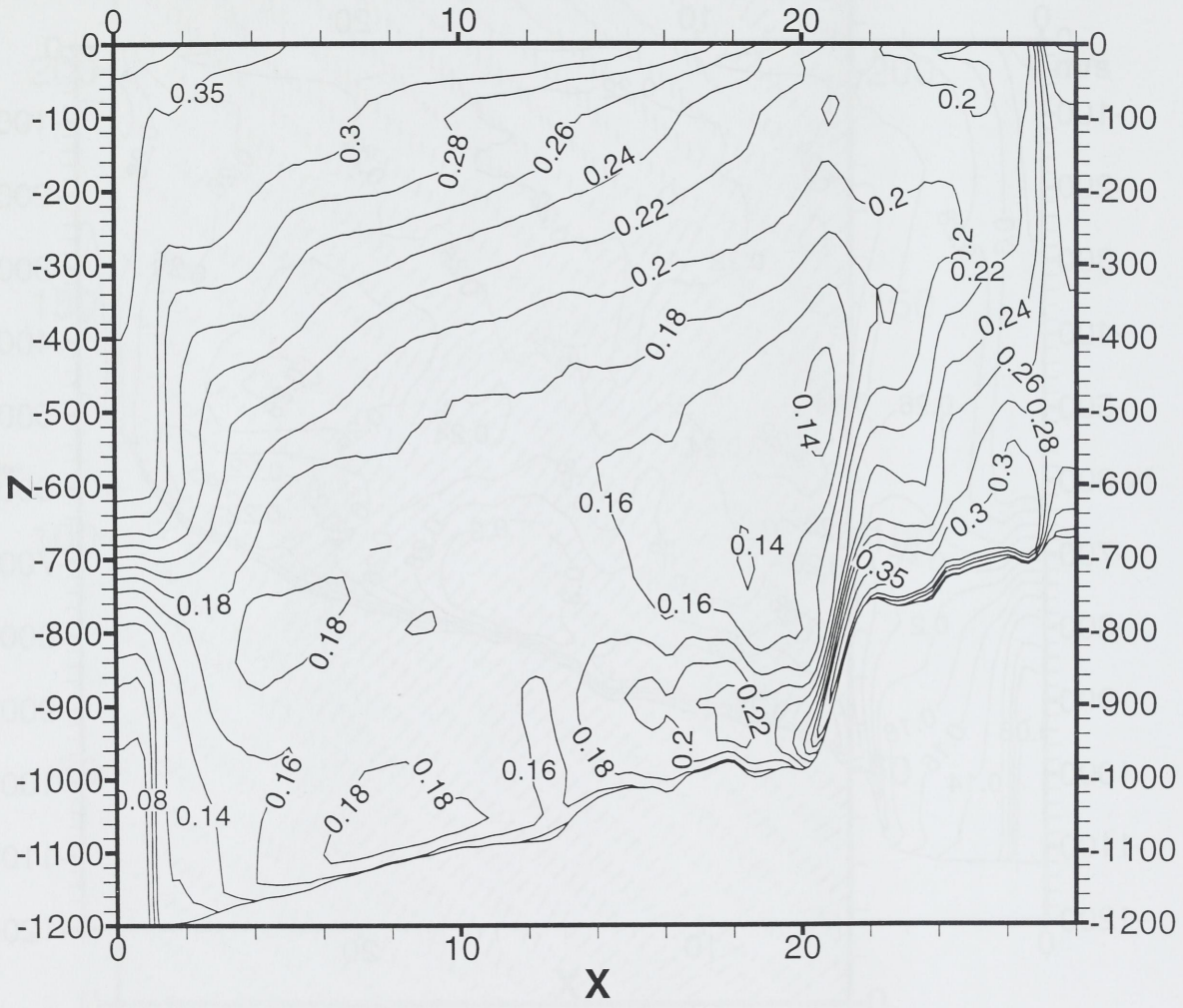

Figure 56: Current speeds through section II.

6 Discussion

The numerical studies presented here may be regarded as an attempt to study how the flow specified at open boundaries surrounding the Ormen Lange area may be interpolated into the interior of the domain taking into account the conservation laws that we believe determine the flow and the local topography.

In experiment 1 the forcing field is based on a climatological mean flow and the focusing of the flow near the shelf break may be said to be representative for what we may find in the mean. However, the variability of the flow may be as large as the mean and experiment 2 is a study of approximately maximum inflow to the area from the mean direction along the shelf break. We have seen that maximum speeds along the shelf breaks increase approximately linearly with the general inflow reaching 0.35 ms^{-1} at the steepest part of the slope at section II.

Even if the flow in mean follows the topography both variability in the local forcing, i.e., wind, variability in the larger scale heat and pressure forcing and variability in the in and out flow areas of the Norwegian sea may lead to more basin scale adjustments of the density fields. The large scale circulation in the Nordic Seas is well described in Blindheim et al. (1999) [8]. This paper also describes fluctuations of fluxes and water mass properties and it discusses possible mechanisms behind such events. We have also seen in the model results from a model covering the whole Norwegian Sea with 20km grid resolution that larger scale anomalies in the density field following these adjustments may occur in large areas of the Norwegian Sea and influence the direction of the flow for instance at the Ormen Lange field as they pass. Thus, during such events the direction of the flow may be more directly in from the open ocean. In experiments 3 and 4 we have demonstrated that if the inflow is directed more at right angles towards the shelf break the focusing effect gets much more pronounced and the area of maximum speed also goes deeper along the shelf break. The maximum speed at the steepest part of the slope at section II in experiment 4 is now 0.40 ms^{-1}.

The horizontal grid resolution in the present studies, 400m, is too coarse to resolve the major length scales around the steepest topography. Also the viscosities needed to stabilize the experiments are too large. That it was necessary to apply these viscosities also suggests that there is a strong drift of energy towards the unresolved length scales.

The variability of the current speed at the bottom and the strong focus along the steepest slope also mean that when data from current meters or ADCPs are used to analyze the maximum possible currents in the area their position relative to the topography is of major importance when the concern is flow near the bottom. In particular we notice that the currents meter rigs in Figure 2 are well below and well above the steepest part of the shelf break. Studying for instance Figure 32 giving speeds across the shelf break we notice that speeds close to the bottom at the shelf break may be twice as large as the speeds close to the bottom at the deepest current meter rig.

The effects of enhancing the resolution to 200m are seen in experiment 6. The energies and maximum speeds are somewhat reduced compared to experiment 4. The enhanced resolution allows a better representation of the flow along the steepest topography. This

alone would be suspected to increase the maximum speed. However, the inflowing water now feels the effects of a different bottom with more detailed structures. This may lead to a drainage of energy from the flow on its way eastwards to the shelf break. At even finer resolutions the combined effects of these mechanisms could be different so further investigations are needed.

7 Future work

In this study we have used a numerical model to simulate the circulation in a relatively small region in the Ormen Lange area. The results may be interpreted as interpolations of the specified flows at the open boundaries taking into account governing equations and topographical variations. In this way we can get a rough picture of the flow variability in the interior of the domain by varying the boundary conditions.

The flow field is seen to be heavily influenced of the local topography. The horizontally constant initial velocities were modified with respect to both magnitude and direction. Near the bottom a jet is following the shelf break with a speed considerably magnified relative to the initial state. With 200m horizontal resolution we still find maxima in the speed at the shelf break, but the extremal values here are slightly less than with 400m resolution. The necessity to use high viscosity parameters indicate that small scale phenomena on unresolved length scales are important. It would thus be desirable with further enhanced resolution.

Another important factor for the resulting flow field is the condition specified at the boundaries. A flow directed more perpendicularly to the shelf break produced a jet penetrating deeper with higher speed and increased shear. This gives an indication of the response of small scale structures to larger scale variability. It would thus be advisable to study circulation properties with more realistically varying boundary conditions.

7.1 Possible future projects on a short time scale

On a short time scale, months to a year, studies where output from the present model with 400 or 200m horizontal resolution is used as initial and boundary values for finer scale models focusing for instance on possible routes for pipelines may be performed. The finer scale models may have 25 or 50m horizontal resolution depending on the size of the area the model is supposed to cover. The nesting in such studies will be one way only. Effects of the finer scale topography on the flow may be studied by using this method.

7.2 Possible future projects on a longer time scale I

By applying the method used so far or the method suggested above, we do not get the effects of larger scale phenomena occurring in the Norwegian Sea basin properly into the model domain and the effects of smaller scale processes are not fed back to the larger scales. On a longer term basis, 1 to 3 years, we therefore suggest to build a two-way nested model system for the Norwegian Sea that allows coupling between a 20km model covering the whole basin and a sequence of finer models that focuses towards the Ormen Lange area. We suggest using a scaling factor of 5. With 6 levels of refinement the resolution at the finest level will be close to 1m. To establish such a model system will require a continued activity over years. Results will, however, be produced each time a new level is added to study the effects of the added refinement. With such a system one may study localized

effects of changes in the larger scale forcing variables like the major inflow/outflow to/from the Norwegian Sea, the atmospheric pressure, wind, heat fluxes etc.

7.3 Possible future projects on a longer time scale II

To learn about and to understand the currents in this area we have so far two sources of information: the direct observations and the model outputs. Both are valuable sources of information and in a recent paper Lynch and Hannah (1999) [18] describe an inverse model for estimating the currents using ADCP-data and/or current meter data. The model may said to be an interpolator for the measurements taken, and the qualities of the modeled currents depend heavily on the geographic placement of for instance the current meter rigs. Such an observation system, model and measurements, would be very useful to produce good estimates of currents inside the region covered by current meter rigs or ADCPs. To establish the model side of such a system would probably take 2 or 3 man years if guided by a person that is familiar with this technology.

A Figures for experiments 1–4

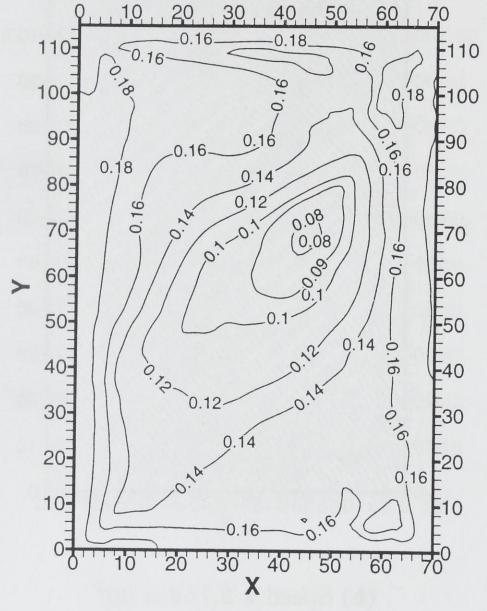

(a) Speed × 1, $\theta = 30°$

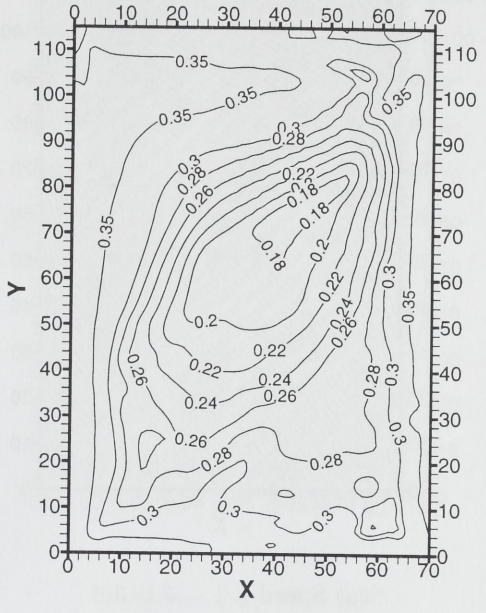

(b) Speed × 2, $\theta = 30°$

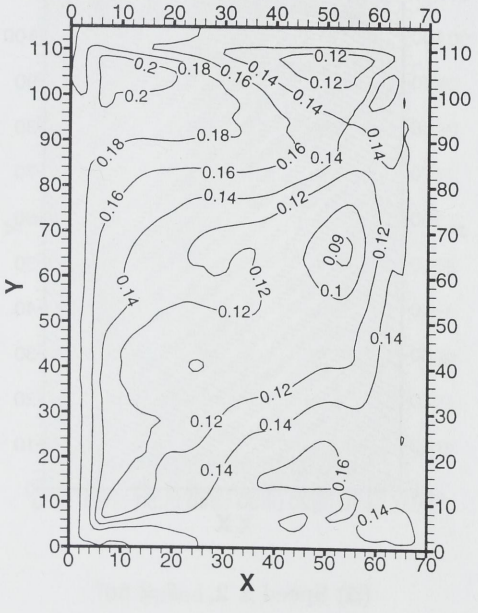

(c) Speed × 1, $\theta = 60°$

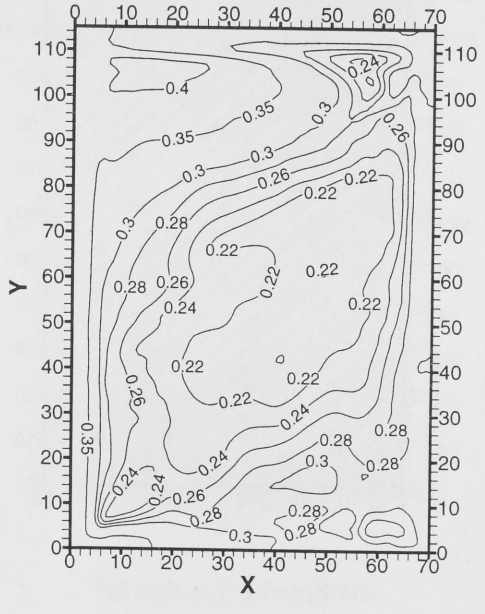

(d) Speed × 2, $\theta = 60°$

Figure 57: Speed at 100 m depth.

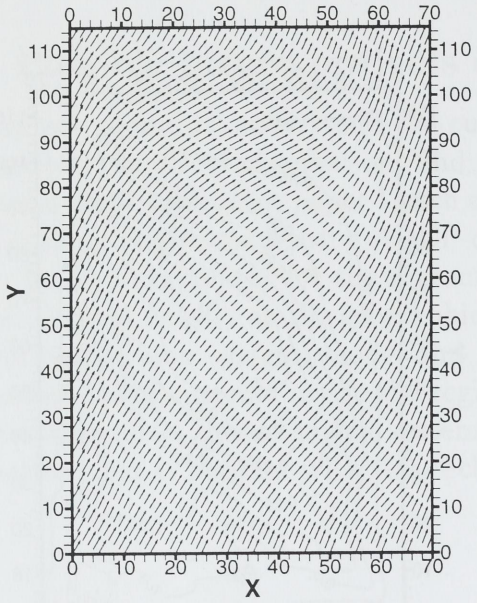

(a) Speed × 1, $\theta = 30°$

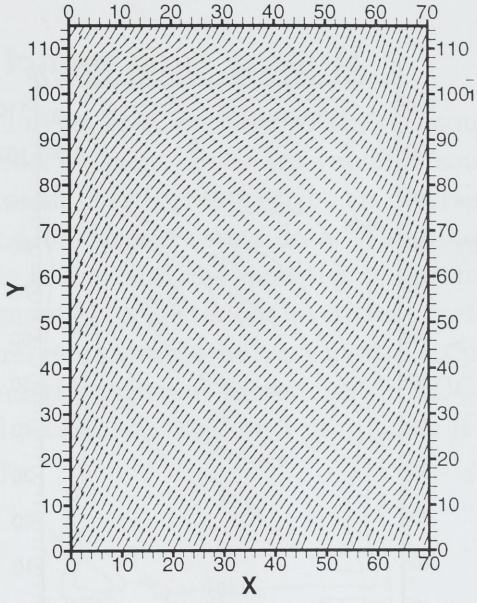

(b) Speed × 2, $\theta = 30°$

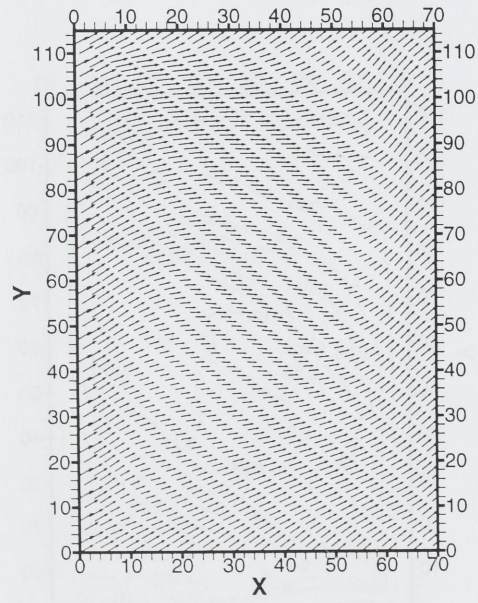

(c) Speed × 1, $\theta = 60°$

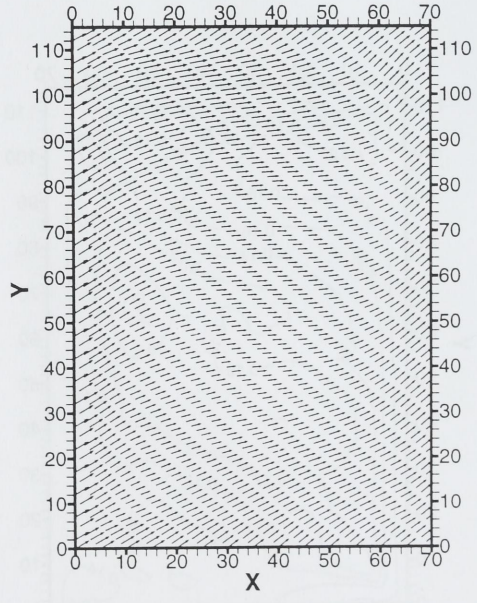

(d) Speed × 2, $\theta = 60°$

Figure 58: Velocity at 10 m depth. (Length of arrows not directly comparable.)

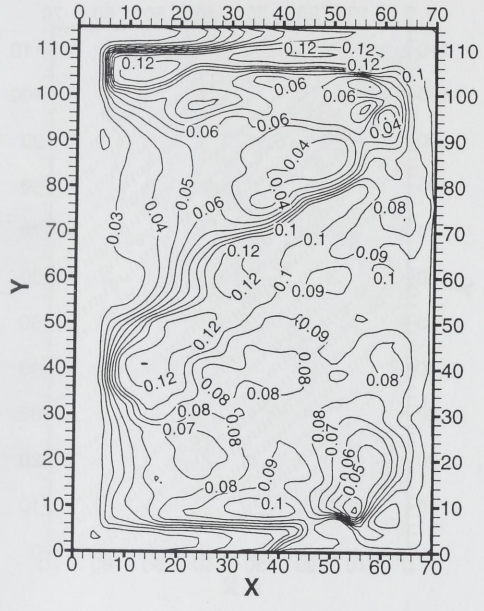

(a) Speed × 1, $\theta = 30°$

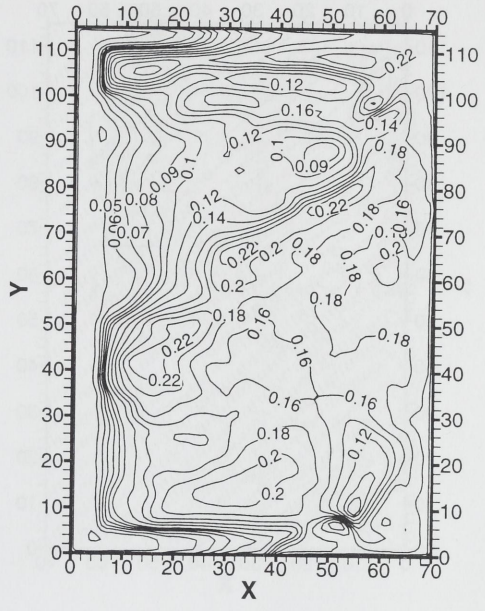

(b) Speed × 2, $\theta = 30°$

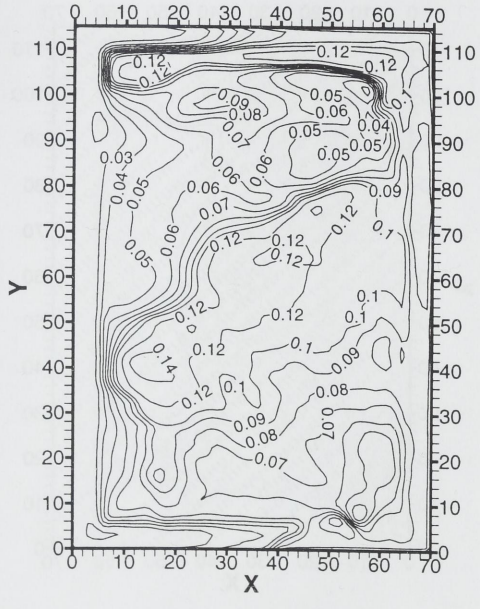

(c) Speed × 1, $\theta = 60°$

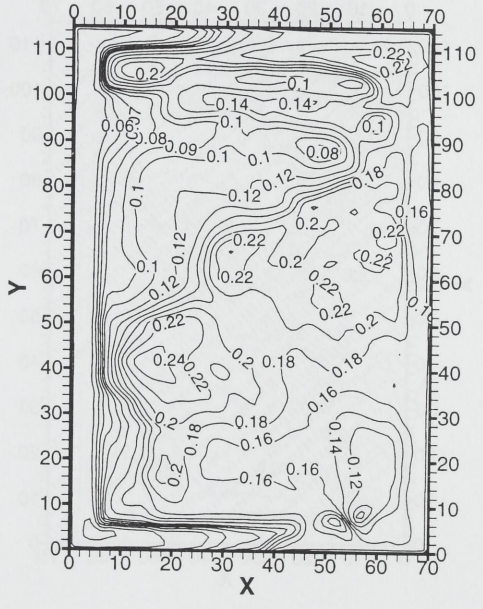

(d) Speed × 2, $\theta = 60°$

Figure 59: Speed at 50 m over bottom.

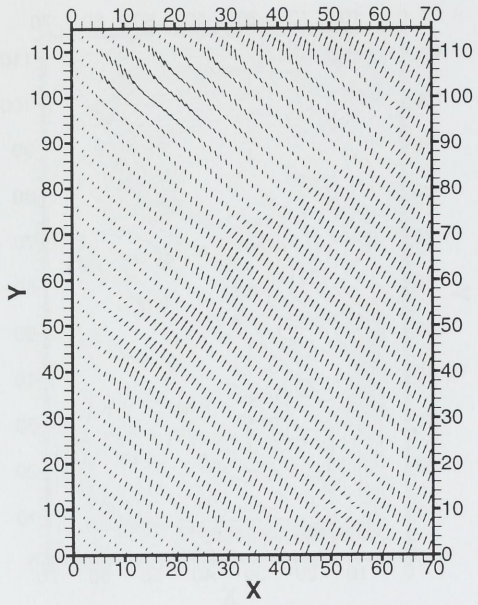

(a) Speed × 1, $\theta = 30°$

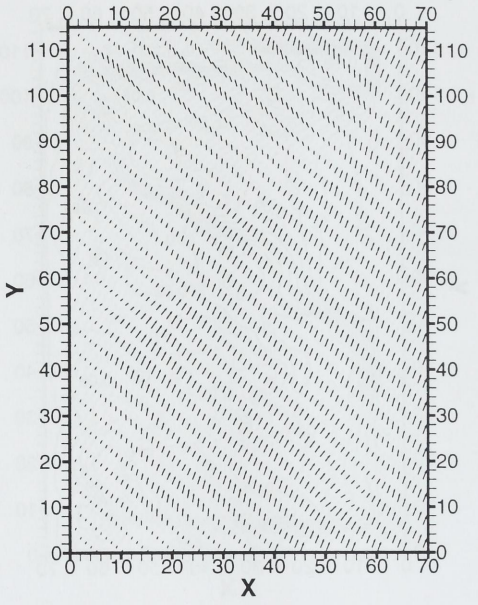

(b) Speed × 2, $\theta = 30°$

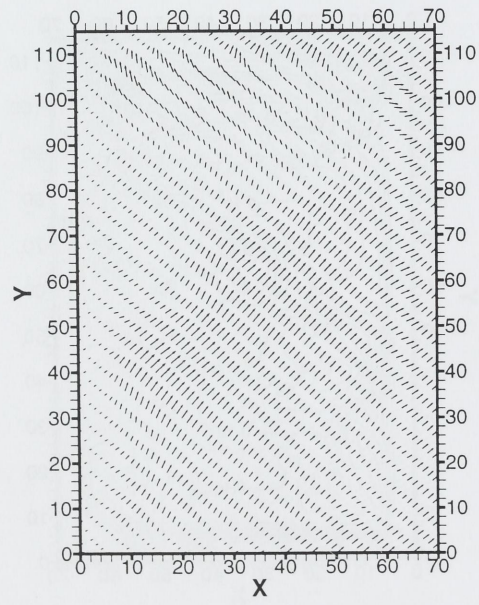

(c) Speed × 1, $\theta = 60°$

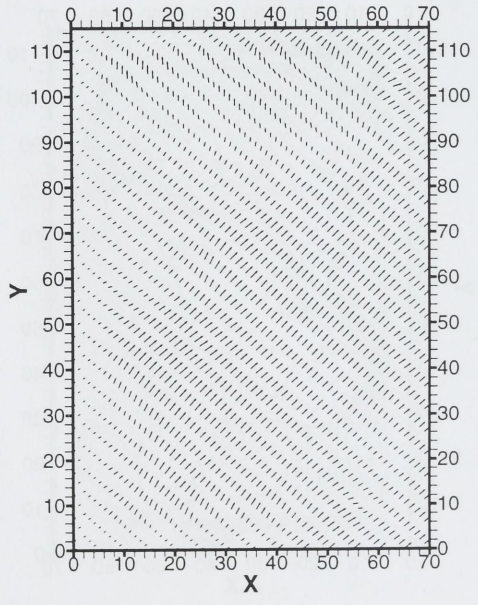

(d) Speed × 2, $\theta = 60°$

Figure 60: Velocity at 50 m over bottom. (Length of arrows not directly comparable.)

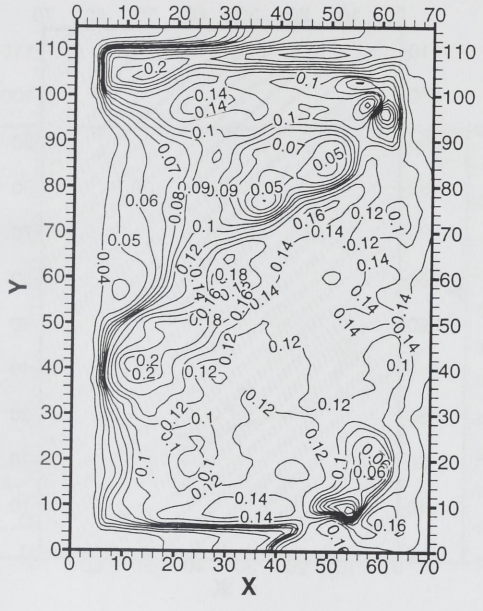

(a) Speed × 1, $\theta = 30°$

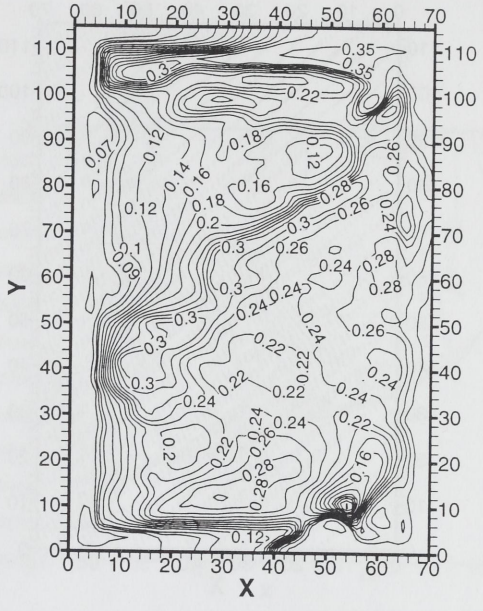

(b) Speed × 2, $\theta = 30°$

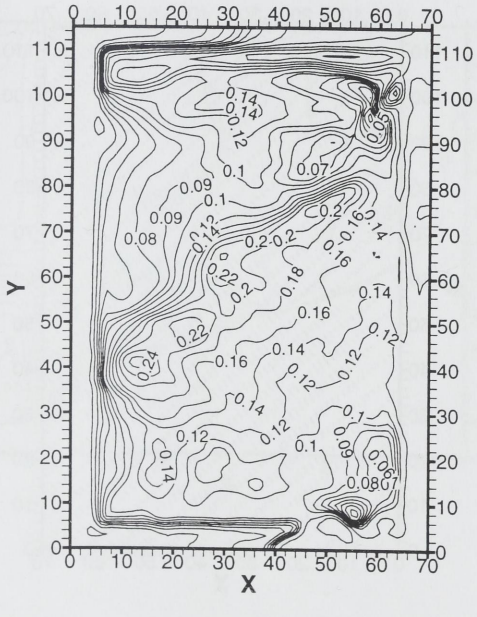

(c) Speed × 1, $\theta = 60°$

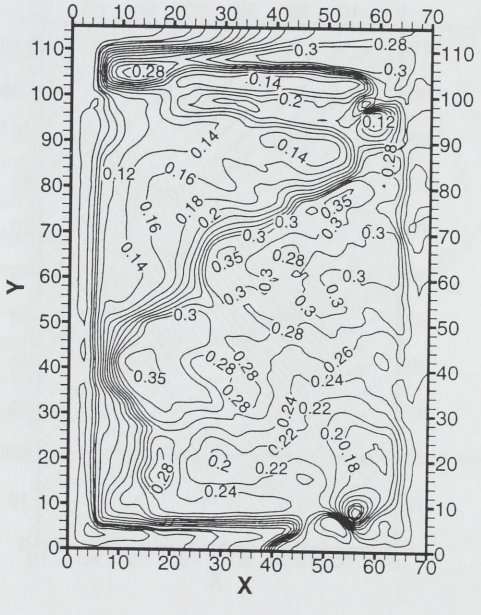

(d) Speed × 2, $\theta = 60°$

Figure 61: Speed at 10 m over bottom.

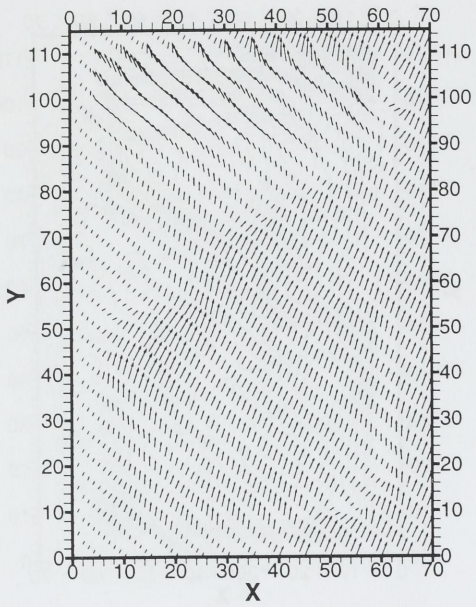

(a) Speed × 1, $\theta = 30°$

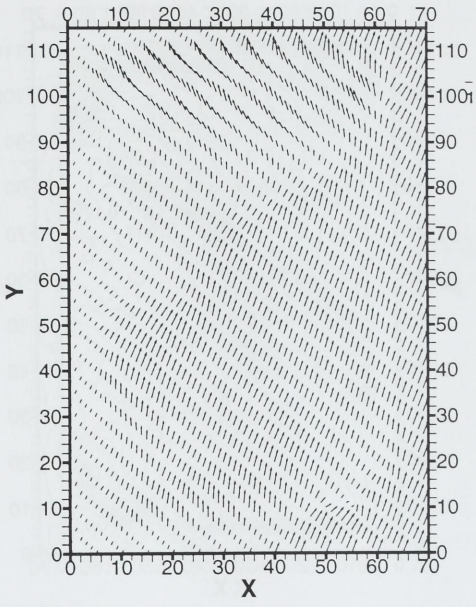

(b) Speed × 2, $\theta = 30°$

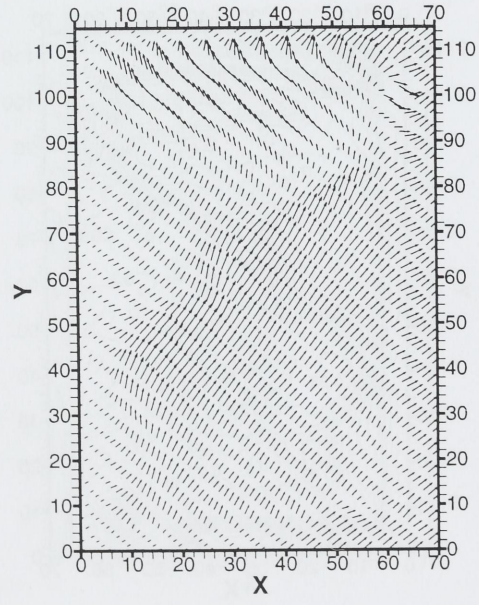

(c) Speed × 1, $\theta = 60°$

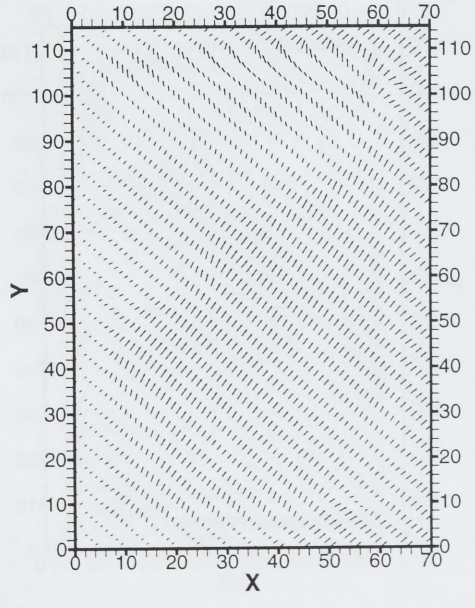

(d) Speed × 2, $\theta = 60°$

Figure 62: Velocity at 10 m over bottom. (Length of arrows not directly comparable.)

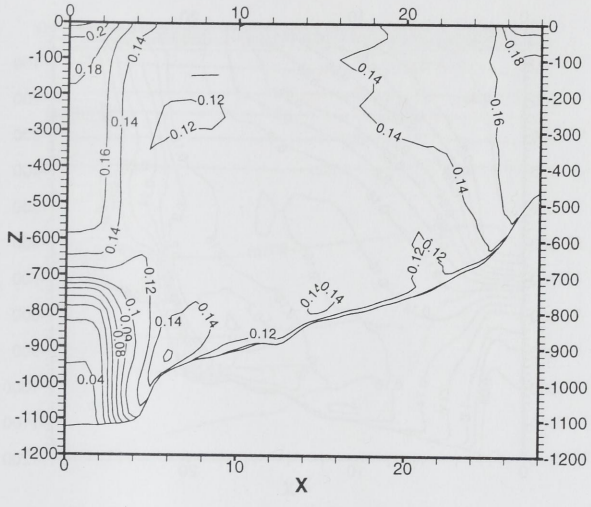

(a) Speed × 1, $\theta = 30°$

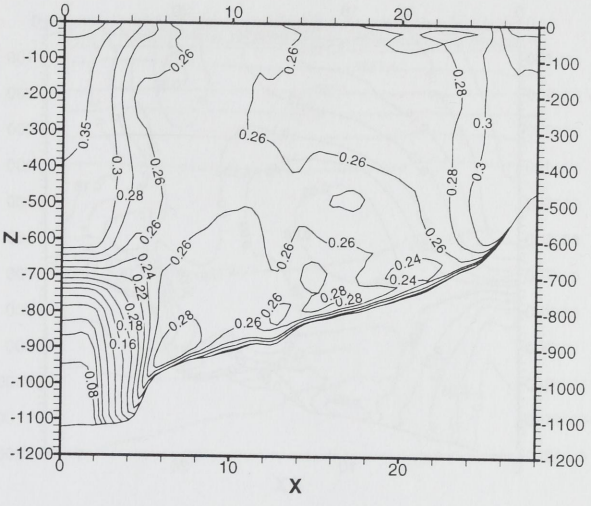

(b) Speed × 2, $\theta = 30°$

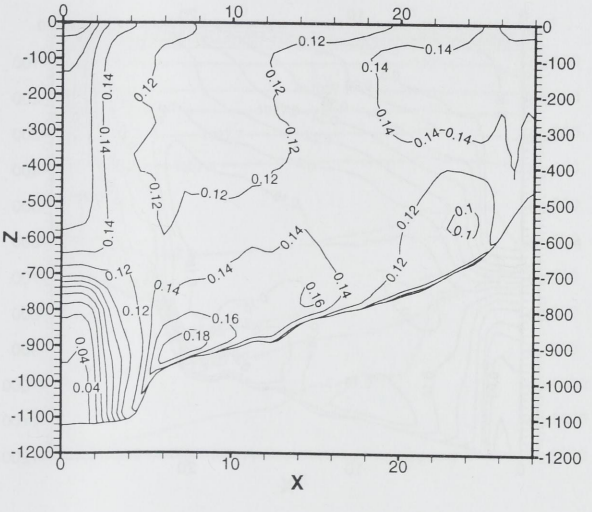

(c) Speed × 1, $\theta = 60°$

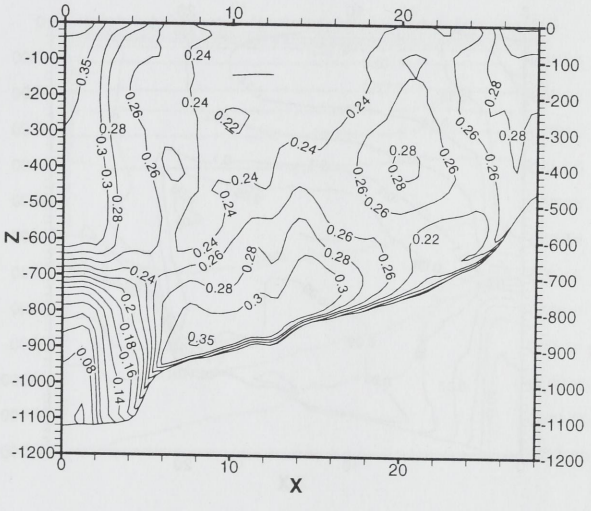

(d) Speed × 2, $\theta = 60°$

Figure 63: Current speeds at Section I.

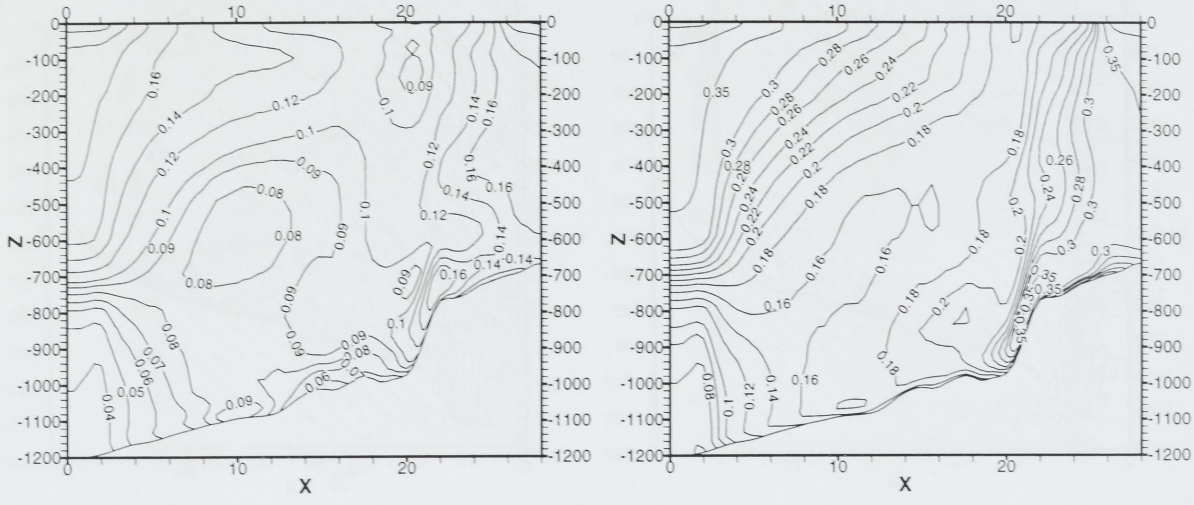

(a) Speed × 1, $\theta = 30°$

(b) Speed × 2, $\theta = 30°$

(c) Speed × 1, $\theta = 60°$

(d) Speed × 2, $\theta = 60°$

Figure 64: Current speeds at Section II.

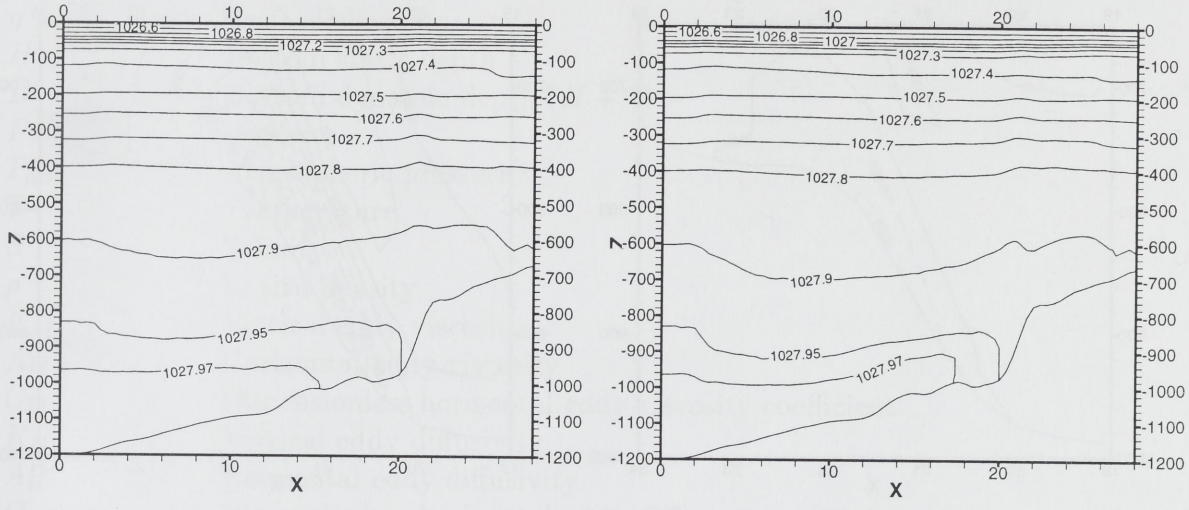

(a) Speed × 1, $\theta = 30°$

(b) Speed × 2, $\theta = 30°$

(c) Speed × 1, $\theta = 60°$

(d) Speed × 2, $\theta = 60°$

Figure 65: Density at Section II.

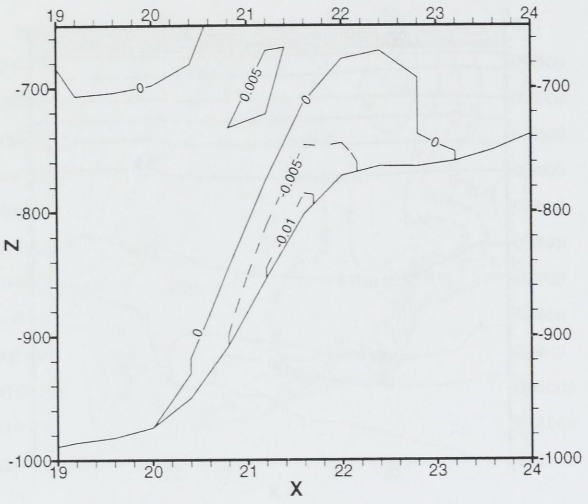

(a) Speed × 1, $\theta = 30°$

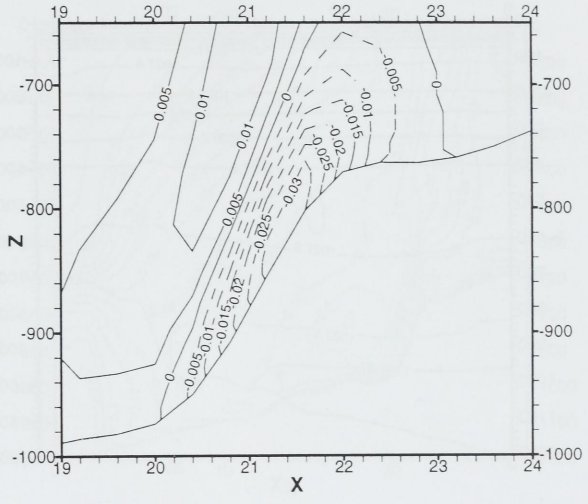

(b) Speed × 2, $\theta = 30°$

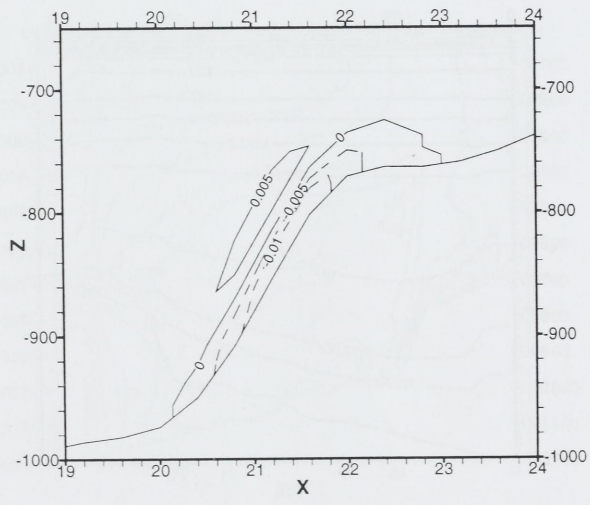

(c) Speed × 1, $\theta = 60°$

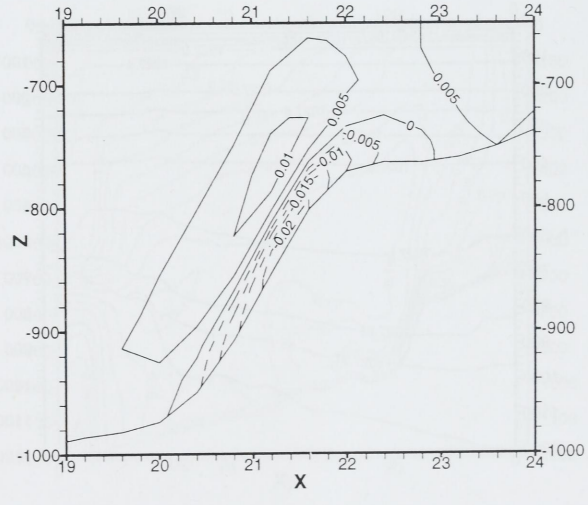

(d) Speed × 2, $\theta = 60°$

Figure 66: Vertical velocity at Section II.

B List of symbols

$\vec{U} = (U, V)$	Horizontal velocities in $x-$ and y-direction respectively
W	Vertical velocity in the z-coordinate system
ω	Vertical velocity in the σ-coordinate system
η	Surface elevation
H	Bottom static depth
D	Bottom dynamic depth $(H + \eta)$
P	Pressure
P_{atm}	Atmospheric pressure
T	Temperature
S	Salinity
ρ	In situ density
K_M	Vertical eddy viscosity
A_M	Horizontal eddy viscosity
C_M	Dimensionless horizontal eddy viscosity coefficient
K_H	Vertical eddy diffusivity
A_H	Horizontal eddy diffusivity
C_H	Dimensionless horizontal eddy diffusivity coefficient
$q^2/2$	Turbulent kinetic energy
l	Turbulent macro scale
ρ_0	Reference density
g	Gravity
f	The Coriolis parameter
$\vec{\tau}_0 = (\tau_{0x}, \tau_{0y})$	Surface wind stress
$\vec{\tau}_b = (\tau_{bx}, \tau_{by})$	Bottom stress
$\dot{T}_0$	The surface heat flux
$\dot{S}_0$	The net precipitation/evaporation at the surface
$\vec{U}_b = (U_b, V_b)$	Horizontal velocities at the bottom
W_0	Vertical velocity at the surface (z-coordinate)
W_b	Vertical velocity at the bottom (z-coordinate)
C_D	Bottom drag coefficient
κ	The von Karman constant
z_0	Bottom roughness parameter

References

[1] B. Ådlandsvik and H. Engedahl. Documentation of a three-dimensional baroclinic sea-model. Technical Report 16/1991/HSM, Institute of Marine Research, Bergen, NORWAY, 1991.

[2] L. Asplin, A.G.V. Salvanes, and J.B. Kristoffersen. Non-local wind-driven fjord-coast advection and its potential effect on pelagic organisms and fish recruitment, 1998. Accepted by Fisheries Oceanography.

[3] J. Berntsen. A sensitivity study of a baroclinic model for the North Sea with focus on the Utsira-Orkneys transect. Technical Report Fisken og Havet Nr. 16, Institute of Marine Research, 1998.

[4] J. Berntsen. USER'S GUIDE for a σ-coordinate numerical ocean model, 1999. Manuscript, Department of Mathematics, University of Bergen.

[5] J. Berntsen, D.L. Aksnes, and A. Foldvik. Fresh water driven primary production in a fjord. Technical Report 109, Dept. of Applied Mathematics, University of Bergen, 1997.

[6] J. Berntsen and E. Svendsen. Using the Skagex dataset for evaluation of ocean model skills. *Journal of Marine Systems*, 18:313–331, 1999.

[7] J. Berntsen, E. Svendsen, and M. Ostrowski. Validation and sensitivity study of a sigma-coordinate ocean model using the Skagex dataset, 1996. ICES CM 1996/C:5.

[8] J. Blindheim, V. Borovkov, B. Hansen, S.Aa. Malmberg, W.R. Turrell, and S. Østerhus. Upper layer cooling and freshening in the Norwegian Sea in relation to atmospheric forcing. *Accepted in Deep-Sea Research*, 1999.

[9] A.F. Blumberg and G.L. Mellor. A description of a three-dimensional coastal ocean circulation model. In N. Heaps, editor, *Three-Dimensional Coastal Ocean Models, Vol.4*. American Geophysical Union, 1987.

[10] A.M. Davies, P.J. Luyten, and E. Deleersnijder. Turbulence energy models in shallow sea oceanography. In D.R. Lynch and A.M. Davies, editors, *Quantitative Skill Assessment for Coastal Ocean Models*. American Geophysical Union, 1995.

[11] A.M. Davies and J. Xing. An intercomparison and validation of a range of turbulence closure schemes used in three dimensional tidal models. In D.R. Lynch and A.M. Davies, editors, *Quantitative Skill Assessment for Coastal Ocean Models*. American Geophysical Union, 1995.

[12] B.I. Dybern, D.S. Danielssen, L. Hernroth, and E. Svendsen. The Skagerrak Experiment-Skagex report 1988-1994. Technical Report 635, TemaNord 1994:635, 1994.

[13] T. Eldevik and K.B. Dysthe. Short frontal waves: May frontal instabilities generate small scale spiral eddies?, 1998. Manuscript, Department of Mathematics, University of Bergen.

[14] I. Eliassen and J. Berntsen. Effects of enhanced resolution in the north sea and the skagerrak, 1999. Manuscript, Department of Mathematics, University of Bergen.

[15] I. Eliassen and J. Berntsen. Evaluation of methods for estimating the internal pressure in sigma-coordinate ocean models using measurements from the norwegian trench and the skagerrak, 1999. Manuscript, Department of Mathematics, University of Bergen.

[16] H. Engedahl, B. Ådlandsvik, and E.A. Martinsen. Production of monthly mean climatological archives of salinity, temperature, current and sea level for the Nordic Seas. *J. Mar. Syst.*, 14:1–26, 1998.

[17] B. Galperin, L.H. Kantha, S. Hassid, and A. Rosati. A quasi-equilibrium turbulent energy model for geophysical flows. *J. Atmos. Sci.*, 45:55–62, 1988.

[18] D.R. Lynch and C.G. Hannah. Inverse model for limited-area hindcasts on the continental shelf. *Submitted to Journal of Atmospheric and Oceanic Technology*, 1999.

[19] D.R. Lynch, J.T.C. Ip, C.E. Naimie, and F.E. Werner. Convergence studies of tidally-rectified circulation on georges bank. In D.R. Lynch and A.M. Davies, editors, *Quantitative Skill Assessment for Coastal Ocean Models*. American Geophysical Union, 1995.

[20] E.A. Martinsen and H. Engedahl. Implementation and testing of a lateral boundary scheme as an open boundary condition in a barotropic ocean model. *Coastal Engineering*, 11:603–627, 1987.

[21] G.L. Mellor and A.F. Blumberg. Modelling vertical and horizontal diffusivities in the sigma coordinate system. *Mon. Weather Rev.*, 113:1379–1383, 1985.

[22] G.L. Mellor and T. Yamada. Development of a turbulence closure model for geophysical fluid problems. *Rev. Geophys. Space Phys.*, 20:851–875, 1982.

[23] N.A. Phillips. A coordinate system having some special advantages for numerical forecasting. *J. of Meteorology*, 14:184–185, 1957.

[24] D. Slagstad. A 4-dimensional physical model of the Barents Sea. Technical Report STF48 F87013, SINTEF, 1987.

[25] J. Smagorinsky. General circulation experiments with the primitive equations, I. The basic experiment. *Mon. Weather Rev.*, 91:99–164, 1963.

[26] D.-P. Wang. Mutual intrusion of a gravity current and density front formation. *J. Phys. Oceanogr.*, 14:1191–1199, 1984.

[27] G. Weatherly and P.J. Martin. On the structure and dynamics of the ocean bottom boundary. *J. Phys. Oceanogr.*, 8:557–570, 1978.